North Atlantic Deep Water and Antarctic Bottom Water: Their Interaction and Influence on Modes of the Global Ocean Circulation

Dissertation
zur
Erlangung des Grades eines
Doktors der Naturwissenschaften
- Dr. rer. nat. -

Dem Fachbereich Physik der
Universität Bremen
vorgelegt von

Holger Brix
Bremerhaven, den 5. Juni 2001

1. Gutachter : Prof. Dr. D. Olbers
2. Gutachterin : Prof. Dr. M. Rhein

Alfred-Wegener-Institut für Polar- und Meeresforschung

Ein Mensch, der lebt,
will uferlos schauen.

Herbert Achternbusch

North Atlantic Deep Water and Antarctic Bottom Water: Their Interaction and Influence on Modes of the Global Ocean Circulation

Abstract

Interhemispheric signal transmission in the Atlantic Ocean connects the deep water production regions of both hemispheres. The nature of these interactions and large scale responses to perturbations on time scales of years to millenia have been investigated using a global three-dimensional general circulation model based on the primitive equations (GFDL's MOM-2) coupled to a dynamic-thermodynamic sea ice model with a viscous-plastic rheology. The coupled model reproduces many aspects of today's oceanic circulation. Testing the model's sensitivity with regard to changes in the model configuration and parameterizations revealed a strong dependence of the model results from eddy diffusivities, filtering and topographic effects. Restoring time scales for surface salinity were found to be of minor importance.

The internal variability in the ocean-sea ice system has been addressed by analyzing the model results with statistical techniques. A decadal oscillation could be identified in the Southern Ocean. A sequence of Kelvin and Rossby waves carries anomalies in this frequency band northward across the equator.

Longer-term variability in the ocean is mainly determined by advective processes. A set of experiments in which the surface boundary conditions were changed showed the necessity to continue integrations over thousands of years until new equilibria are established. Buoyancy changes in the Weddell and Labrador Seas exert a direct effect on the overturning cells of the respective hemisphere. They influence the density structure of the deep ocean and thereby lead to alterations in the strength of the ACC. The model results suggest an influence of the ACC on convective activities in the Southern Ocean. Changing the wind stress south of 30°S influences the magnitude of the deep water production of both hemispheres. The interhemispheric effect in these experiments cannot be explained solely by advective mechanisms (contradicting previous studies by TOGGWEILER AND SAMUELS, 1993a, 1995). Switching off the wind stress over the latitude band of the Drake Passage leads to a slow gradual decrease of the water mass transport in the ACC resulting in an almost complete cessation.

Contents

List of Figures

List of Tables

1. Introduction

> There are two inhabitable sections of the earth: one near our upper, or northern pole, the other near the other or southern pole; and their shape is like that of a tambourine. . . . Now since there must be a region bearing the same relation to the southern pole as the place we live in bears to our pole, it will clearly correspond in the ordering of its winds as well as in other things.
>
> *Aristotle, Meteorologica, Book II, 5.*[a]

> You will also observe with accuracy the Situation of such Islands as you may discover in the Course of your Voyage that have not hitherto been discover'd by any Europeans, and take possession for His Majesty and make Surveys and Draughts of such of them as may appear to be of Consequence, without Suffering yourself however to be thereby diverted from the Object which you are always to have in View, the Discovery of the Southern Continent so often Mentioned . . .
>
> *Additional Instructions for Lt. James Cook,*
> *Appointed to Command H.M. Bark the Endeavour*[b]

Aristotle's notion suggesting that the symmetry of a sphere demanded the existence of a land mass on the southern hemisphere to balance the earth's inhabited northern regions has influenced politics and science until the age of Enlightenment. It was Ptolemy, who drew a map in 150 A.D. showing a large continent connecting Africa and Asia in the south naming it "Terra Australis Incognita". The search for this land mass and the possible wealth to be found there inspired numerous expeditions until the late eighteenth century. The secret order for *James Cook*, dated 1768, was one of the last attempts to reveal the mystery of the Southern Continent. One result of his expeditions was the insight that such a place – if existing – could hardly be a fertile, profitable one.

It is astonishing that even in our modern world Aristotle's idea seems to hold in a way. Taking his works literally, of course, he was wrong; in a figurative sense the idea of both

[a] Translated by E.W. Webster (Ross, 1963).
[b] Citation after Beaglehole (1955).

hemispheres balancing each other is at least true in the field of ocean dynamics. Enormous amounts of heat are transported from the equator to the poles in both atmosphere and ocean to compensate for differential insolation. This meridional radiation gradient, together with the earth's rotation, drives every dynamical process in the climate system – directly or indirectly. The atmosphere is the component reacting fast with its most prominent time scale ranging up to weeks and months. Dynamical processes in the ocean have scales of up to more than thousand years. Due to its high heat capacity the ocean acts as reservoir, absorbing heat in one place, releasing it in another. On an "aqua planet", i.e. without continents, ocean circulation would be confined to the two hemispheres, there would be no need for interhemispheric exchanges. On earth with its asymmetric distribution of land masses the situation is different: ocean currents have to arrange with the obstacles in their way. In the atmosphere high mountains like the Himalaya or the Rocky Mountains exert a modifying effect on the circulation patterns, in the oceans the land masses give stronger constraints. This is the reason why interhemispheric processes in the atmosphere are of minor importance, while there is an ocean-wide system of water mass exchange connecting the Atlantic, Pacific and Indian Oceans, the northern and southern hemisphere, the upper ocean and the abyss.

This global water redistribution needs more than a thousand years to transport a single water parcel – and with it its physical properties – through the whole cycle. The ocean therefore plays a key role in understanding global change. Its large time scale acts as a brake to fast climate transitions; on the other hand it provides a memory of the climate's closer past and it forces changes to persist. The rise of atmospheric carbon dioxide concentration since the industrial revolution as recorded in the famous Hawaiian Mauna Loa curve and with it the rise of atmospheric temperatures prove a change in the earth's climate during more than the past hundred years. Only recently an increase of the heat content could be spotted in the ocean (LEVITUS ET AL., 2000). These changes are not uniformly distributed over the planet. About half of the increase in the ocean's heat content was found in the upper 300 m of the world ocean, substantial changes in depths greater than 1000 m were observed only in the North Atlantic. The Atlantic and Pacific have undergone a net warming since the 1950s, the Indian Ocean only since the mid-1960s. There are regions like the subpolar gyre in the North Atlantic even showing a cooling. Furthermore the trends are not monotonic: sea surface temperatures reveal two distinct warming periods, during 1920 to 1940 and since the 1970s.

It has been suggested, that the ocean acts to transmit switches between glacial and interglacial states of the climate system via its thermohaline circulation (e.g. GHIL ET AL., 1987; BROECKER AND DENTON, 1989). Model investigations indicate that there exist at least two stable states of the ocean circulation and that there is a critical threshold at which the system changes from one into another (e.g. RAHMSTORF, 1999). It is still subject to discussions whether these variations are reactions to external forcing, internal oscillations of the system or a mixture of both. Nevertheless, there seems to be strong evidence from both modelling and observations that freshwater forcing plays a key role in regulating the stability of the thermohaline circulation. For example, meltwater inflows or surges of

icebergs into the North Atlantic have been made responsible for the triggering of rapid collapses of the overturning circulation (e.g. BJÖRCK ET AL., 1996).

A structural analysis restricted to processes inherent in the climate system reveals quite a number of feedback processes and nonlinear interactions that involve atmosphere, ocean, cryosphere and land / biosphere. There have been numerous investigations with models of all degrees of sophistication aimed at identifying the mechanisms that control the components of the climate system and their interactions. The complexity and nonlinearity of the problem requires to limit investigations to only a subset of components and aspects. The present work concentrates on the large scale dynamics of the oceans and sea ice. The emphasis is laid on processes involving the Atlantic and the Southern Ocean and its deep water production regions. The interplay of North Atlantic Deep Water, Antarctic Bottom Water and the Antarctic Circumpolar Current is addressed applying a global ocean general circulation model coupled to a dynamic-thermodynamic sea ice component. Different sets of model runs are used to detect interhemispheric interactions of advective nature as well as those involving wave propagation.

Chapter 2 gives a broad introduction into theory and observations of the global ocean circulation and its interactions with other components of the climate system – in particular sea ice. One section therein is dedicated to observed variability on various time scales, another to the feedbacks and equilibria mentioned before. Section 2.7 then deals with large and global scale phenomena, teleconnections and interhemispheric interactions. A description of the model components used in this study, their coupling and the basic set-ups is presented in chapter 3. Chapter 4 illustrates the main features of the model in equilibrium state; the results of testing the ocean model's sensitivity to variations in parameterizations is discussed in chapter 5. A statistical analysis of the model results is performed in chapter 6, investigating time scales and pathways of the spreading of signals. Examining the reaction to alterations in the systems boundary conditions (chapter 7) reveals mechanisms of the thermohaline circulation and serves as a basis for a comparison of the model's behavior with the results of other studies. Finally, chapter 8 summarizes the results of the present investigation and gives an outlook.

2. The Global Ocean Circulation

The global ocean circulation is driven by two types of forcing: wind and buoyancy. Winds drive ocean currents by transmitting momentum to the oceanic surface layer; buoyancy changes are established by heat and fresh water fluxes. Density gradients within the oceans cause the water masses to move. There are only few locations on earth - around the Antarctic continental margins and in the northern North Atlantic - where deep water production takes place. Only there the precondition of sufficient buoyancy loss of the upper layer waters from air-sea and sea-ice exchanges is fulfilled. These sinking water masses spread into all ocean basins preferably along the western boundaries. In a variety of places upwelling brings water masses back to the intermediate and upper layers of the ocean. A poleward advection of warm and salty upper layer water closes the budget. This system of redistribution of global water masses is commonly known as the "conveyor belt", a terminology introduced by BROECKER (1987, 1991) (A simplified sketch is shown in Fig. 2.1).

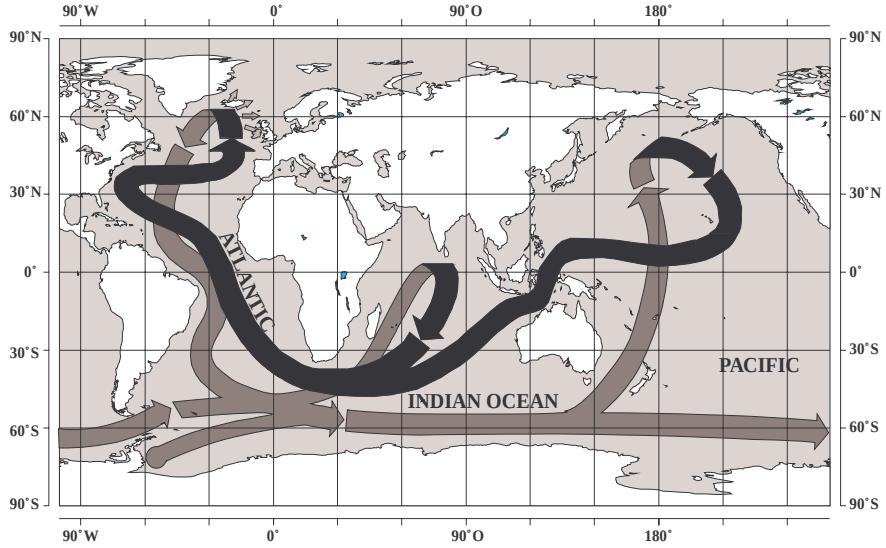

Figure 2.1.: *Cartoon of the global ocean conveyor belt circulation, after* VON STORCH ET AL. *(1999). The black arrows indicate upper layer, grey arrows lower layer circulation.*

2.1. The Thermohaline Circulation of the Atlantic Ocean

Historical Approaches It has not been long that the global-scale ocean circulation presents an almost closed picture. Certain features and flow patterns had been identified in the ancient world and in the age of the discovery of the Americas. The picture that existed then was characterized by nautical necessities and of course limited to surface observations. The first steps into a scientific (at least in our modern understanding) approach were done in the 19th century by people like *Alexander von Humbold*, Sir *J. Clark Ross* and *M. F. Murray*, just to mention a few. The first classical description of the abyssal and deep large-scale meridional circulation in the Atlantic Ocean was offered by WÜST (1935) who analyzed the data base collected during the German *Meteor* expedition between 1925 and 1927.

STOMMEL (1957) provided a conceptual two-layer model explaining both the wind-driven and thermodynamically driven Atlantic Ocean general circulation. Fig. 2.2 shows a two-layer sketch presenting his simulation of the pathways of North Atlantic Deep Water (NADW) in the lower layer along with its compensation flow and the directly wind-forced circulation in the upper layer. He presumed the sinking in the northern North Atlantic to be caused by atmospheric cooling forcing deep convection. In this model upwelling takes place in the area of the Antarctic Circumpolar Current (ACC) and to a lesser extent in the subtropical gyre of the North Atlantic.

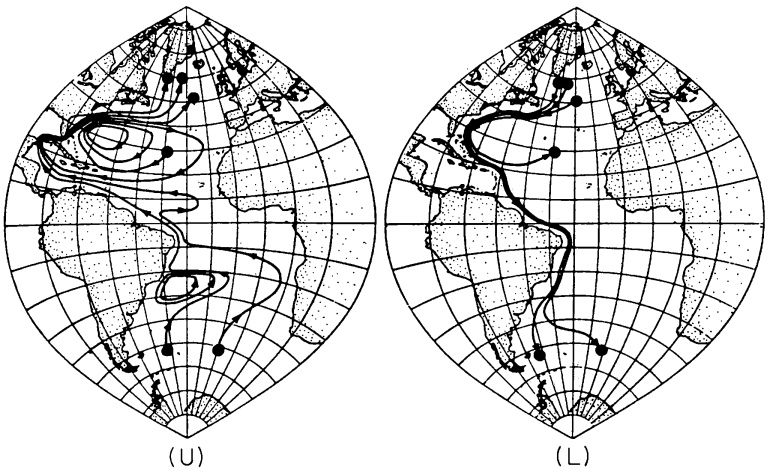

Figure 2.2.: *Schematic transport streamline field taken from* STOMMEL *(1957). Left: upper layer, right: lower layer. Solid circles indicate the sinking of North Atlantic Deep Water (NADW) in the northern North Atlantic and upwelling elsewhere.*

The Observed Present-Day Circulation The present-day picture of the global conveyor belt and the circulation of the Atlantic Ocean has been described thoroughly by SCHMITZ AND MCCARTNEY (1993) and SCHMITZ (1995). A simplified cartoon showing

the main features of the latter is presented in Fig. 2.3. It should be noted that the figures given in the following are subject to interannual variability and that some of the values are still under discussion. The most striking circulation property is an asymmetric meridional overturning cell spanning both hemispheres. Approximately 13 Sv (1 Sverdrup $\equiv 10^6$ m^3/s) enter the South Atlantic in the upper layers across 32°S. On its way to the equator this thermocline and intermediate water upwells to shallower depths (presumably in regions close to the equator). However, the two-dimensional picture of Fig. 2.3 is not sufficient to explain the path of these water masses in the North Atlantic. After crossing the equator the 13 Sv circulate through the Caribbean and into the Gulf Stream. By then the transport has more than doubled due to wind-driven contribution (not included in Fig. 2.3). At approximately 40°N the Gulf Stream is separated into two branches: one recirculates feeding the subtropical gyre, whereas the northward branch constitutes the North Atlantic Current. 2 Sv of Gulf Stream water cools and sinks leaving the upper layers even before Cape Hatteras while 1 Sv upwells off the coast of Africa. Together with 1 Sv originating from Mediterranean outflow, this sums up to a net total of 13 Sv reaching the higher latitudes and sinking there producing NADW. This process is of course far more complex than indicated in Fig. 2.3 and will be addressed in detail in section 2.3.2. It should be noted in this context that this sketch ignores the water mass contribution coming from the Pacific Ocean through the Bering Strait, which (subject to interannual variations) has been estimated to values between 0.8 and 0.9 Sv by ROACH ET AL. (1995).

4-5 Sv of northward bound Antarctic Bottom Water (AABW) flow enters across 32°S in the abyssal ocean. Approximately just 1 Sv is diverted through the Romanche Fracture Zone into the eastern basin. About the same quantity warms and upwells after crossing the equator. The remaining 3 Sv join the southward flow of the deep western boundary current (DWBC) along the coast of North America adding modified AABW to it. The DWBC can be divided into about 4 Sv of lighter Upper North Atlantic Deep Water (UNADW) and a denser and saltier core of about 12 Sv Lower North Atlantic Deep Water (LNADW). The origin of these differences will be explained in section 2.3.2. Adding the 1 Sv of upwelled AABW results in 17 Sv cross-equatorial flow. Mixing of the 1 Sv coming through the Romanche Fracture Zone and another 2 Sv of Antarctic Intermediate Water (AAIW) totals to a deep outflow of as much as 20 Sv at the southern end of the Atlantic basin.

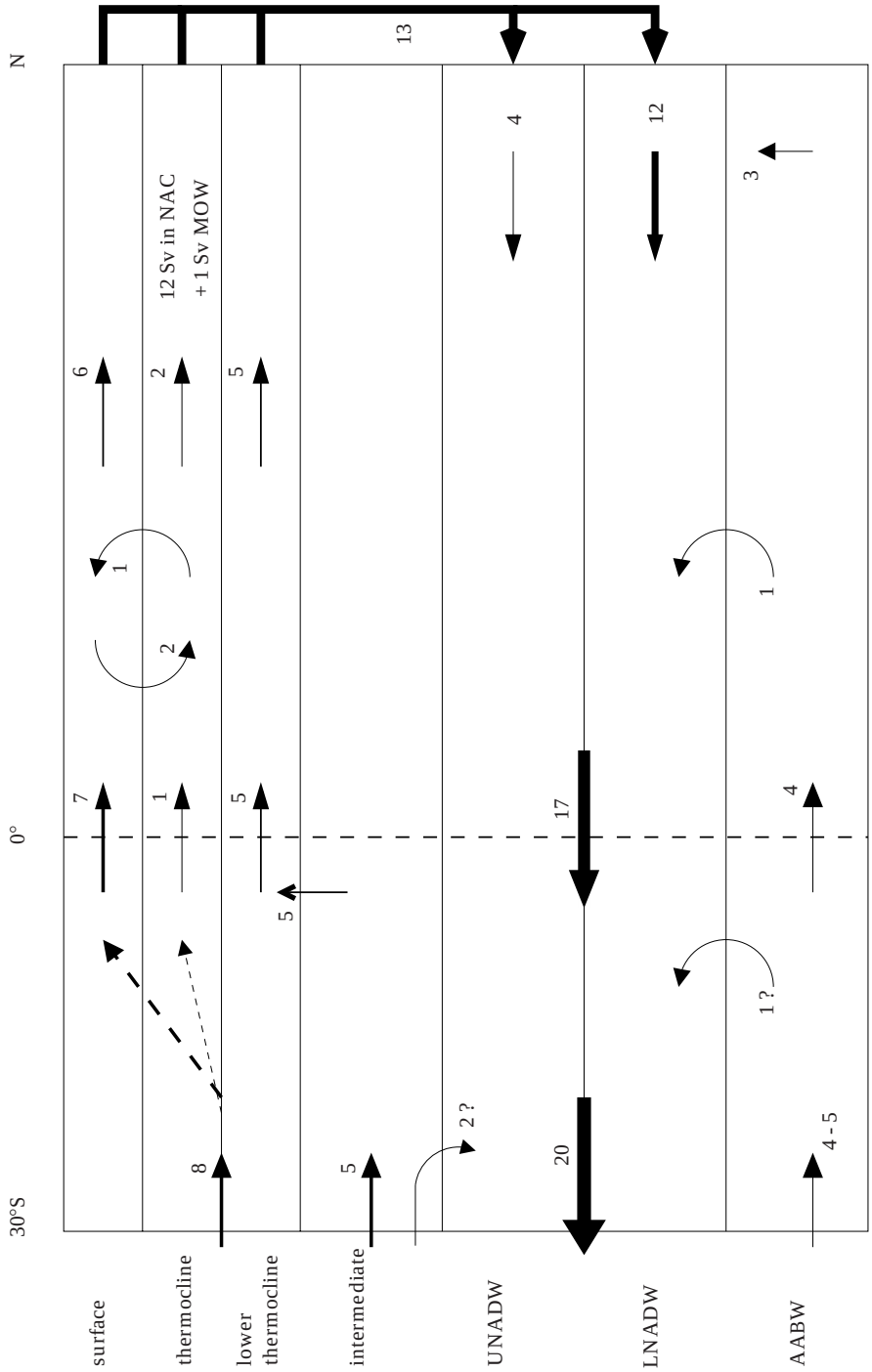

Figure 2.3.: *Thermohaline circulation of the North Atlantic, after* SCHMITZ AND MCCARTNEY *(1993) and* HUGHES *(1995). Transports are in Sv. UNADW, LNADW: Upper/Lower North Atlantic Deep Water; AABW: Antarctic Bottom Water; NAC: North Atlantic Current; MOW: Mediterranean Outflow Water.*

2.2. Closing the Conveyor Belt

The completion of the Atlantic circulation is still a matter of investigation and intense discussions. To balance the deep water production in the northern North Atlantic upwelling processes in other parts of the world ocean must take place. It should be kept in mind, that the picture of an "upper" and a "lower" layer as suggested by Fig. 2.1 is oversimplified. Convection can of course extend from the surface to the abyss and upper ocean upwelling in regimes like the Peru and Benguela Current systems reaches into and through the thermocline. It has been assumed for a long time that the mechanism of converting deep waters to lighter ones happens in broad regions spread over the ocean interior. STOMMEL AND ARONS (1960) base their theory of the abyssal circulation on this assumption. SCHMITZ AND MCCARTNEY (1993) on the other hand argue that the upwelling path for the return flow is concentrated in the circumpolar regions as well as in the equatorial regions of the Atlantic; the circumpolar upwelling south of the ACC is wind-forced and does not occur as broad diffusive upwelling (TOGGWEILER AND SAMUELS, 1993b). On the other hand there seems to be evidence for upwelling to occur in a variety of places and in comparatively small steps, so called differential upwelling. Recently, LEDWELL ET AL. (2000) (investigating tracer release experiments), found that mixing can reach large values over rough topography in the abyssal ocean. The sites for these buoyancy flux regions are few and the mixing processes do not depend on the large scale circulation itself, as the source of its mechanical energy probably are the tides (MUNK AND WUNSCH, 1998).

Closing the picture of the global thermohaline circulation (THC), SCHMITZ AND MCCARTNEY (1993) suggest the so called cold water route: the main compensation for the Atlantic outflow across 32°S is due to AAIW entering through the Drake Passage between South America and the Antarctic Peninsula. This AAIW is formed in the Pacific as well as in the Atlantic Ocean. The missing amount is credited to AABW entering at the ocean floor. On the contrary the concept of the warm water route describes the upwelling of Atlantic deep water in the thermoclines of the Pacific and Indian Ocean. These water masses re-enter the Atlantic via the Agulhas Retroflection off southern Africa. GARZOLI AND GORDON (1996) estimate this transport at 2-5 Sv, while SCHMITZ (1995) suspects the cold water route to contribute approximately 10 Sv. It should be stressed that those two pathways are not mutually exclusive. The difficulty lies in the determination of the cold-to-warm route transport ratio, as the properties of these water masses are substantially different, which of course has implications on e.g. the salinity structure of the Southern Atlantic and by that on the characteristics of water masses flowing north to feed the deep water production. Another factor to be regarded in this respect is that the ratio mentioned depends on the influence of the wind field over the Southern Ocean. Effects of the variability of this wind forcing will be discussed later.

Besides transporting mass the conveyor belt takes its share in regulating the worlds climate through its ability to transport huge amounts of heat. The equator-to-pole heat flux associated with the meridional overturning circulation amounts to about 2 PW

(MUNK AND WUNSCH, 1998). The ocean is cooled in the northern hemisphere by 1.7±0.2 PW, in the southern by 0.7±0.3 PW, while the tropics are heated by 2.3±0.4 PW. Changes in oceanic heat transport can have a large impact on atmospheric temperatures and thus on climate (GANACHAUD AND WUNSCH, 2000). Before investigating the nature and possible consequences of variability the following section will discus the mechanisms of deep water production more closely.

2.3. Deep Water Production

2.3.1. The Production of AABW

The Southern Ocean plays a central role in the global circulation. It allows communication between the northern oceans, while isolating them from the southern polar regions. It is the only place on earth where water masses can flow almost unhindered all around the globe at one latitude band. Its most prominent feature (at least in terms of transport) is called the Antarctic Circumpolar Current (ACC); it is by far the strongest circulation system on Earth. Most transport estimates reference observations made in the Drake Passage, where the Southern Ocean has the least meridional extent. WHITWORTH, III (1983) and WHITWORTH, III AND PETERSEN (1985) name 134 ± 13 Sv for the mean transport - a recent analysis of WOCE (World Ocean Circulation Experiment) section A21 by GANACHAUD AND WUNSCH (2000) gives a value of 140 ± 6 Sv. The ACC consists of several fronts; the two most important ones – the Subantarctic and the Polar Front – are displayed in Fig. 2.4. South of the ACC two cyclonic gyre systems exist – the Ross and the Weddell Gyre.

Another outstanding feature of the Southern Ocean is the fact, that the permanent thermocline does not extend into the polar regions but penetrates to the surface in the Subtropical Convergence. The Southern Ocean, therefore, only shows very small density variations with depth, the water column is generally stratified relatively weakly (MARTINSON, 1990). Besides resulting in a deep reaching current system, this density structure implies a high relevance of the ocean floor topography. South of the Polar Front the Antarctic Divergence is located. It is the place where high salinity NADW reaches the surface coming from depths of more than 2,000 m. The portion of this water mass reaching the upper 200 m warms the surface waters and melts sea ice. In the Polar Front part of this water mass, now warmed and diluted by melt water, snow and rain, on its way north sinks, creating a new water mass known as Antarctic Intermediate Water (AAIW). It can be traced in all of the three world oceans, characterized by its low salinity. Most of the AAIW found in the Atlantic Ocean enters from a formation region in the eastern Pacific through the Drake Passage (ENGLAND ET AL., 1993). Close to its formation region it has a salinity of about 33.8 psu and a temperature of 2.2°C. On its way north it mixes with water masses from higher and lower layers gradually weakening the salinity minimum to values of near 3°C and 34.3 psu at the Subtropical Convergence (TOMCZAK AND

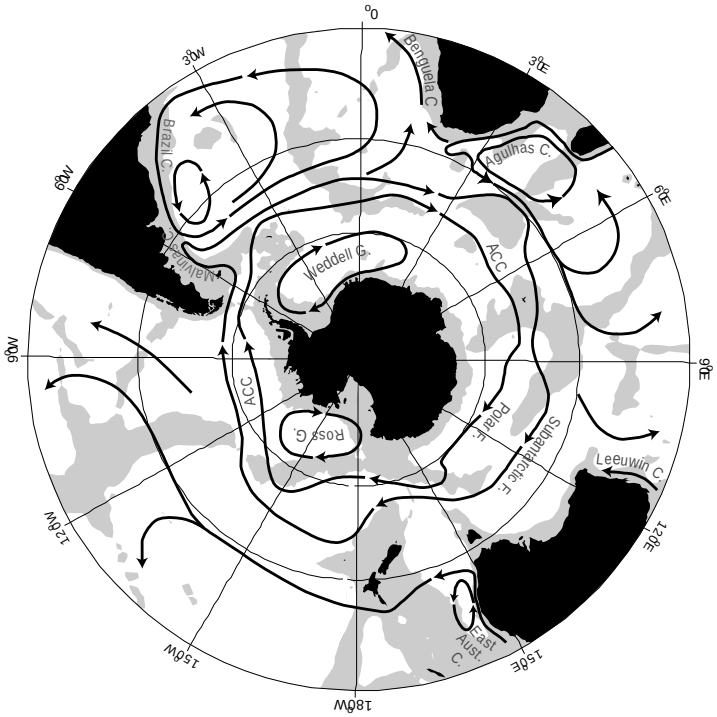

Figure 2.4.: *Schematic map of major currents in the southern hemisphere oceans south of 20°S. Depths shallower than 3500 m are shaded. The two major cores of the ACC are shown, the Subantarctic Front and the Polar Front. Taken from* RINTOUL ET AL. *(2001).*

GODFREY, 1994). The AAIW is located below the thermocline, but in depths shallower than about 1,500 m (GORDON, 1996).

Freezing of sea ice on the Antarctic continental shelf leads to bottom water formation. The salt rejected by newly formed ice increases the salinity and therewith the density on the shelves. If there is wind forced ice export from the shelves the process of ice production can continue to inject salt into the upper layer of the ocean. The salty water accumulates on the shelves and when the salinity reaches a threshold value the water is dense enough to sink down over the shelf edges into the deep basins. On its way down the slope of the shelf intense mixing processes with water derived from the Circumpolar Current form the properties of Antarctic Bottom Water. Therefore it would not be correct to account AABW production solely to convection; subsurface mixing surely has an important share. This kind of processes are confined to some specific regions. Main area for AABW production is the Weddell Sea (for a review and the role of the Weddell gyre see FAHRBACH ET AL., 1998), other places are off the Adélie coast (RINTOUL, 1998), along the Enderby coast or in Prydz Bay (see RINTOUL ET AL., 2001, also for a more detailed description of the processes mentioned above). Concerning the AABW formation rate, figures to be found in the literature span quite a broad range (e.g. 18-40 Sv by SAUN-

DERS AND THOMPSON (1993); 8 and 15 Sv by ORSI ET AL. (1999) using CFC-11 and PO_4^*[a] inventories, respectively; 21±6 Sv by GANACHAUD AND WUNSCH, 2000). Part of the formed AABW (5 Sv according to RINTOUL, 1991) flow into the Southern Ocean sector of the South Indian Ocean, while 7 Sv flow northward at the latitude range of the Brazil Basin, approximately 4 Sv of it entering into the southern Atlantic (SCHMITZ, 1995). The remaining 3 Sv upwell or are mixed with NADW. In its initial stages AABW has a salinity of 34.66 psu and a temperature of about -0.8°C, rising to 1.9°C when the waters reach the North Atlantic (MANTYLA AND REID, 1983; SCHMITZ, 1995).

2.3.2. The Production of NADW

The role of the Arctic on the global ocean circulation (and on the global climate) differs substantially from the Antarctic. The most striking feature is of course the absence of a land mass covering the pole and its surrounding regions. Moreover, the Arctic Ocean is encircled almost completely by the American and Eurasian continents leaving only comparatively small exits to the world oceans: the Bering Strait, the Canadian Archipelago and the sill from Greenland to Scotland. Being separated from the rest of the global ocean by these relatively shallow ridges leads to circulation characteristics governed by thermohaline forcing typical for mediterranean seas (DIETRICH ET AL., 1975). In the center of the Arctic Ocean four basins reach down to depths of up to 4000 m. They are surrounded by large shelf areas (see Fig. 2.5), which play a key part in the hydrology as numerous rivers discharge into this area. Their estimated freshwater import accounts for about the half of the freshwater transport entering the Arctic Seas. The other half is supplied by precipitation and the import of relatively fresh waters through Bering Strait and the Norwegian Coastal Current (AAGAARD AND CARMACK, 1989)[b].

On the other hand, ice formation is facilitated on the shelves due to the low salinities. The combined effect of brine release and wind driven ice export leading to the production of deep and bottom waters has already been outlined in the previous section. For the Arctic this process was explained in detail by AAGAARD ET AL. (1985). Other potential bottom water production areas are in the central Greenland Sea (surface water cooling in winter, see MEINCKE ET AL., 1997; RUDELS, 1998), and in the Barents and Norwegian Seas (heat loss of the warm, saline intermediate water, see MAURITZEN, 1996a,b).

As mentioned above the Arctic Ocean receives water from river runoff, precipitation, through the Bering Strait and in the Norwegian Coastal Current in the surface layer and with the West Spitsbergen and the Norwegian Atlantic Current in the intermediate layer. The East Greenland Current transports sea ice and water southwards through Fram Strait (i.e. between Greenland and Svalbard), a smaller part leaves the Arctic through the Canadian Archipelago. The mass balance is closed by overflow of about 4-5 Sv (DICKSON AND

[a] $PO_4^* = PO_4 + (O_2/175) - 1.95\mu\,\mathrm{mol/kg}$

[b] For a detailed description of the freshwater budget in the Arctic Ocean in general and the role of river runoff see PRANGE (2001).

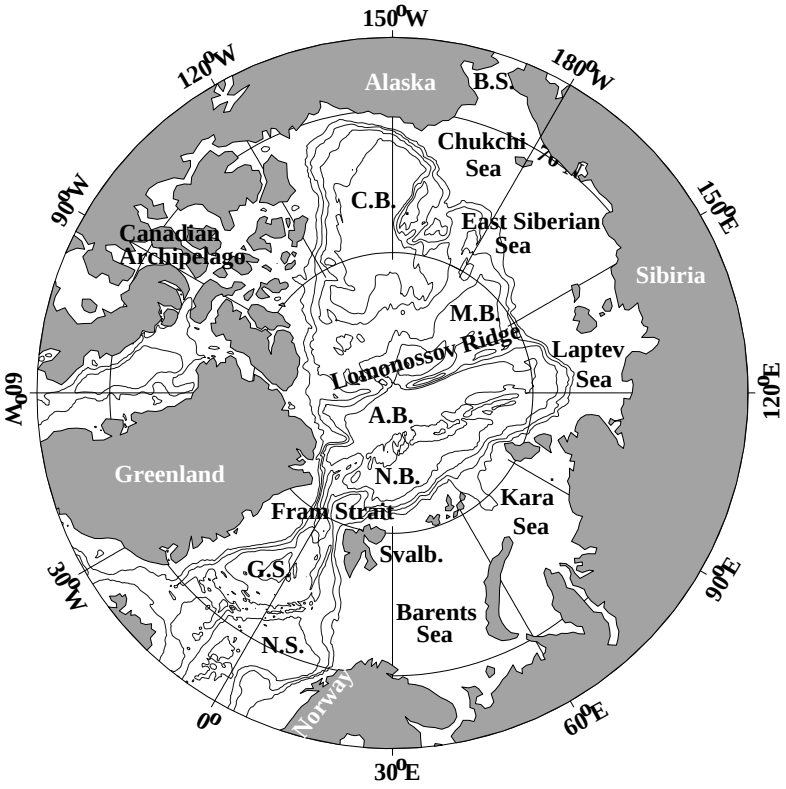

Figure 2.5.: *Bottom topography of the Arctic Mediterranean Sea. The 500, 1500, 2500 and 3500 m isobaths are shown. B.S.: Bering Strait, C.B.: Canadian Basin, M.B.: Makarov Basin, A.B.: Amundsen Basin, N.B.: Nansen Basin, G.S.: Greenland Sea, N.S.: Norwegian Sea, Svalb.: Svalbard.*

BROWN, 1994) crossing the Greenland-Iceland-Faroe-Scotland Ridge sinking to greater depths, compelled by Coriolis force to follow the western boundaries (i.e. the coastlines of Greenland and Iceland and the Mid-Atlantic Ridge – compare Fig. 2.6). On their way south these water masses substantially alter their characteristics by entrainment of ambient waters. When reaching the southern tip of Greenland their mass transport has more than doubled to approximately 10 Sv. It is then the water mass that has been referenced in section 2.1 as Lower North Atlantic Deep Water (LNADW). Upper North Atlantic Deep Water (UNADW) on the other hand is formed by winter convection in the Labrador Sea as Labrador Sea Water. Part of it spreads to the East and North, the rest can be found heading southward between 500 and 2,000 m as part of the global conveyor (SY ET AL., 1997; LAVENDER ET AL., 2000; RHEIN, 2000).

Of course the picture presented here is not complete, only the main circulation features are outlined[c]. Details of the circulation are still under discussion in the scientific community. Especially the temporal variability of the system is subject of intense re-

[c] A more complete picture of Arctic water masses and their circulation is given by CARMACK (1986) and RUDELS ET AL. (1999); for North Atlantic circulation refer to SCHMITZ (1996).

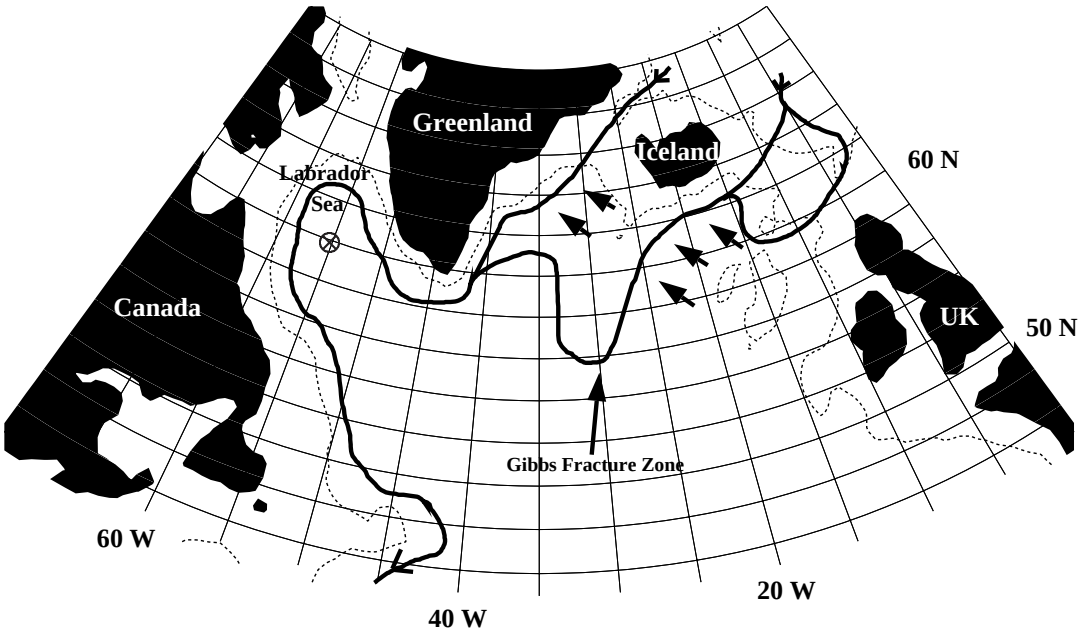

Figure 2.6.: *The path of overflow waters from the Arctic Mediterranean. The broken line indicates the 1000 m isobath. Deep convection in the Labrador Sea is marked by ⊗. The arrows indicate regions of entrainment. After* TOMCZAK AND GODFREY *(1994).*

search. Before taking a closer look at this topic in section 2.5, the role of sea ice in the climate system is portrayed in section 2.4.

2.4. The Role of Sea Ice

The freshwater budget of the high latitude oceans is strongly influenced by processes involving ice, among them thermodynamic and dynamic changes in sea ice, glacial melt, snowfall on ice, its subsequent melting and runoff of snow meltwater from the adjacent land. Sea ice influences the climate system of the earth by a variety of mechanisms (HARDER, 1996):

- Albedo: water absorbs about 90% of the insolation, sea ice about 20%, a value that is reduced even more if a snow cover is present.
- Insulation: heat fluxes between atmosphere and ocean in the polar regions can be tremendous, especially in winter. The presence of sea ice reduces the transports of sensible and latent heat substantially.
- Momentum: the torque exerted from the atmosphere on the ocean is modified by sea ice. It depends on the roughness of the surface; without sea ice it is governed by the wave height. With sea ice the nature of the ice surface, i.e. the existence of ridges

and other features determining the roughness, modify the momentum transfer into the ocean. The bigger the roughness, the more intense is the dynamical coupling of the ocean to the atmospheric forcing.

- Deformation: storms deform the ice cover, leading to the development of ridges, piling up floes, thereby changing the kinetic energy of the atmosphere into mechanical work. This leads to a reduced energy transfer from the atmosphere to the ocean.

- Salinity: freezing of sea ice causes the salinity of the oceanic surface layer to rise; most of the salt contained in sea water is ejected in a process called brine release during freezing. Together with the cooling of the surface layer by the heat transfer to the (cold) atmosphere this leads to the convection / deep water formation processes described above. The necessary high density can only be reached by the combination of both processes, thus restricting the "motor" of the global ocean circulation to be effective only in few places in the polar regions.

- Advection: during the formation of sea ice the ocean stratification is destabilized, while during melting fresh water is injected into the oceanic surface layer, stabilizing the stratification. Sea ice often is transported over large distances away from its formation regions leaving open water allowing further freezing. Ice drift thus advects huge amounts of fresh water and alters the latent heat budget influencing the climate system substantially.

It should be noted that these points only outline the main features and principal mechanisms. There are a number of feedbacks between the components of the climate system involving sea ice. Besides moderating the heat exchange between atmosphere and ocean at high latitudes, sea ice interacts with the climate system via the important mechanism of the ice-albedo-feedback (IPCC, 1990, and others). In a global warming scenario with rising air temperatures and diminishing ice cover, less solar radiation is reflected, the higher absorption of (the then larger) water covered areas leads to enhanced local warming and promotes further melting etc. This is not only of local importance, as a change of the temperature difference between high and low latitudes changes the circulation patterns of atmosphere and ocean. A negative feedback process involves the overlying atmosphere: diminishing ice cover leads to larger water covered areas, causing stronger evaporation and therewith enlarged cover of low clouds. As low clouds deplete the incoming solar radiation in the infrared fraction of the spectrum and change direct beam radiation to diffuse radiation the resulting broadband albedo of snow and ice is augmented. Thus more radiation is reflected, temperature cools and the sea ice production rises (CURRY AND WEBSTER, 1999).

The relevance of these and other feedback mechanisms for the variability and stability of the THC has been shown in a variety of investigations with numerical models of different complexity, sophistication and regional extent. Some results shall be given in section 2.6.

2.5. Observing Variability

The complexity and variety of mechanisms and feedbacks ruling the interplay of the components of the Earth's climate system make it necessary to restrict investigations to distinct scales. This constraint is valid not only with respect to the amount of processes and the spatial resolution taken into account but also when considering time scales. Temporal variability examined in Earth science spans from seconds (when investigating small scale atmospheric turbulence) to hundreds of millions of years (looking into plate tectonics). In principle, the causes for climate variability can be alterations in the internal dynamics and energy exchanges within the system or they can result from external forcing, e.g. changes of insolation or the effects of anthropogenic impacts. Detecting man made influence on climate change requires an understanding of the mechanisms that rule natural variability. The large number of interrelated physical processes impedes simple linear explanations. Here lies the main difficulty when interpreting observational data. Two main categories of data can be distinguished: data measured directly with instruments, and proxies, i.e. indirect indicators – for changing climate ranging from historical records as e.g. the number of ice-free days of lakes and rivers to geochemical tools as investigations of carbon isotopic composition of calcareous tests of foraminifera just to name two.

Some proxy data analyses indicate that the global THC has undergone dramatic changes on glacial time scales (DUPLESSY AND SHACKLETON, 1985; KELLOGG, 1987; GHIL ET AL., 1987; BROECKER AND DENTON, 1989; LYNCH-STIEGLITZ ET AL., 1999, and others)[d]. Their data indicate that the Atlantic overturning circulation was generally weaker during glacial periods and the source areas of NADW and AABW formation were shifted. YU ET AL. (1996) on the other hand deduced only a relatively small decrease in meridional overturning during the Last Glacial Maximum (LGM – about 21,000 years BP – investigating ^{231}Pa / ^{230}Th ratios in sediment cores).

Analyzing century time scales STOCKER AND MYSAK (1992) interpreted data from ice cores, tree rings, pollen records and historical and instrumental data records. Their conclusion is that the ocean's THC exhibits natural variability, i.e. not triggered from outside, on a century time scale which produces heat flux oscillations between ocean and atmosphere.

Most intense research during the last thirty or so years has gone into decadal and interdecadal variability. Most prominent examples are ENSO (El Niño / Southern Oscillation) and the NAO (North Atlantic Oscillation). Both phenomena result from an interplay of oceanic and atmospheric processes. While ENSO has its "center of action" in the tropical Pacific, the effects of its two states (commonly known as El Niño and La Niña) and the changes in between them can be observed almost all over the world (see PHILANDER, 1990). Less spectacular, but also of utmost importance for both regional and global climate is the NAO (HURRELL, 1995; MARSHALL AND KUSHNIR, 1997; DICKSON ET AL.,

[d] A profound overview of the proxy data used to investigate glacial meridional overturning is given by BOYLE (1995).

2000). Intense discussions about possible decadal variability in the North Atlantic were spawned by the observation of DICKSON ET AL. (1988) of a "Great Salinity Anomaly" (GSA). During 1968-1982 there was a widespread freshening of the subpolar gyre waters with amplitudes of up to more than 0.5 psu. (Another, even stronger, GSA was observed in the 1980s; BELKIN ET AL., 1998). DICKSON ET AL. (1988) described this feature as an advective event triggered by an abnormally strong freshwater export (especially in form of sea ice export) through Fram Straight. AAGAARD AND CARMACK (1989) pointed out that salinity stratification in the high latitude oceans is critically important for deep water production. They take the GSA as an example for how to alter or stop convection by slight changes in the fresh water budget, as has been shown for the Labrador Sea during the GSA by LAZIER (1980). DICKSON (1997) pointed to a connection between deep water production and the NAO. In phases of low Labrador Sea convection (as observed in the late sixties), convection in the Greenland Sea and mode water production in the Sargasso Sea was high, while the NAO index was in his "low-index" extreme state[e]. The other phase with high NAO index and reversed water formation patterns could be observed during the early 1990s.

Despite all effects and feedback loops described here, decadal variability is not the whole story: there are overlying trends and given the length (or more precise shortness) of observational data sets it is often hardly possible to attribute a distinct feature to the process or time scale governing it. Especially when looking for the effects of human impact onto climate it is hard to distinguish whether a process is part of natural ultra-low frequency variability or a trend caused by anthropogenic influence. The alteration of sea ice cover may serve as an example here. The shrinkage of Arctic sea ice cover between 1978 and 1996 was 34,000 km^2 per year, i.e. 2.8% per decade (PARKINSON ET AL., 1999; VINNIKOV ET AL., 1999) – a result derived from a satellite based data set. A numerical hindcast experiment with a dynamic-thermodynamic sea ice model performed by HILMER AND LEMKE (2000) shows a decrease of Arctic sea ice volume by 4% per decade for the period from 1958-1998. The mean ice thickness decreased from about 3.1 m to 1.8 m over the last forty years of the past century in most of the deep water portion of the Arctic Ocean according to data acquired on submarine cruises (ROTHROCK ET AL., 1999). The probability that observed trends in sea ice extent in the Arctic result from natural variability are less than two percent for 1978-98 and less than 0.1% for the 1953-98 trends according to VINNIKOV ET AL. (1999), who compared surface and satellite-based observations to control and transient integration of two climate models. Around Antarctica on the other hand the sea ice cover increased by $1.3 \pm 0.2\%$ from 1978 to 1996 (CAVALIERI ET AL., 1997)[f].

This example clearly shows the weakness of data analyses: the availability of ocean and sea ice data is limited and their results are not easily included into an conceptual

[e] The NAO index is comprised of the normalized sea-level pressure difference between Lisbon, Portugal and Stykkisholmur, Iceland (see HURRELL, 1995).

[f] Ice thickness data is not available for the southern hemisphere; a project to analyze ship track data in order to investigate ice thicknesses has been launched recently (see WORBY AND ACKLEY, 2000).

framework. To overcome this deficiencies numerical modeling can help revealing processes. The next section will give some examples of modeling efforts simulating the THC.

2.6. THC-Modelling: Feedbacks and Equilibria

For investigations of paleo climate scenarios, model runs over hundreds of thousand of years are necessary. Limits in computational power therefore require a simple model structure, i.e. models with a very coarse resolution, simplified topography, box or conceptual models. On one hand this leads to restrictions in the number of processes that can be taken into account, on the other it allows concentration on important mechanisms. Running an ocean general circulation model (OGCM) to investigate the global conveyor at present and during conditions similar to the LGM, SEIDOV AND HAUPT (1997) found a weakening of more than 40% and some shallowing of the conveyor during LGM conditions. Simulating a post-glacial freshwater discharge in the northern North Atlantic led to a complete collapse of the deep water production in the North Atlantic and a subsequent altering of global water transport paths. More general, large and rapid climate changes can best be explained by major reorganizations of the THC (STOCKER AND MARCHAL, 2000). The question how changes in the THC develop and whether there are general modes describing the global overturning circulation have been addressed by a large variety of numeric experiments and models of different complexity. A number of feedback mechanisms regulating the THC have been identified (WILLEBRAND, 1993; CURRY AND WEBSTER, 1999, or as cited):

- The positive salinity feedback: a negative salinity anomaly in the high latitudes (e.g. by excess precipitation or enhanced river runoff) leads to decreased density. This will diminish the sinking motion and thereby the meridional overturning, resulting in a reduced transport of salty waters from the lower latitudes, which in turn decrease the high latitude salinities (STOMMEL, 1961).

- Continuing the scenario with a reduced poleward advection of warm surface water will result in lower temperatures in the high latitudes, i.e. higher densities and stronger sinking and a stronger poleward heat transport, thereby establishing a negative temperature feedback.

- Changes in the sea surface temperatures (SST) will influence the air-sea heat flux leading to local air temperatures changes. A lower SST will cause lower air temperatures, increasing the meridional temperature gradient. This will lead to an increase in poleward atmospheric heat transport due to enhanced eddy activity. So the air temperature at high latitudes will increase, warm the oceanic surface layer and reduce density. Another effect of enhanced eddy activity was an increased atmospheric moisture transport into polar regions, decreasing salinity and density. Thus, the atmospheric heat and moisture cycles constitute a destabilizing positive

feedback (NAKAMURA ET AL., 1994; LOHMANN, 1996; LOHMANN ET AL., 1996; SCHILLER ET AL., 1997).

- The negative wind stress driven feedback: changed atmospheric circulation patterns associated with enhanced eddy activity cause a deepening of the trough over the northern North Atlantic. This leads to an intensification of the subpolar gyre and a stronger upwelling through Ekman-suction. Ekman transports lead to an intensified East Greenland Current, that exports fresh water into the North Atlantic (SCHILLER ET AL., 1997)[g].

- Decreased SSTs lead to increased sea ice formation, increasing the density by brine rejection, strengthening the THC – a negative feedback. On the other hand, sea ice insulates the atmosphere from the ocean, stops heat fluxes avoiding SSTs below the freezing point; vertical mixing is suppressed and the sea ice edge moves equatorward. This mechanism and the sea ice-albedo feedback (section 2.4) contribute to a positive feedback associated with sea ice (LOHMANN AND GERDES, 1998)[h].

There are more mechanisms with possible feedback-like effects that have not been included in this list, as they are only active under special conditions. A weaker overturning cell with lower SSTs, for instance, would lead to reduced evaporation. If the evaporated water returned to the ocean locally (by precipitation) there was no feedback. If in turn the precipitation fell in other regions, this would establish a positive feedback. Another potentially important process involves increased sea ice formation (e.g. in shelf regions) and thus enabled enhanced sea ice export representing an important freshwater transport over long distances. This could lead to decreased deep water formation in the regions where the sea ice was transported to.

Negative feedbacks can principally lead to an oscillatory behavior of the system, while positive feedbacks may cause instabilities, preconditioning for a partly self-sustaining system with possible multiple equilibria solutions (RAHMSTORF, 1999). The response of the THC to a perturbation depends on the relative strength of the feedbacks. Model studies have shown scenarios leading to a complete shut-down of the THC. The consequences of a disruption of the Atlantic THC are still under discussion - nevertheless it can be stated that they would be quite drastic, even if the effects of local sea surface cooling would be in part compensated by atmospheric heat transports reducing the effects on air temperature. There would be severe consequences for marine ecosystems and fisheries. A reduced or stopped THC would weaken the carbon dioxide uptake of the ocean, making the climate system more susceptible to further emissions (RAHMSTORF, 1997; SARMIENTO AND LE QUÉRÉ, 1996). Furthermore there are surely processes that have not been included in models yet. It is suspected, e.g., that changes in abyssal water

[g] SCHILLER ET AL. (1997) name this mechanism as the way their model reinitialized NADW formation after a collapse of the conveyor belt circulation.

[h] LOHMANN AND GERDES (1998) emphasize that in their experiments the insulating effect of sea ice is more important than salinity impacts.

properties as deep-water warming connected with shifts in convection sites could result in a sudden release of methane from dissociation of methane-hydrate in continental margin sediments. The methane would be oxidized to CO_2 leading to higher concentrations in ocean and atmosphere (HESSELBO ET AL., 2000).

In a fairly simple conceptual model (STOMMEL, 1961), consisting of two well-mixed reservoirs representing the low and high latitude oceans, the existence of two equilibrium states, depending on the range of the hydrological forcing, could be demonstrated. One was thermally dominated, i.e there was a strong poleward heat transport, the high latitude ocean was warm and salty and there were sinking processes taking place. The other case was salinity dominated with weak equatorward heat transport, a generally weaker circulation and no sinking at the colder and fresher high latitudes. To test this solution regarding its relevance for the 'real' ocean more sophisticated models have been applied to the problem. The results of some of them are shown in WILLEBRAND (1993). They are all characterized by the existence of more than one stable state.

In a variety of models there have been found global or local oscillations, i.e. regular transitions between two stable states of the system. An overview of self-sustained oscillatory behavior with thermal or thermohaline forcing has been given by WELANDER (1986). BROECKER (1990) provided an example for salinity forced oscillations of the THC (during the last ice age). Times of deep water production, ice melting and decreasing salinities changed with times of weak deep water production, stronger freezing and a salinity increase. WEAVER AND SARACHIK (1991) and WEAVER ET AL. (1993) showed model solutions with a decadal oscillatory behavior of the THC alternating between a present day circulation state and a total cessation.

Experience with numerical models taught that a shut-down of the THC requires the surmounting of a critical threshold. The climate systems sensitivity to perturbations and the determination and quantification of the conditions leading to a possible passing of the threshold and / or to the switching of the THC into another equilibrium state has been investigated with all kinds of models from simple ones, uncoupled OGCMs to fully coupled ocean-atmosphere GCMs. WILLEBRAND (1993), examining the influence of salinity perturbations, emphasizes that not only the strength of a perturbation is important, but also the location where it is introduced into the system. One way to reach the threshold to a complete stop of the THC is by augmenting atmospheric temperature (MANABE AND STOUFFER, 1993; STOCKER AND SCHMITTNER, 1997; SCHMITTNER AND STOCKER, 1999). This leads to a reduced meridional heat transport and regional cooling, the deep Atlantic circulation is then dominated by AABW (RAHMSTORF, 1996). There has also been shown a dependence on the rate of temperature increase - the faster the warming, the less stable the THC (STOCKER AND SCHMITTNER, 1997). RAHMSTORF (1997) quantifies the weakening of THC with 15-50 per cent for doubling atmospheric CO_2, MANABE AND STOUFFER (1993) find a complete halt of the THC for quadrupling carbon dioxide compared to pre-industrial values.

2.7. Long Distance and Interhemispheric Patterns

Having examined more structural aspects of the climate systems variability hitherto, the rest of this chapter is dedicated to patterns of variability spanning greater distances, especially those connecting high with low latitudes or acting as a link between the hemispheres. Taking into account the connections between the distinct parts of the world ocean it does not take wonder that one part reacts to another. But it is still the time scales and the interaction patterns that are to be investigated closer.

One focal point of this work are processes involving the Labrador Sea. For the northern hemisphere oscillation patterns have been identified in a number of studies (e.g. WINTON, 1997). For the Labrador Sea MEISSNER (1999) and YANG (1999) have recently provided investigations on this subject. MEISSNER (1999) describes a highly variable THC on multidecadal time scales. In her global ocean general circulation model coupled to an atmospheric energy and moisture balance model and a simple thermodynamic sea ice component, she finds a negative feedback loop between the strength of the overturning and sea ice cover causing an oscillation of the THC changing the strength of water mass export into the southern hemisphere. YANG (1999) investigates a link between decadal variability in Labrador Sea Water thickness data and SST in the equatorial region of the Atlantic. He names coastally-trapped baroclinic waves propagating along the western boundary as the means of signal transmission to gap the five years lag between the two phenomena.

The Antarctic Circumpolar Wave (ACW) is the most prominent feature of decadal variability in the southern hemisphere. The ACW (first identified by WHITE AND PETERSON, 1996) can be seen in anomalies of SST, sea level pressure (SLP) and sea ice extent. The anomalies propagate eastward circling the globe in approximately eight to nine years. Due to its zonal wavenumber 2, the period observed at a distinct point lies between four and five years. A similar period of about four years was found by STÖSSEL ET AL. (1998) and STÖSSEL AND KIM (1998) for the Weddell Sea region and the Drake Passage throughflow in modeling studies. The authors describe regional subsurface temperature anomalies, modifying convection and thereby deep-ocean temperature and salinity. The oscillating behavior is effected by a rapid barotropic response. A decadal oscillation in convective potential energy release, temperature and salinity in the Weddell Sea characterizing a predominantly baroclinic mode was described by STÖSSEL AND KIM (2001). From the origin of the disturbances signals spread northward along the western boundary into the equatorial Atlantic. The time scales of the models baroclinic adjustment match the travel time of anomalous water masses from the Weddell Sea to 18°S (5 to 11 years) as found in observational data by COLES ET AL. (1996) quite well.

Different mechanism of coupling both hemispheres have been discussed involving a variety of processes. Of course there are atmospheric links between the hemispheres and there is a continuous exchange of air masses via the equator effected e.g. by the seasonal variations of the Intertropical Convergence Zone (HOLTON, 1992). Concentrating

on ocean processes, WEYL (1968) hypothesized in a first investigation that reduced production of (warm and saline) NADW would lead to an increasing Antarctic sea ice cover by temperature and salinity feedbacks altering the stability of the water column. This effect would reduce heat transport to the base of the sea ice layer leading to weaker melting processes. Analyzing observations and modelling studies on the other hand CROWLEY (1992) argues high NADW production would lead to southern hemisphere temperature increase as the above argumentation neglects surface circulation changes. In the NADW circulation relatively cold water in the deeper layers is transported to the south while in the upper layers warm water travels north leading to a northbound net heat transfer. The amount of heat gain for the South Atlantic and the Southern Ocean in case of a weaker NADW overturning exceeds the heat loss by reduced upwelling of NADW by a factor of 3 to 6. In the opposite case large NADW production would lead to cooling of the southern hemisphere (according to modeling studies, see CROWLEY, 1992). These results have been consolidated in a number of other model studies (e.g. by MAIER-REIMER ET AL., 1993). Observational evidence for these interrelations is sparse. HALL ET AL. (1997) analyzed a moored array in the western basin of the equatorial Atlantic, finding quasi-annual cycles in AABW and LNADW transport rates, with AABW maxima coinciding with LNADW minima and vice versa.

Carbon dioxide variations have been discussed (e.g. MANABE AND BROCCOLI, 1985) as a way to link both hemispheres in the framework of paleo-climate changes. VIDAL ET AL. (1999) found evidence for an opposite phase relationship of sea surface temperatures in the northern and southern Atlantic. They infer an interhemispheric connection via the global ocean circulation investigating sub-Milankovitch climate variability (i.e. on scales shorter than the 23,000 year cycle of the Earth's precession). In their examinations continental and marine sediment cores as well as ice cores serve to establish a chronology for both hemispheres; warm periods in Equatorial and South Atlantic surface waters are related to North Atlantic surface water warming after two Heinrich events[i], but in the South Atlantic the warming trend commenced 1500 years earlier. A more complete picture of interhemispheric temperature anti-phasing was presented by BROECKER (1998) and BROECKER ET AL. (1999) analyzing $\delta^{18}O$, ^{14}C and PO_4^* inventories for the deep ocean. During the Bolling-Allerod warm interval (the end of the glacial conditions north of 45°S – about 12,000 years BP) the warming that ruled Antarctica's climate for the preceding 5000 years stalled. When the Younger Dryas event forced the rest of the planet back into cold conditions (about 11,000 years BP), the warming in Antarctica resumed. BROECKER ET AL. (1999) propose an alternation between intense deep water formation in the northern North Atlantic and in the Southern Ocean as explanation. The climatic consequence was a bipolar seesaw with stronger heat release from the Southern Ocean and warming in Antarctica during periods of strong deep water formation in the southern hemisphere accompanied by weak heat release and cooling in the North and vice versa. This hypothesis of a 1500 year thermohaline oscillation is supported by the

[i] Heinrich events were massive episodic disgorgements of sediment-laden ice from the Laurentide Ice Sheet to the North Atlantic Ocean (CLARKE ET AL., 1999).

absence of external forcing of this frequency and the recurrence of ice-rafting events at approximately 1500 year intervals and has recently been consolidated by further proxy data analyses (BLUNIER AND BROOK, 2001) and model studies investigating Dansgaard-Oeschger like events[j] (GANOPOLSKI AND RAHMSTORF, 2001). COX (1989) analyzing four idealized global ocean experiments, GOOSSE ET AL. (1997) varying freshwater fluxes and FIEG (1996) and FIEG AND GERDES (2001), comparing the results of over twenty numerical experiments with both LGM and recent boundary conditions, find a similar seesawing behavior in the strength of NADW and AABW. Runs with strong northern hemisphere deep water production show weak southern hemisphere bottom water production and vice versa. A possible connection may lie in the formation region of AABW. GOOSSE ET AL. (1997) showed in a model study that AABW decreases allow the influence of NADW to increase, leading to warmer and saltier bottom water. On the other hand, this behavior is not found in every OGCM experiment. GOODMAN (1998) state explicitly, that there was no dependency of AABW on NADW variations in their model runs.

Studies with a coarse-resolution OGCM (TOGGWEILER AND SAMUELS, 1993a, 1995) suggest a dependence of the formation rate of NADW on southern hemisphere winds at the latitude band of the Drake Passage – a teleconnection called the "Drake Passage effect". Strong westerly winds cause northward Ekman drift moving upwelled deep water out of the circumpolar zone. The water pushed north must return southwards at depth; mainly below the depth of topographic ridges at the Drake Passage's latitude, as above the ridges no mean zonal pressure gradient can exist, which implies the impossibility of net southward geostrophic flow there. The only place for the formation of this compensating deep water can be the North Atlantic as the ocean is too stratified elsewhere. The enforced separation between equatorward flows at the surface and poleward flows at depth constitute an overturning of the deep ocean that is independent of vertical mixing and deep upwelling into the thermocline. Their experiments further show an dependence of the rate of NADW production on the strength of the southern hemisphere winds and in general on the existence of the Drake Passage (allowing an ACC to exist), which plays a key role for the thermal structure of the ocean's interior (TOGGWEILER AND SAMUELS, 1998). The idea of this teleconnection has been confirmed by investigations with an idealized basin model (TSUJINO AND SUGINOHARA, 1999) and a similar resolved OGCM coupled to a simple atmospheric feedback model (RAHMSTORF AND ENGLAND, 1997). The latter, though, found the NADW being modified by the influence of southern hemisphere winds instead of being controlled by them. They explain the dominance of wind forcing in the Toggweiler and Samuels experiments by the use of thermal boundary conditions, which neglect the negative temperature feedback of the atmosphere.

When trying to verify these findings comparing observational data, one has to regard the possible existence of overlying trends. FOLLAND ET AL. (1986) find a seesaw

[j] Dansgaard-Oeschger events typically start with abrupt warmings of Greenland by 5-10°C over a few decades or less, followed by gradual cooling over several hundreds or thousands of years (see BOND ET AL., 1999).

of SST differences between the North and South Atlantic on decadal time scales for the 20th century. Overlayed is a global warming trend in SST revealing different behavior between the hemispheres (MORON ET AL., 1998). Their multi-channel singular spectrum analysis of SSTs shows decadal oscillations (as well as variability on shorter time scales). The trends for both hemispheres coincide with the global trend until 1920, diverge from it until 1950, with the northern hemisphere warmer and the southern colder, intersect again in 1970 and diverge in opposite directions since. A decrease in AABW production during the 20th century from 15 to 5 Sv presently has been deducted from geochemical inventories by BROECKER ET AL. (1999) – a result that is doubted by GANACHAUD AND WUNSCH (2000).

The uncertainty how to interpret data correctly, the ambiguity of model results and the necessity of profound and reliable knowledge of the way our climate system works, point to the need of further investigations. This is, where the present study wants to set off, concentrating on numerical experiments trying to decipher global modes of the ocean circulation, identifying time scales and interaction patterns. The next chapter serves to introduce the models applied.

3. Models

3.1. Introduction

The complexity of the climate system and the limited computational resources make it necessary to restrict numerical investigations to just a number of sub-systems, processes and time scales. The first simplification compared to nature is the usage of discrete, macroscopic quantities bearing measurable qualities like temperature or velocity. The physical laws governing their interaction can be included into numerical models. The way how and to what extent this is done, strongly depends on the problem to be addressed: paleoclimate simulations need an active ocean component, while short term weather forecasts will do with prescribed SSTs. Furthermore, limits are set by the spatial extent – the circulation in a single ocean basin like the Arctic Ocean can be investigated with a finer resolution than the global circulation. And at last the time stepping needs to be adapted to the problem. This is the reason why a hierarchy of models has been developed.

For the ocean resolving explicitly all the energetic phenomena would be prohibitively expensive. Therefore, a set of specialized models have evolved, including highly idealized, process-oriented models, regional models and basin- or global-scale general circulation models. Each of them requires a distinct parameterization to account for phenomena taking place on smaller scales than those resolved explicitly while still influencing larger ones. Considerable effort has been put into the development of these parameterizations yielding models that are able to reproduce realistic features such as circulation patterns and water mass distribution. However, there are still a number of processes which are poorly represented as for instance intense boundary currents or overflows. Furthermore, models' meridional heat transports and vertical overturning circulations (MOC) exhibit a strong sensitivity to vertical and horizontal diffusion (Bryan, 1987; Schmittner and Weaver, 2001), to thermohaline forcing (Maier-Reimer et al., 1993) and to numerical algorithms (Gerdes et al., 1991). Besides all imperfection ocean models show due to a variety of reasons, they prove to be a useful tool for filling the gap left by sparse observations and the identification and examination of processes not directly accessible by measurements. Even coarse resolution models like GFDL's MOM as used by Toggweiler et al. (1989) – 3.75° × 4.5°, 12 vertical levels – are capable of reproducing rates of deep water production and meridional overturning that appear to be of realistic magnitudes.

As explained in section 2.4, sea ice has a determining effect on the freshwater budget in the polar regions and hence on deep water production. Sea ice models have been developed spanning different degrees of sophistication: purely thermodynamic ice models, those including the thermodynamic effects of snow and models taking ice dynamics into account. The latter is important to account for the substantial freshwater transports connected with sea ice exports. STÖSSEL ET AL. (1998) e.g. stated that the rate of AABW production is strongly coupled to local sea ice processes in the Southern Ocean. They found that the formulation of sea ice in the model and its forcing does not only modify the the regional stratification and convection rates but has also remote effects on the deep-ocean hydrographic properties as well as the penetration of AABW into the World Ocean.

With respect to climatic scales the atmosphere can be regarded to be in equilibrium as it has a low thermal capacity and a fast adjustment time. Therefore it is not necessary for many studies to perform time consuming calculations with a fully prognostic atmospheric model (RAHMSTORF AND WILLEBRAND, 1995). There are different methods to account for the atmospheric influence instead. When concentrating on feedback mechanisms as those explained in section 2.6 it is advisable at least to use energy balance or energy and moisture balance models (see e.g. TRENBERTH, 1992). The most simple model of the atmosphere is prescribing it as surface boundary condition for the ocean. A widely used method to do this is by restoring to a some fixed values for SST and / or sea surface salinity (SSS). It should be kept in mind that by using this kind of setup it is implicitly assumed that the atmosphere is in an equilibrium state. Therefore statements on climate variability can be made only to a limited extent.

The model combination used here aims to investigate interhemispheric interaction patterns, signal spreading in the ocean and the behavior of the ocean in response to perturbations. As there is no stress laid on feedback mechanisms involving the atmosphere the model is set up as an OGCM coupled to a dynamic-thermodynamic sea ice model. The atmospheric component is mimicked by surface forcing and restoring fields. Their details are explained in the forthcoming sections.

3.2. The Ocean Model

The ocean component used here is a general circulation model based on the second version of the “Modular Ocean Model” (MOM-2) developed at the “Geophysical Fluid Dynamics Laboratory” in Princeton (PACANOWSKI, 1995). It applies the primitive equations of thermo- and hydrodynamics. Its main features are based on works by BRYAN (1969) and COX (1984). As this model has been used widely and is fully documented in PACANOWSKI (1995) only the central equations and the approximations used will be outlined in the following section. The general model setup for the experiments performed in this study will be described in section 3.2.2; the model’s sensitivity to certain parameterizations is presented in chapter 5.

3.2.1. A Short Summary of Model Theory

The governing equations of the model are the shallow water equations derived from the Navier Stokes equations. As this model is used for investigations of slowly changing large scale processes a number of approximations is justified. Small variations in density within the ocean justify the *Boussinesq approximation*. The *anelastic approximation* allows filtering of sound waves keeping the compressibility of the equation of state. With the *traditional approximation* the local horizontal component of the earth's rotation is neglected in the horizontal and vertical momentum balance. The *hydrostatic approximation* (i.e. only the pressure gradient and gravitational forces are retained in the vertical momentum balance) is applied, as is the *thin shell approximation* (the Coriolis component and viscous terms involving vertical velocity in the horizontal momentum equations are ignored). The *spherical approximation* treats geopotential surfaces as spherical. Vertical velocities are set to zero at the surface using the *rigid lid approximation* which leads to a filtering of surface gravity waves. Furthermore molecular fluxes are neglected. For a detailed description of the approximation used, see MÜLLER AND WILLEBRAND (1989).

The model equations are calculated in spherical coordinates (λ, ϕ, z), where λ and ϕ are longitude and latitude, respectively, z denotes the depth relative to the mean radius of the earth a. Considering the assumptions made above, the model's **momentum equations** take the form:

$$u_t + L(u) - \frac{uv\tan\phi}{a} - fv = -\frac{p_\lambda}{\rho_0 a \cdot \cos\phi} + \left(\kappa_m u_z\right)_z + F^u \tag{3.1}$$

$$v_t + L(v) + \frac{u^2\tan\phi}{a} + fu = -\frac{p_\phi}{\rho_0 a} + \left(\kappa_m v_z\right)_z + F^v \quad . \tag{3.2}$$

Here u and v are the longitudinal and latitudinal velocity components, t is time, p is pressure, ρ_0 is a reference density, κ_m the vertical eddy viscosity coefficient and $f = 2\Omega\sin\phi$ is the Coriolis parameter, where Ω is the angular velocity of the earth. The independent variables in the subscripts denote partial derivatives with respect to those variables. L stands for the advection operator:

$$L(\alpha) = \frac{(u\alpha)_\lambda}{a\cdot\cos\phi} + \frac{(\cos\phi\cdot v\cdot a)_\phi}{a\cdot\cos\phi} + (w\cdot\alpha)_z \quad .$$

w is the vertical velocity component, F^u and F^v denote horizontal, nonconservative terms, representing horizontal friction and diffusion:

$$F^u = \nabla\cdot(A_m\nabla u) + A_m\left(\frac{(1-\tan^2\phi)\cdot u}{a^2} - \frac{2\sin\phi\cdot v_\lambda}{a^2\cos^2\phi}\right) \tag{3.3}$$

$$F^v = \nabla\cdot(A_m\nabla v) + A_m\left(\frac{(1-\tan^2\phi)\cdot v}{a^2} + \frac{2\sin\phi\cdot u_\lambda}{a^2\cos^2\phi}\right) \tag{3.4}$$

where A_m is the horizontal eddy viscosity coefficient.

The **conservation equations for the prognostic variables** potential temperature (T) and salinity (S) read as follows:

$$T_t + L(T) = (\kappa_h \cdot T_z)_z + \nabla \cdot (A_h \nabla T) \tag{3.5}$$

$$S_t + L(S) = (\kappa_h \cdot S_z)_z + \nabla \cdot (A_h \nabla S) \quad . \tag{3.6}$$

A_h and κ_h are the horizontal and vertical eddy diffusivity coefficients, respectively.

The **continuity equation**:

$$w_z = -\frac{1}{a\cos\phi} \cdot \left(u_\lambda + (\cos\phi \cdot v)_\phi\right) \quad , \tag{3.7}$$

the **hydrostatic equation**:

$$p_z = -\rho \cdot g \quad , \tag{3.8}$$

and the nonlinear **equation of state** for seawater:

$$\rho = \rho(T, S, p) \tag{3.9}$$

complete the set of governing equations with ρ denoting the density and $g = 9.8\ \mathrm{m\,s^{-2}}$ the gravitational acceleration. These equations are solved in a discretized form for a three dimensional grid of rectangularly shaped cells. The lateral boundary conditions are "no-slip" (i.e. $\mathbf{u}_\parallel = 0$ and $\mathbf{u}_\perp = 0$ with $\mathbf{u}_\parallel$ denoting the horizontal velocity parallel to the lateral boundaries and $\mathbf{u}_\perp$ the velocity component perpendicular to it) and "no-flux" (i.e. insulating walls and bottom for heat or salt transport). At the ocean surface, boundary conditions are applied for heat, salt and momentum (for details see section 3.5). At the ocean bottom besides the "no-flux" constraint there is a "free-slip" condition for the horizontal velocity, i.e. $\kappa_m \mathbf{u}_z = 0$ (for sensitivity studies a bottom drag has been used – see section 5.1). The vertical velocity at the bottom is given by the kinematic boundary condition $dF/dt = 0$ where $F = z + H$ and H is the depth from the ocean surface to the bottom:

$$w = -\frac{u}{a \cdot \cos\phi} H_\lambda - \frac{v}{a} H_\phi \quad .$$

The horizontal velocity (u, v) can be divided into a depth independent or external mode representing the barotropic flow $(\overline{u}, \overline{v})$ and a depth dependent internal mode representing the baroclinic flow $(\hat{u}, \hat{v})$:

$$u = \overline{u} + \hat{u}$$
$$v = \overline{v} + \hat{v} \quad .$$

Due to the rigid lid approximation, the external mode is horizontally non-divergent and can be expressed by a streamfunction Ψ:

$$\overline{u} = -\frac{1}{Ha}\Psi_\phi$$
$$\overline{v} = \frac{1}{Ha \cdot \cos\phi}\Psi_\lambda \quad .$$

Vertical averaging of the horizontal momentum equations and subsequent cross-differentiation yields an elliptic equation for the streamfunction:

$$\begin{aligned}\nabla\cdot\left(\frac{1}{H}\nabla\Psi_t\right) &= J\left(\frac{f}{H},\Psi\right)+\left[\frac{g}{\rho_0 H}\int_{-H}^{0}\int_{-H}^{z}\rho_\phi dz' dz\right]_\lambda \\ &\quad -\left[\frac{g}{\rho_0 H}\int_{-H}^{0}\int_{-H}^{z}\rho_\lambda dz' dz\right]_\phi+\tilde{G}\end{aligned}$$

where $\tilde{G}$ represents the nonlinear and dissipation terms; J is the Jacobi operator given by $J(A,B)=(a^2\cos\phi)^{-1}(A_\lambda B_\phi - A_\phi B_\lambda)$.

The model is set up on an Arakawa B grid (BRYAN, 1969; MESINGER AND ARAKAWA, 1976; COX, 1984) containing scalar and vector cells. This arrangement is shown in Fig. 3.1 for one horizontal level. Grid points in the middle of a cell define the locations of tracer quantities or zonal and meridional velocity components, respectively. The vertical velocities are calculated on grids shifted vertically by half a grid size (for a detailed discussion see PACANOWSKI, 1995).

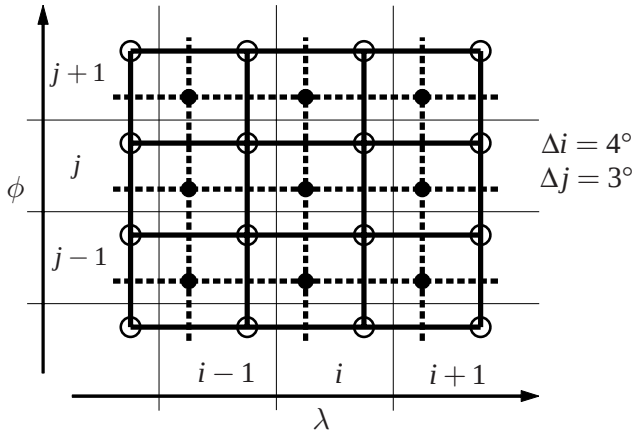

Figure 3.1.: *Representation of scalar and vector points of one depth level of MOM's Arakawa B grid; thick solid lines denote the vector, dashed lines the scalar grid. Points having the same indices are contained within the same boxes bounded by the thin solid lines. Vector points are symbolized by open circles, scalar points by filled ones. λ is longitude, ϕ is latitude (figure courtesy of Katrin Meißner).*

3.2.2. Model Configuration

In the ocean a wide range of time scales exists; from fast moving internal gravity and external Rossby waves to slow diffusion of water mass properties below the main thermocline. Numerical integrations to an equilibrium state[a] can therefore be lengthy. To

[a] Equilibrium state, as used here, is meant to be the state in which large scale advective adjustments have been completed. As a rough measure for its time scale, the model's volume – $1.34\cdot 10^{18}\mathrm{m}^3$ – was divided

overcome this problem a method called distorted physics has been implemented in MOM. The equations are solved asynchronously using different time steps for the external mode, for the internal mode and for the tracers. The method attempts to compress the model's frequency band in two ways. Gravity waves and Rossby waves are decreased in speed, thereby eliminating very high frequencies. This part has been applied here. At the other end of the spectrum the very long time scales could be reduced by shrinking the local time scale of the abyss relative to the upper ocean levels. This can be interpreted as a decrease in the abyssal heat and salt capacity without altering the mixing and transport of these quantities. The equilibrium solution with distorted physics is equivalent to a non-distorted solution, as only local derivatives with respect to time are changed (BRYAN, 1984).

The horizontal resolution of the model is 4° in longitude and 3° in latitude. There are 20 vertical levels, monotonically increasing from about 50 m spacing near the surface to about 450 m near the bottom at 5000 m depth (see Table 3.1).

Level	Δz [m]	z [m]	Level	Δz [m]	z [m]
1	51.23	25.00	11	265.64	1354.38
2	56.13	77.46	12	296.55	1635.67
3	65.79	137.52	13	326.30	1947.47
4	80.00	209.05	14	354.18	2288.27
5	98.39	297.25	15	379.49	2655.82
6	120.51	405.82	16	401.61	3047.25
7	145.82	538.27	17	420.00	3459.05
8	173.70	697.47	18	434.21	3887.25
9	203.45	885.67	19	443.87	4327.46
10	234.36	1104.38	20	448.77	4775.00

Table 3.1.: *The ocean model's vertical resolution: Δz: layer thickness, z: depth of scalar and vector points.*

The model's topography was taken from DANABASOGLU AND MCWILLIAMS (1995). Only four land masses are present: one big continent (including Europe, Africa, Asia and the Americas) and three islands: Australia, Antarctica and (to avoid numerical problems) the North Pole. Some straits and bays were deleted or closed: Greenland is connected to North America, the Bering and Gibraltar Straits are closed. Others, for instance the Indonesian Throughflow, were widened artificially. The bottom topography was obtained by interpolating a data set from the NOAA National Geophysical Data Center. This averaged data set was modified allowing only depths greater than 2500 m. The resulting fields were smoothed (for a detailed description see DANABASOGLU AND MCWILLIAMS,

by an approximate worldwide deep water production rate of 40 Sv yielding 1060 years. To reach an equilibrium state having a diffusive time scale in mind, a much longer integration time was necessary: an estimate based on the quotient of the square of a typical ocean depth of 3 km and a vertical diffusivity coefficient of $5 \cdot 10^{-5} \mathrm{m}^2/\mathrm{s}$ would be about 5700 years.

1995). Due to these modifications it is avoided to resolve coastal topography and numerical instabilities due to topographical roughness are prevented. The only "shelf" areas introduced into the model (differing here from DANABASOGLU AND MCWILLIAMS, 1995) were the Barents Sea and the transition from the North Atlantic to the Arctic Ocean to create a kind of "Greenland-Scotland-Ridge". The resulting topography is sketched in Fig. 3.2.

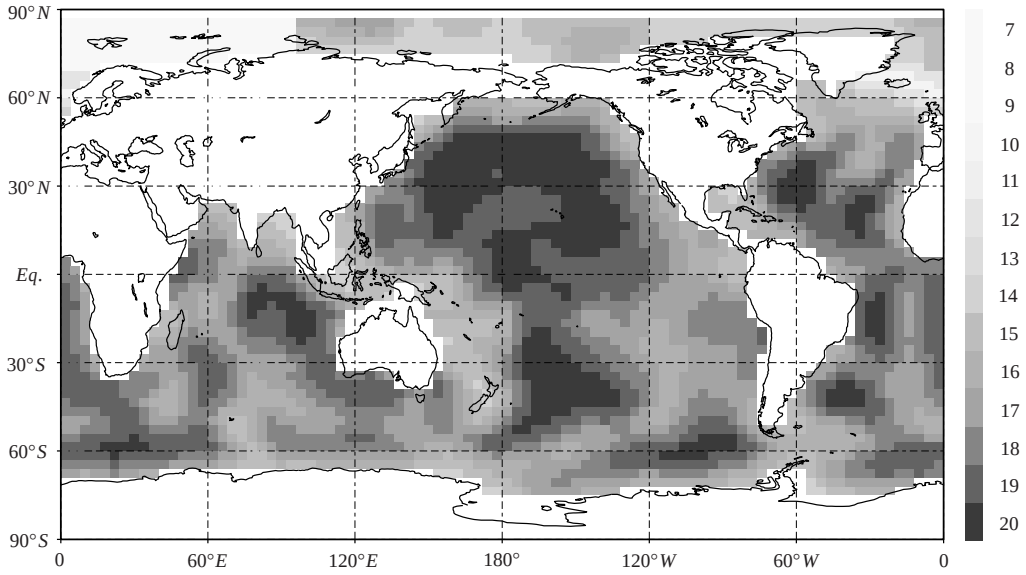

Figure 3.2.: *Topography of the ocean model: the number of depth levels for tracer points is shaded.*

Description	Parameter	Value	Unit
Vertical eddy viscosity coefficient	κ_m	10^{-3}	m^2/s
Horizontal eddy viscosity coefficient	A_m	10^6	m^2/s
Vertical eddy diffusivity coefficient	κ_h	0	m^2/s
Horizontal eddy diffusivity coefficient	A_h	0	m^2/s
Restoring time constant for SSS	Δt_{rS}	96	days
Length of time step for tracers	τ	43,200	s
Length of time step for internal mode velocities	τ	1728	s
Length of time step for external mode velocities	τ	864	s
Bottom drag coefficient	c_{dbot}	0	

Table 3.2.: *Parameters used in the ocean model for the control run.*

The ocean parameters for the control run (referred to as "CTRL" in the following) have been chosen according to the values used by MEISSNER (1999) to allow to compare the results of the setup used here with her model version that applies a purely thermodynamic sea ice component and is coupled to an energy and moisture balance model. The

parameter values are listed in Table 3.2. Sub-grid scale mixing for momentum is implemented with constant values for the horizontal and vertical mixing coefficients. Filtering is applied only to the streamfunction north of 79.5°N using a symmetric finite impulse response filter. Tracer advection employs the FCT algorithm, convection the Rahmstorf scheme. Details of these settings will be explained in section 5.1.

3.3. The Ice Model

A dynamic-thermodynamic sea ice model with a viscous-plastic rheology (HARDER, 1996; HARDER ET AL., 1998) is the second climate system component used for the present study. It is based on the fundamental works on the dynamics (HIBLER III, 1979) and thermodynamics (SEMTNER, 1976; PARKINSON AND WASHINGTON, 1979) of large scale sea ice models. The model code was modified to enable a coupling to global domain components. Another manipulation of the code was necessary to enable calculations on a global grid with cyclic boundary conditions. The following subsection explains the theory of these components – a more detailed model description can be taken from the above publications.

3.3.1. The Model Equations

Sea-ice is considered to be a two-dimensional continuum in this model. It is described by the mean ice thickness h_I (ice volume per area), the ice concentration A_I (spatial coverage) and the ice drift velocity $\mathbf{u}_I$. For the prognostic snow layer the variable h_s denoting the snow thickness is included. The evolution of the ice and snow cover is given by the **continuity equations**:

$$\frac{\partial h_I}{\partial t} + \nabla \cdot (\mathbf{u}_I h_I) = S_h \tag{3.10}$$

$$\frac{\partial A_I}{\partial t} + \nabla \cdot (\mathbf{u}_I A_I) = S_A \tag{3.11}$$

$$\frac{\partial h_s}{\partial t} + \nabla \cdot (\mathbf{u}_I h_s) = S_s \quad , \tag{3.12}$$

where S_h, S_A and S_s are the thermodynamic source and sink terms. S_h is determined from an energy budget at the ice surface and an approximation for the heat conduction through the ice. The energy balance of the oceanic surface layer then yields:

$$Q_a + Q_o + \rho_I L_I S_h = 0 \quad . \tag{3.13}$$

Q_a and Q_o are the net heat fluxes from the atmosphere and the ocean into the surface layer (defined here including the ice cover); ρ_I is the density of sea ice, L_I its specific latent heat. For a detailed treatment of the heat fluxes at surface and bottom of the ice,

the energy balance (3.13) is split into two balances (SEMTNER, 1976). This yields

$$Q_a + Q_c + \rho_I L_I \left(\frac{\partial h_I}{\partial t}\right)_a = 0 \tag{3.14}$$

for the upper boundary between ice and atmosphere and

$$Q_o - Q_c + \rho_I L_I \left(\frac{\partial h_I}{\partial t}\right)_w = 0 \tag{3.15}$$

for the bottom. Q_c is the conductive heat transport through the ice. The net atmospheric heat flux Q_a is composed of solar and long wave radiation as well as of latent and sensible heat fluxes.

Sources and sinks of the ice concentration are described by an empirical function

$$S_A = \frac{1 - A_I}{h_0} G_h + \frac{A_I}{2h_I} M_h \tag{3.16}$$

with $G_h = \max(S_h, 0)$ being the freezing rate and $M_h = \min(S_h, 0)$ the melting rate. The first term on the right side describes the freezing of sea ice. Horizontal freezing is proportional to the area of open water $(1 - A_I)$ and the freezing rate. The empirical parameter h_0 controls the velocity of lead closing. The second term, covering the melting process, is proportional to the melting rate and inversely proportional to the actual thickness of the model's ice floe h_I/A_I. This formulation accounts for the fact that thin ice leads to a faster decrease of ice covered areas compared to thicker ice floes.

The source of S_s is precipitation while its sinks are provided by the energy budget mentioned before. Melting processes at the ice surface first change the snow cover, the ice thickness is only affected, when all snow has vanished.

The ice drift velocity $\mathbf{u}_I$ is determined from the **momentum balance**:

$$m\frac{D\mathbf{u}_I}{Dt} = \tau_a + \tau_w - mf\vec{k} \times \mathbf{u}_I + \mathbf{F} - mg\nabla H \quad . \tag{3.17}$$

$-mf\vec{k} \times \mathbf{u}_I$ is the Coriolis force, m the ice mass per area, $\mathbf{F}$ represents the internal ice forces and $-mg\nabla H$ is the force due to the tilt of the ocean surface H. The surface tilt ∇H is derived from the ocean current $\mathbf{u}_w$ via geostrophy (in the coupled model version the geostrophic velocity of the second layer of the ocean is used). τ_a is the wind stress and is supplied from an external data file (see section 3.5). τ_w denotes the oceanic drag and is defined as follows:

$$\tau_w \quad = \quad \rho_w c_w |\mathbf{u}_w - \mathbf{u}_I| [(\mathbf{u}_w - \mathbf{u}_I)\cos\Theta + \mathbf{k} \times (\mathbf{u}_w - \mathbf{u}_I)\sin\Theta] \quad ,$$

where ρ_w is the density of water, c_w is the drag coefficient and $\mathbf{u}_w$ is the ocean velocity. $\mathbf{k}$ is the vertical unit vector and Θ describes the deflection angle between drag and ocean velocity (set to Θ =25° for geostrophic ocean currents).

A viscous-plastic rheology with an elliptical yield curve describes the internal ice forces **F** as the divergence of the stress tensor σ:

$$\mathbf{F} = \nabla \cdot \sigma \tag{3.18}$$

where $\sigma = \sigma(\dot{\varepsilon}, \varepsilon)$ is a function of the deformation ε and the deformation rate $\dot{\varepsilon} = \nabla \mathbf{u}$. The rheology connects kinematics (described by ε and $\dot{\varepsilon}$) and ice dynamics (**F**). It is formulated in this model in a way generally valid for viscous isotropic media (HIBLER III, 1979; KREYSCHER, 1998):

$$\sigma_{ij} = 2\eta\dot{\varepsilon}_{ij} + \left((\zeta - \eta)(\dot{\varepsilon}_{11} + \dot{\varepsilon}_{22}) - P/2\right)\delta_{ij} \quad , \tag{3.19}$$

with $i, j \in \{1, 2\}$. $\dot{\varepsilon}$ describes the fluid's non-rotational deformation, η is the shear viscosity, ζ denotes the bulk viscosity, P the pressure and δ_{ij} is the Kronecker symbol. To account for the plastic behavior of sea ice η and ζ are set to be non-linear functions of the deformation rate. The definition of the non-linear viscosities for an elliptical yield curve reads as follows:

$$\zeta = \frac{P_p}{2(\Delta + \Delta_{min})} \tag{3.20}$$

$$\eta = \frac{P_p}{2\epsilon^2(\Delta + \Delta_{min})} \tag{3.21}$$

$$P = \frac{P_p \Delta}{2(\Delta + \Delta_{min})} \quad . \tag{3.22}$$

P_p is the large scale ice strength parameterized by:

$$P_p(h_I, A_I) = P^* h_I \exp\left(-C(1 - A_I)\right) \quad . \tag{3.23}$$

The values for the constants P^* (ice strength parameter) and C (ice concentration parameter), as well as for ϵ (eccentricity of the yield curve) and Δ_{min} (regime parameter) are empirical and have been determined by sensitivity studies (see section 3.3.2). They are given in Table 3.3. $\Delta = \Delta(\dot{\varepsilon})$ is a kinematic measure for the ice cover's total deformation:

$$\Delta(\dot{\varepsilon}) = \sqrt{(\dot{\varepsilon}_{11}^2 + \dot{\varepsilon}_{22}^2)(1 + \epsilon^{-2}) + 4\epsilon^{-2}\dot{\varepsilon}_{12}^2 + 2\dot{\varepsilon}_{11}\dot{\varepsilon}_{22}(1 - \epsilon^{-2})} \tag{3.24}$$

The eccentricity of the elliptic yield curve (ϵ) gives the relation between convergence and shear. For a more detailed discussion of the properties of the applied rheology see HARDER (1996) and KREYSCHER (1998).

3.3.2. The Model Setup

The ice model is run on the same grid as the ocean model. The model domain was divided into two parts calculating separately on both hemispheres poleward from 45°. The time step chosen was the same as the tracer time step of the MOM. The original model was designed to be calculated on a rotated grid for one hemisphere only. Therefore

Description	Parameter	Value	Unit
Thermodynamical parameters:			
Density of sea ice	ρ_I	910	$\mathrm{kg\,m^{-3}}$
Density of snow	ρ_s	300	$\mathrm{kg\,m^{-3}}$
Density of water	ρ_w	1000	$\mathrm{kg\,m^{-3}}$
Specific melt energy for sea ice	L_I	$3.34 \cdot 10^5$	$\mathrm{J\,kg^{-1}}$
Lead closing parameter	h_0	1	m
Dynamical parameter:			
Drag coefficient for the ocean	c_w	$5.5 \cdot 10^{-3}$	
Rheological parameters:			
Ice strength NH	P^*	15,000	$\mathrm{N\,m^{-2}}$
Ice strength SH	P^*	22,500	$\mathrm{N\,m^{-2}}$
Ice concentration parameter	C	20	
Eccentricity of the yield curve	ϵ	2	
Regime parameter	Δ_{min}	$2 \cdot 10^{-9}$	$\mathrm{s^{-1}}$
Radiation parameters:			
Albedo for open water	α_w	0.1	
Albedo for ice (without snow) NH	α_I	0.65	
Albedo for ice (without snow) SH	α_I	0.75	
Albedo for melting ice (without snow) NH	α_m	0.60	
Albedo for melting ice (without snow) SH	α_m	0.66	
Albedo for snow NH	α_s	0.80	
Albedo for snow SH	α_s	0.85	
Albedo for melting snow NH	α_{sm}	0.70	
Albedo for melting snow SH	α_{sm}	0.75	

Table 3.3.: *Parameters used in the ice model. NH: northern hemisphere; SH: southern hemisphere.*

the model code had to be modified to serve the needs of a global approach. This included the implementation of cyclic boundary conditions as well as changing parameterizations from single values to fields holding different numbers for the two hemispheres.

Like the ocean model, the sea ice component contains various parameters to be tuned. Sensitivity studies performed with a model version coupled to a simplified ("toy") ocean (results not shown here explicitly) yielded the values listed in Table 3.3. These investigations were validated comparing ice concentrations to SSM/I (Special Sensor Microwave/Imager) satellite data (NSIDC, 1996). Results of this comparison are explained for the control run in chapter 4. For C, ϵ and Δ_{min} the values used by HARDER (1996) were taken. The ice strength parameter P^* has different values for the Arctic and Antarctic due to the fact, that the ice classes found there in reality differ substantially. Therefore it was necessary to tune these values separately for a realistic simulation. The albedo, i.e. the capacity to reflect incoming radiation, also differs between the hemispheres to account e.g.

for the effects of meltponds on multi-year ice in the Arctic. The albedos chosen for the Arctic are identical to those used by HARDER (1996), values for the Antarctic are taken from FISCHER (1995).

3.4. Coupling

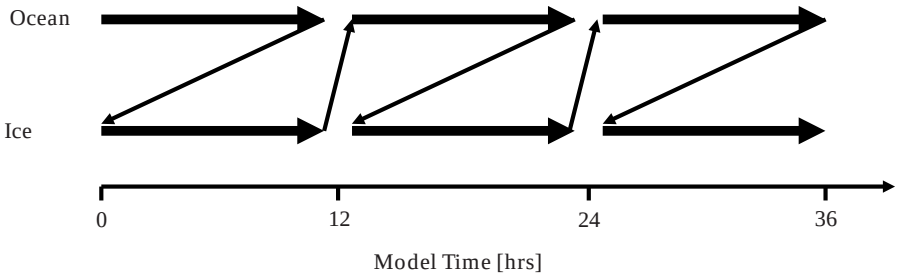

Figure 3.3.: *Time stepping of the coupled model. The ocean model calculates one tracer time step (12 hrs), gives the calculated values to the ice model, which performs the same time step. When finished, it gives the relevant fields to the ocean, starting the next time step.*

Coupling two models requires an interface for the exchange of quantities the submodels need as "external" input. The ocean supplies the sea ice with SST and values for geostrophic velocity. The ice model, in turn, feeds MOM with internal stresses, information about evaporation, fresh water fluxes and net heat fluxes. As both models use the same grid there was no need for interpolating fields. Also, time stepping is identical (the tracer time steps being the longest in the ocean). This means the exchange between the two components takes place every 12 hours as displayed by Fig. 3.3. This time-marching coupling procedure is illustrated by considering simplified one-dimensional momentum equations of the form:

$$\frac{\partial u_I}{\partial t} = F(u_I) + \frac{\partial p}{\partial x} - D(u_I - u_w) + \tau_a \tag{3.25}$$

$$\frac{\partial u_w}{\partial t} = -\frac{\partial p}{\partial x} + [F(u_I) + \tau_a] \quad , \tag{3.26}$$

where u_I and u_w are the ice and the ocean velocities, respectively, $F(u_I)$ denotes the nonlinear and rheology terms and D represents the drag term. As the idea is to center the exchange terms in time to the degree possible, the coupling for a leapfrog time-stepping is as follows:

$${u_I}^{i+1} - {u_I}^{i-1} = 2\Delta t \left[F({u_I}^{i+1}) + \frac{\partial p^i}{\partial x} - D({u_I}^{i-1} - {u_w}^{i-1}) + {\tau_a}^i \right] \tag{3.27}$$

$${u_w}^{i+1} - {u_w}^{i-1} = 2\Delta t \left[\frac{\partial p^{i+1}}{\partial x} + F({u_w}^i) + {\tau_a}^i \right] \quad . \tag{3.28}$$

The superior indices i, $i-1$ and $i+1$ denote the time steps. To eliminate splitting problems, every 17 steps a forward step is used in both models. For the conservative equations

of both models the first level is integrated forward in time. This produces a tendency for SST, SSS and the ice thickness. In a splitting procedure the SST is then set to freezing and an equivalent amount of ice is melted, while the SSS is adjusted accordingly. This implicit procedure forces the ice cover and the SST to stay in a balance and at the same time ensure conservation. For a more detailed description of sea ice-ocean coupling see HIBLER III AND BRYAN (1987).

3.5. External Forcing and Initial Conditions

The surface forcing fields consist of monthly mean data sets which are interpolated linearly for the actual time step within the model.

The SSS fields were obtained from the climatology of LEVITUS (1982)[b]. The data was averaged over the upper 50 m to match the first vertical level thickness and was transfered onto the model grid by horizontal averaging. The tracer equation for salinity at the shallowest grid level is linearly restored to the surface forcing fields with a time constant Δt_{rS} as listed in Table 3.2.

All other forcing fields have been derived from a validated 15 year set of assimilated data for the period 1979 to 1993 provided by the re-analysis project of the European Center for Medium-Range Weather Forecasts (ECMWF) which was prepared in the framework of the BMBF ocean model intercomparison project (FRITZSCH ET AL., 2000). The parameters used here are: 2-m-temperature, 2-m-dew-point-temperature, total cloud cover, precipitation, scalar winds and the horizontal windstress components. The data have been processed to construct a "typical" year from different forecast cycles. Therefore these cycles were first averaged to daily values and then filtered by a Gaussian filter method (e.g. SCHÖNWIESE, 1992). This leads to a splitting of the data into a low pass and a high pass. The low pass was averaged to a single year. From the high pass a particular year describing maximum variability was selected and added to the low pass. The advantage of this technique is the preservation of the variability of daily values which would be leveled out by mere averaging. The data sets used here are monthly means derived from this typical year interpolated onto the model's grid.

The initial fields for potential temperature and salinity were constructed in the way described above for SSS interpolating the Levitus climatology horizontally and vertically onto the ocean model's grid. To start the model runs the monthly means for January were used.

[b] This data set was provided together with the model code. Its overall structure is very similar to that of younger data sets. Furthermore, it has been used in a great number of model experiments and has proved to be a reliable basis for calculations.

4. The Control Run

This chapter is dedicated to present the main features of the model run that will be taken as a reference during the upcoming part of this study (referenced as “CTRL” then). Its setup has been introduced in the previous sections. The model run started from initial temperature and salinity fields provided by the LEVITUS (1982) climatology as described in section 3.5, where also details about surface boundary conditions can be found. For the initial ice fields values for concentration and thickness gained by uncoupled runs of the ice model were used. The integration started with values for January.

The model has been run for 5500 years. After about 3000 to 3500 years it reached an equilibrium state as defined in section 3.2.2. The run then was continued for another 2000 years as a control case for the experiments with altered boundary conditions that will be described in chapter 7. In the following, the main features of the model in equilibrium will be discussed. The results presented are taken from a 500 year mean for the model years 3500 to 3999. This allows to use them in chapter 7 as a reference.

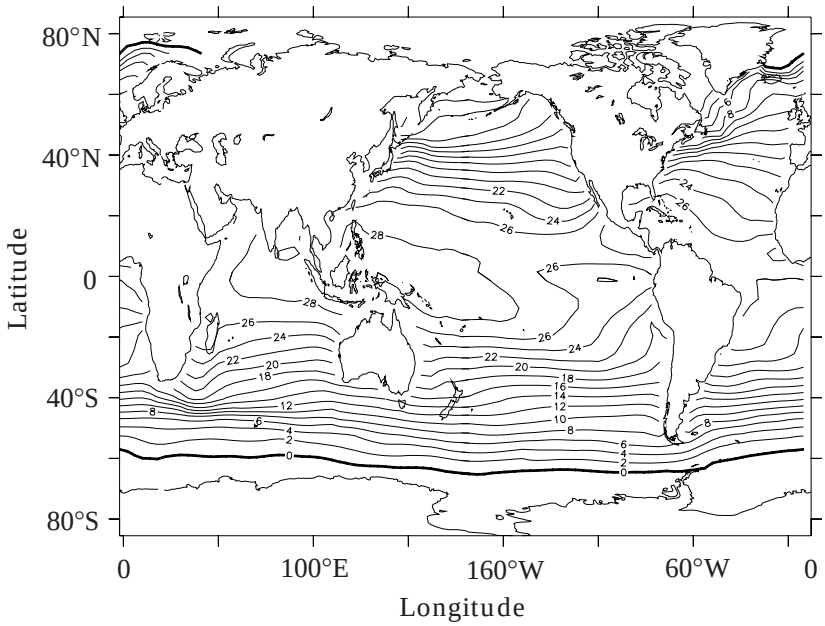

Figure 4.1.: *Mean potential temperatures in the first level in °C for the integration years 3500 to 3999 of the control run.*

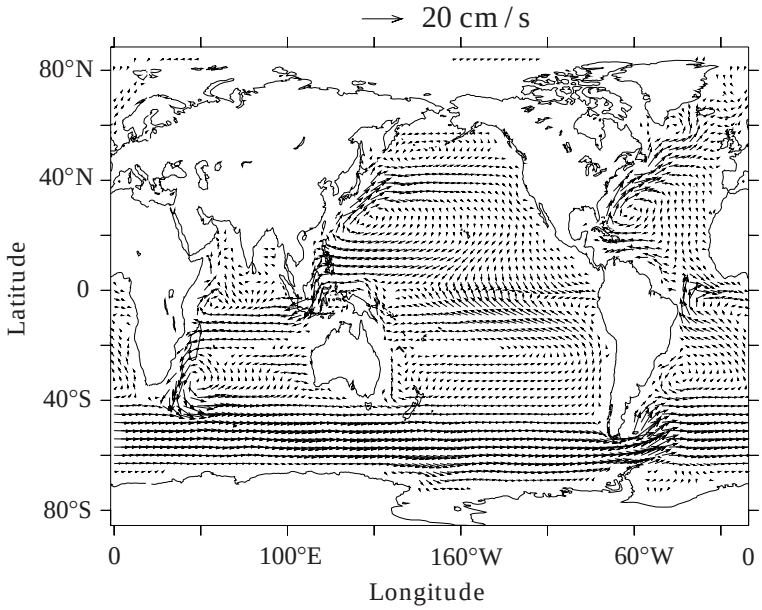

Figure 4.2.: *Mean velocities in the second level for the integration years 3500 to 3999 of the control run; the reference arrow represents 20 cm/s.*

Fig. 4.1 shows the potential temperature field for the model's first level. It reflects the climatological state. Maxima are located in the Tropical Indian and Western Pacific Ocean. Atlantic and Pacific Ocean show a zonal temperature gradient caused by upwelling of cold water at the eastern boundaries. The upwelling regions are close to reality with the exception of the West African shore. There, no upwelling takes place, leading to exaggerated temperatures. The northern hemisphere's big current systems, the Kuroshio in the Pacific Ocean and the Gulf Stream in the Atlantic Ocean are reproduced properly (as far as possible within the scope of the coarse resolution; compare second level velocities in Fig. 4.2[a]). The northbound transport of warm surface waters along the east coast of North America, across the basin and into the Nordic Seas compares to observational evidence (see section 2.1). In the Northern Pacific Ocean the model temperatures are too high. In the Indian Ocean the southbound Agulhas Current is very pronounced. This feature (which is not expected within a model of this resolution) can presumably be credited to the FCT advection scheme (that will be described in section 5.1). The SST field in the Arctic Ocean is very close to the freezing temperature in accordance with observational values (LEVITUS, 1982). Around Antarctica, the 0°C-isotherm is too close to the continent, which implies too high temperatures in the Southern Ocean between 50° and 60°S. In deeper layers the temperature field is too warm in the high latitudes of both hemispheres.

The overall structure of the subtropical and subpolar gyres is close to reality. This can also be seen in the barotropic streamfunction of Fig. 4.3. The strength of the Atlantic

[a]Second level velocities are displayed here, as the top level is completely determined by the wind forcing.

subtropical gyre is too weak. The flow field of the ACC with its northward deviation east of the Drake Passage is also properly reproduced. Its volume transport of about 235 Sv is overestimated, but still in the (upper) range of model results (compared for instance to the 240 Sv of BOVILLE AND GENT, 1998).

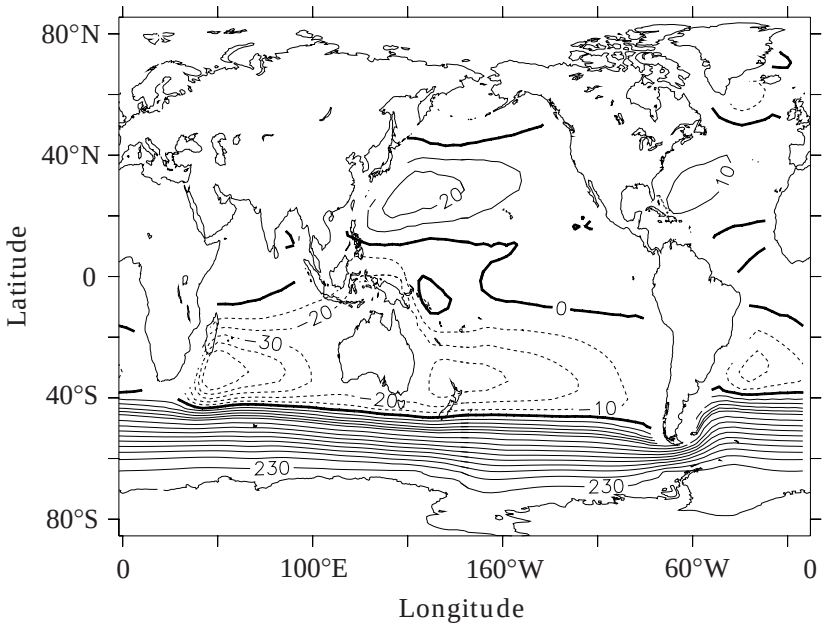

Figure 4.3.: *Vertically integrated mass transport streamfunction averaged over the integration years 3500 to 3999 of the control run. Contour interval is 10 Sv for values between 0 and* $\pm$*50 Sv, 20 Sv elsewhere, dashed contours denote negative values.*

Surface salinities in the world ocean (Fig. 4.4) are characterized by high values in the subtropics due to high (local) evaporation and lower SSS values in the tropics and higher latitudes. At the same time, a remarkable difference between the Atlantic and the Pacific Ocean exists: the salinities are generally higher in the Atlantic Ocean. The subtropical salt signal is transported by the strong currents far to the north along the European coast into the Northern Seas. This overall structure is reproduced correctly by the model, also covering more regional structures like the intrusion of fresh Pacific waters through the Indonesian Passage into the Indian Ocean. Deviations from reality are found in the big river estuaries of the Amazon, Congo, Ganges, Yangtse and the Siberian rivers, whose contribution to the freshwater budget is not sufficiently reproduced. However, this effect is limited to the model's first level. In general, the surface salinities in the Arctic along the Siberian and Canadian coast are to high. The SSS around Antarctica exceeds the observed values to a lesser extent. At deeper levels the model produces too high salinities throughout the entire ocean. Features like the spreading of intermediate water are reproduced, but their salinities are too high. Especially in the Arctic there are deviations from observational data of up to 2 psu. Around Antarctica the belt between 50° and 60°S shows salinities that are about 1 psu to high. In the abyssal layers the trend continues with de-

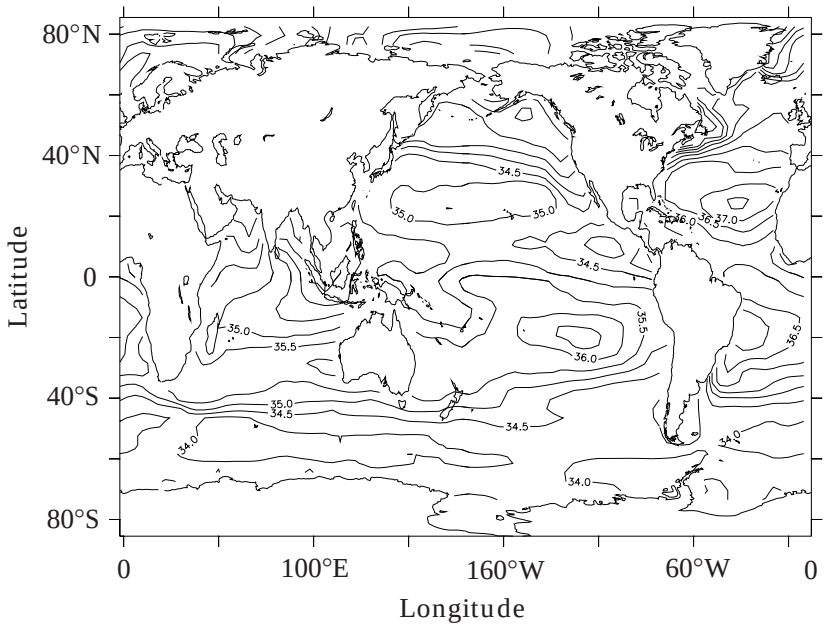

Figure 4.4.: *Mean salinities in the first level in psu for the integration years 3500 to 3999 of the control run.*

creasing amplitudes. Here mainly the Pacific and Indian basins are affected, whereas the model simulates the Atlantic Ocean more closely to reality (LEVITUS, 1982).

Meridional overturning streamfunctions for the Atlantic and the global ocean are shown in Fig. 4.5. The latter shows two shallow cells that upwell at the equator. They are driven by the convergence of the Ekman transport due to easterly trade winds. Most of this water sinks within 30° of the equator. Ekman divergence in the subpolar zones produces two adjoint counter-rotating cells. In the northern hemisphere this cell is quite weak as it is opposed by the strong North Atlantic thermohaline circulation. The corresponding cell in the southern hemisphere is called the Deacon cell. It is connected in intermediate depths to the thermohaline cell intruding from the North. The accumulation of isolines in the upper layers at 60°S indicates strong upwelling there. The southernmost cell represents the formation of AABW. It extends to the sea floor and spreads far north across the equator to 50°N. The small surface cell north of 65°N is extremely weak and without any importance for the global circulation. The overturning is dominated by downwelling north of 50°N, associated with the strong Atlantic cell with a maximum of more than 24 Sv centered in about 1000 m depth at 50°N. Its southward branch represents the transport of NADW. Only about 16 Sv of the 24 Sv enter the southern hemisphere, resulting in 8 Sv of upwelling before the equator is reached. The meridional overturning streamfunction of Fig. 4.5 is in qualitative agreement with the e.g. investigations by DANABASOGLU AND MCWILLIAMS (1995) and MEISSNER (1999), even though the maximum is slightly higher than their figures. For the export of deep water out of the Atlantic basin observational values give approximately 20 Sv (SCHMITZ AND MCCARTNEY,

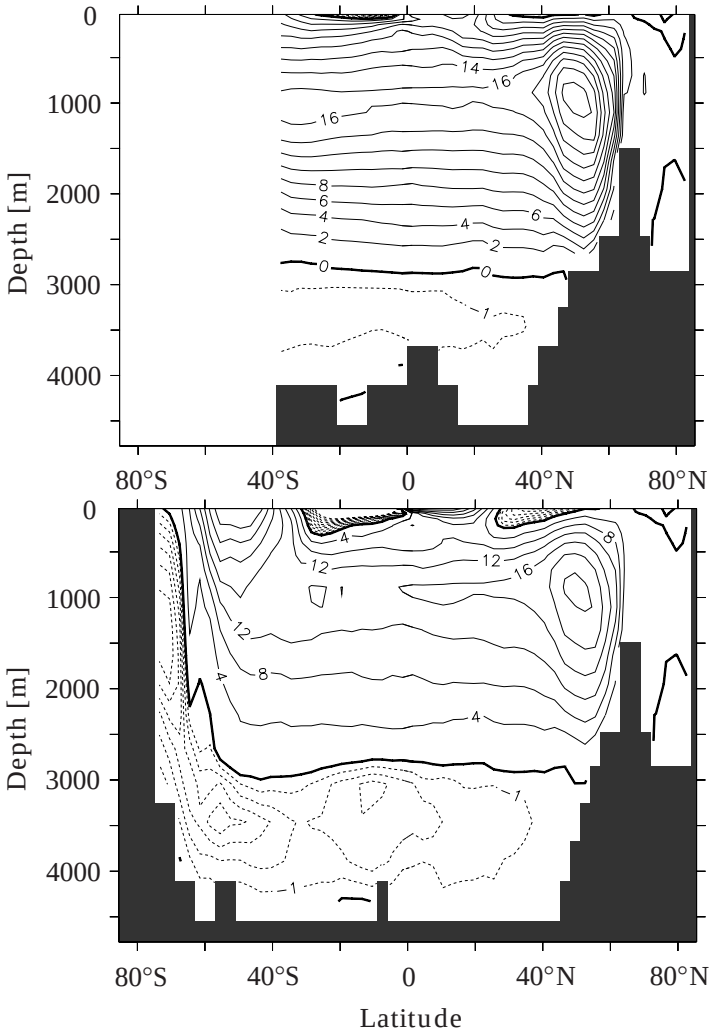

Figure 4.5.: *Mean meridional overturning streamfunction in Sv for the integration years 3500 to 3999 of the control run; top: for the Atlantic Ocean; bottom: for the global ocean. Contour interval is 2 Sv (4 Sv) for positive values in the Atlantic (global), 1 Sv for negative values.*

1993; SCHMITZ, 1995, compare section 2.1). The present study shows 16 Sv, the model of MEISSNER (1999) produced about 10 Sv.

Meridional temperature and salinity sections across the Atlantic are shown in Fig 4.6. Compared to climatological values (LEVITUS, 1982) the thermocline is sharper, but a little too shallow. At intermediate depths the Atlantic is too warm, while the bottom water is too cold. The signature of Antarctic Intermediate Water is simulated well for a coarse resolution model. Nevertheless, the intermediate water tongue is shallower than in reality and its salinity values are 0.3 to 0.4 psu higher. The whole Atlantic basin is too salty. The reason may be found in the high salinity of the surface water masses south of the Greenland-Scotland-Ridge that are subducted when deep water is formed.

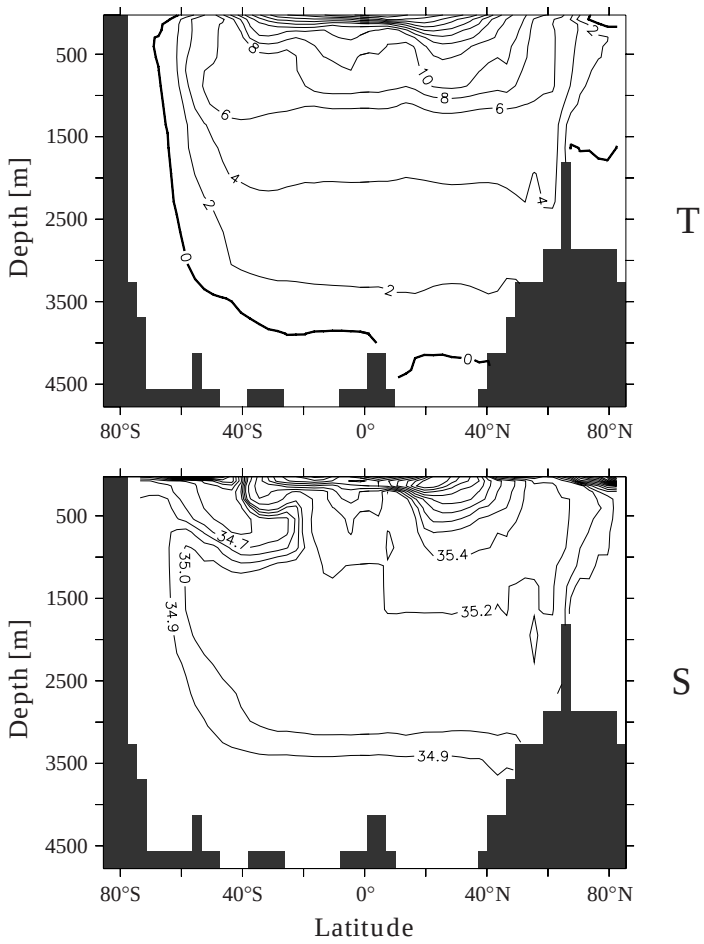

Figure 4.6.: *Atlantic zonal mean of potential temperature (top) and salinity (bottom) for the integration years 3500 to 3999 of the control run; contour interval is 2°C for temperature, 0.2 psu for salinity, between 34 and 35 psu it is 0.1 psu.*

OGCMs are often evaluated by their ability to reproduce water mass transport pathways. To follow the path of deep water a passive tracer was introduced into the model in year 3490. Its concentration was set to a constant value of one at the surface level. Fig. 4.7 gives the concentration of the tracer in 1950 m depth 300 years after it has been introduced into the model. Concentration values of one indicate that the whole water at this grid box has been replaced by water that has been in contact with the surface within the 300 years. The maximum concentrations are found in the Atlantic close to the Greenland-Scotland-Ridge and spreading southward from there along the western boundary. At 30°S the concentration plume turns east and follows the northern edge of the ACC circling the entire Southern Ocean. Further concentration maxima exist in the Arctic Ocean, which is filled with subducted water. The entire Pacific Ocean north of 30°S shows concentration values smaller than 0.1. 300 years are not enough to fill this basin with water masses originating from the surface layers.

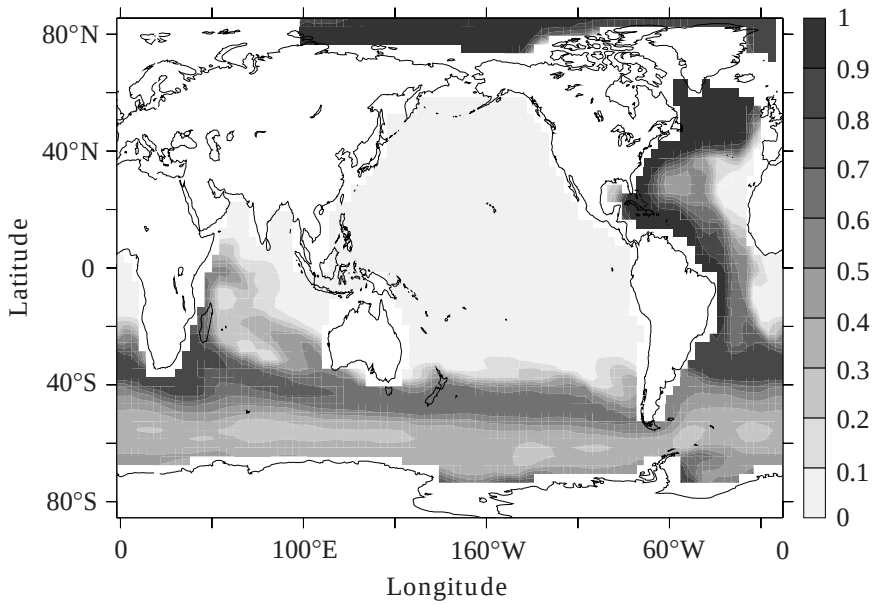

Figure 4.7.: *Concentration of a passive tracer introduced over the whole surface starting from model year 3490 after 300 years of integration in 1950 m depth.*

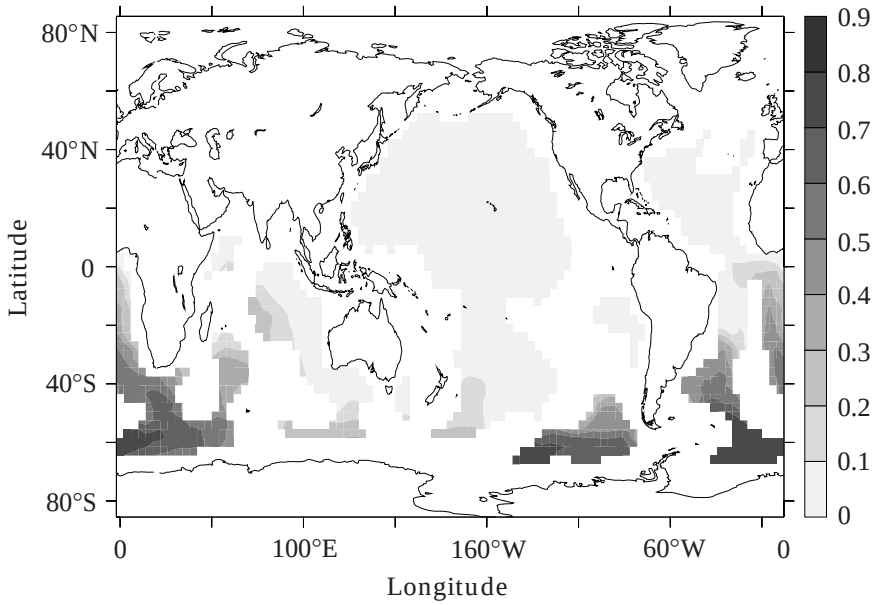

Figure 4.8.: *As in Fig. 4.7, for 3800 m depth.*

Other maxima are located in the Ross Sea and the Weddell Sea. They are confined to very small areas. This indicates that the sinking water masses are not staying at this level, but proceed to greater depths. Fig. 4.8 gives the tracer concentrations at 3.8 km depth. No signals can be seen that point to water masses of northern hemisphere origin. Hence,

NADW is entirely confined to higher levels. But waters subducted in the Southern Ocean have filled the adjacent basins and slowly proceed north. While during 300 years water of northern hemisphere origin has already spread around the globe with the ACC, southern hemisphere bottom water has only reached the equator in the Atlantic and Indian Oceans. The pathways of NADW and AABW in the model are well represented and confirm the ideas derived from observations (compare chapter 2 and the references there).

Monthly means of sea ice concentration are shown in Fig 4.9 for February and August. Comparison with satellite data (NSIDC, 1996) reveals that the winter concentrations are simulated well in the central Arctic basin. The ice free region along Scandinavia is a result of the warm North Atlantic Current. The observed winter sea ice cover along the East coast of Greenland is reproduced only in its northern part; south of the Greenland-Scotland-Ridge the concentrations are too low. The ice cover in the Labrador Sea is realistic. In the North Pacific the ice concentrations are underestimated. In wintertime the northern hemisphere's sea ice[b] covers $8.8 \cdot 10^6\,km^2$, while GLOERSEN ET AL. (1992) name an observational value of $14.5 \cdot 10^6\,km^2$. In summer, the difference between modeled and observed values is about one third less with $7.9 \cdot 10^6\,km^2$ against $11.5 \cdot 10^6\,km^2$. These differences are not solely due to a deficit in modeling the sea ice cover. Due to the resolution of the model grid the model underestimates the Arctic Ocean's size. Large parts of the shelf areas, the Canadian Archipelago and the North Pole are not resolved by the model. This leads to an overall Arctic ice extent that is lower than figures derived from observations. In boreal summer the ice cover is restricted to the central Arctic Ocean and the north-eastern Greenland shore, both in model and reality. The concentrations in the area of the Chukchi Sea and the Canadian Basin are too high. SSM/I data (NSIDC, 1996) give values reaching from one in the central basin to zero on the shelves. The annual cycle of the ice extent with its extremes in March and September is realistic. Summarizing, it can be stated, that the northern hemisphere ice concentrations and extent are modeled astonishingly good regarding the models coarse resolution.

Around Antarctica the model's ice cover has a strong annual cycle. In winter the continent is surrounded by a closed ice cover, while in summer, there are only a few small ice covered areas left. The model's ice extent reaches values of $16.2 \cdot 10^6\,km^2$ in winter (JJA) and $5.87 \cdot 10^6\,km^2$ in summer (DJF). GLOERSEN ET AL. (1992) report $16.0 \cdot 10^6\,km^2$ and $7.0 \cdot 10^6\,km^2$, respectively. The annual cycle in the model reaches its maximum in September and October with $22.9 \cdot 10^6\,km^2$. Caused by the high temperatures and salinities in this area, the spring melting in the model is very intense, leaving almost no ice in late summer and fall ($0.7 \cdot 10^6\,km^2$ in March). Compared to the observed ice covered regions (NSIDC, 1996) in the Weddell Sea and between the Antarctic Peninsula and the Ross Sea, the modeled areas are too small in summer. In winter the ice sheet extends

[b] Ice extent as used here is defined as the area poleward of a line of grid cells with an ice concentration of at least 10%. For the observations the sea ice extent is defined as the area enclosed by the ice edge, which in turn is defined as the 15% concentration contour. Winter is used here for the mean value over the months December to February (DJF) in the northern hemisphere and June to August (JJA) in the South. Summer values span the same months for the other hemisphere, respectively.

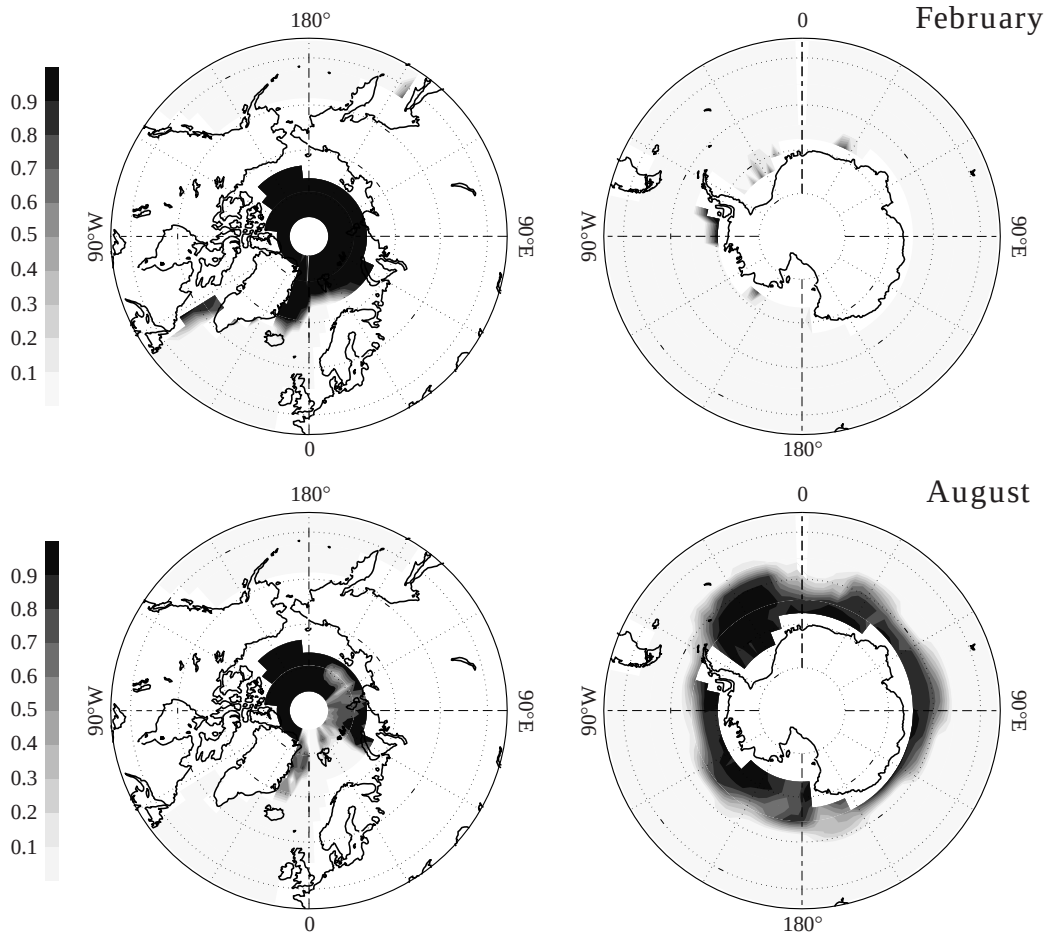

Figure 4.9.: *Mean February (top) and August (bottom) sea ice concentration for the Arctic (left) and Antarctica (right) – integration years 3500 to 3999 of the control run; values of 0 denote ice free conditions, 1 stands for total ice coverage.*

farther to the North than in reality. Especially in the Weddell Sea region and the Indian Ocean sector the modeled ice edge reaches 55°S.

Winter sea ice thickness patterns are given in Fig 4.10. It is obvious from the Arctic plot on the left that the model's thickness distribution is unrealistic. This is due to two reasons: the models resolution is too coarse and the existence of a land mass in the central Arctic hinders a transpolar drift. The sea ice tends to pile up north and northwest of Greenland as the passage between the island and the North Pole is too small to let the ice drift through. This "ice jam" reaches back to the Chukchi Sea. This problem is not unique to this model; it has been reported e.g. by STÖSSEL ET AL. (1998). The ice thickness distribution around Antarctica is within the range of observed values (JEFFRIES, 1998). In the western Weddell Sea along the Antarctic Peninsula they appear to be too low compared to measurements (e.g. STRASS AND FAHRBACH, 1998). This is due to the model's convective activities that are concentrated in the south-western edge of the Weddell Sea.

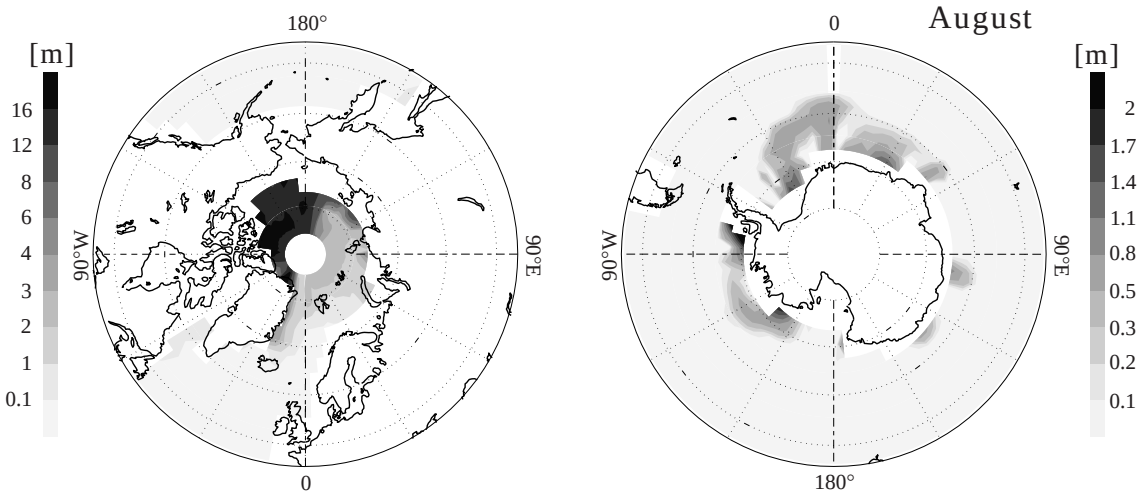

Figure 4.10.: *Mean winter sea ice thickness patterns in m for the Arctic (February – left) and Antarctica (August – right) – integration years 3500 to 3999 of the control run. Note different shading intervals.*

As this study concentrates on the sensitivity of the system to perturbations and to the spreading of signals, an exact match with observational quantities was thought to be of secondary importance. A reproduction of the main circulation systems and water masses, nevertheless, is essential. These requirements are met, as has been demonstrated in this chapter.

5. Sensitivity Experiments

In order to study the capabilities of the used model and its sensitivity to parameterizations some of its settings have been subject to testing. Transport schemes, mixing parameterizations, time steps, filtering, damping time scales and bottom drag have been investigated. These studies have been performed with the uncoupled ocean (runs OC-2 to OC-11) as well as with the coupled model (CTRL and IOC-3 to IOC-6). Table 5.1 lists the parameter settings for all sensitivity runs. For the ocean runs the surface boundary conditions differed from those described in section 3.5 accounting for the simpler needs of the uncoupled model. In detail, the surface forcing fields consisted of annual means and annual and semiannual harmonics. These were obtained from ECMWF (1993) for wind data. SST and SSS forcing fields were prepared from the LEVITUS (1982) climatology. The initial conditions for all runs were those described at the end of chapter 3. Section 5.1 gives a short overview of the modified parameters. The results of the uncoupled ocean runs are presented in section 5.2. Section 5.3 highlights the effects of coupling the sea ice model to the ocean and the model's sensitivity to a change of the restoring time scales.

5.1. Parameter Modifications

The following parameters have been modified in the sensitivity experiments:

Mixing: the traditional approach to parameterize the effects of sub-grid scale processes (mesoscale eddies for instance) in OGCMs is the use of horizontal and vertical mixing schemes for momentum and tracers (K. BRYAN, 1969; F. BRYAN, 1987, and others). In the basic version of the model (denoted by "Const" in Table 5.1) this is done using constant values (independent of space and time) for κ_m in the momentum equations (3.1) and (3.2) as well as for A_m in the horizontal, nonconservative terms (3.3 and 3.4). In the tracer conservation equations (3.5) and (3.6) κ_h and A_h are set constant.

Mixing of tracers by mesoscale eddies is believed to occur mainly along surfaces of constant local potential density. Therefore, a parameterization based on the transformation of the diagonal diffusion tensor was introduced by REDI (1982) and COX

(1987) to account for this kind of mixing ("Isopyc" in Table 5.1). It takes the vertical mixing coefficient κ_h from the basic vertical mixing scheme as a background in the vertical and the A_h from the basic horizontal mixing scheme as a background in the horizontal (PACANOWSKI, 1995). The use of additional, artificial horizontal background diffusion for computational stability can have detrimental effects on the solutions through non-physical diapycnal fluxes especially in regions of steep density slopes (DANABASOGLU AND MCWILLIAMS, 1995).

GENT AND MCWILLIAMS (1990) have developed a different parameterization ("GMcW" in Table 5.1). It is based on a down-gradient diffusion of the thickness between neighboring isopycnals in adiabatic flows. They replace the Eulerian-mean transport velocity of the advection operator by an effective transport velocity (the sum of the Eulerian-mean and an eddy-induced transport velocity). Their formulation can be interpreted as the introduction of an additional tracer advection, in addition to the diffusion of tracers along isopycnals. For a detailed discussion see GENT AND MCWILLIAMS (1990) and GENT ET AL. (1995).

Convection: a parameterization to remove statically unstable stratifications is necessary in models using the hydrostatic approximation. MOM offers implicit and explicit schemes. Static instability is removed implicitly by increasing the vertical diffusivity in regions where the water column is unstable. Explicit convection uses a set of calculations to mix the levels until the stratification is stable. There are various ways how this can be accomplished. Two methods are used here: a scheme developed by COX (1984) mixing two adjacent levels if they are statically unstable. This is done here once for every time step for those experiments marked with "Cox" in Table 5.1. The alternative method (marked "Full") was developed by Rahmstorf (as explained in PACANOWSKI, 1995). It removes static instability mixing the whole water column in one pass, thus avoiding possible problems due to the incomplete mixing in the Cox scheme, that only takes adjacent levels into account.

Tracer advection: the evolution of tracers (as potential temperature and salinity or any passive tracer) in the ocean interior is strongly affected by advection. Therefore it is necessary to represent this process properly. Two techniques are applied here. The central difference algorithm ("CD" in Table 5.1; used in run OC-7) computes the tracer flux across the boundary of two grid boxes centered in space with a leap frog scheme in time. Its advantage is the conservation of the first and second moment (i.e. mean and variance of the tracer)[a]; the disadvantage lies in the numerical dispersion that produces non-physical oscillations (under- and overshoots) of the advected quantity. The flux-corrected transport algorithm ("FCT", see BORIS AND BOOK, 1973; ZALESAK, 1979) computes the flux-difference (the anti-diffusive flux) between a central difference and an upstream scheme; the latter is based on a calculation of one-sided upstream differences in each spatial direction combined with forward time-stepping. The anti-diffusive flux is limited locally so that no under-

[a] Strictly speaking only true for uniform grids (see GERDES ET AL., 1991).

or overshoots can occur. The main disadvantage of the FCT scheme is its time consumption. For a detailed discussion and comparison of advection algorithms see e.g. GERDES ET AL. (1991) or GRIFFIES ET AL. (2000).

Filtering: due to the convergence of meridians on a sphere, the resolution of the model's grid in longitudinal direction decreases towards higher latitudes reaching zero at the poles. This sets a limit for the length of the used time steps ($\Delta\tau$) following the Courant-Friedrichs-Lewy (CFL) criterion

$$\Delta\tau < \frac{\Delta x}{2 \cdot u}$$

with Δx being the width of a grid cell in zonal direction. So, smaller grid boxes require smaller time steps. The instabilities arising when $\Delta x/(2u)$ becomes smaller than $\Delta\tau$ can be removed by filtering the (most unstable) highest wave numbers out of the solution. In MOM this can be achieved by two different methods. The first one (abbreviated "Four" in Table 5.1) does a Fourier smoothing of prognostic variables in the longitudinal direction. Wavenumbers bigger than a latitudinal dependent critical value are eliminated by a discrete Fourier transform. The second method uses multiple passes with a symmetric finite impulse response filter ("Fir"). Both methods are described in PACANOWSKI (1995) and the references therein. As it is reasonable to avoid filtering when possible it was tried to perform runs completely without filtering (run OC-6) and with filtering restricted to velocities and streamfunction ("Ψ" in Table 5.1; runs OC-5, CTRL and IOC runs).

Bottom drag: the bottom drag is represented as a quadratic drag law $\tau_{bot} = c_{dbot}\,\rho_w\,\mathbf{u}_h \cdot |\mathbf{u}_h|$, where τ_{bot} is the bottom drag, c_{dbot} the bottom drag coefficient and $\mathbf{u}_h = (u, v)$ the horizontal velocity at the bottom. Two values for c_{dbot} were used: a "free slip" case with $c_{dbot} = 0$, and $c_{dbot} = 10^3$.

Restoring: in all uncoupled ocean runs (OC), the temperature is restored with a time scale of 30 days for the uppermost level. Surface salinity is restored using a 96 days scale (Δt_{rS}). For testing the sensitivity of the coupled model to SSS restoring, the time scales have been varied for the IOC experiments as stated in Table 5.1.

Topography: the topography used for most of the ocean runs (OC-2 to OC-4 and OC-6 to OC-10) was the original DANABASOGLU AND MCWILLIAMS (1995) topography without the additional "shelf" regions that have been introduced in runs OC-5, CTRL and the IOC runs (see Fig. 3.2 in section 3.2.2).

5.2. Ocean Model Variations

Parameter sensitivity experiments with the uncoupled ocean model have been performed using ten different setups. Basically there have been two classes of experiments: one

Model Run	Mixing	κ_m [m^2/s]	A_m [m^2/s]	κ_h [m^2/s]	A_h [m^2/s]	Convect.	Advect.	c_{dbot}	Filtering	Δt_{rS} [d]	Topog.
OC-2	GMcW	10^{-3}	10^5	0	0	Full	FCT	0	Fir $\pm$57°	96	DMcW
OC-3	Const	10^{-3}	10^5	$5\cdot10^{-5}$	0	Full	FCT	0	Fir $\pm$67°	96	DMcW
OC-4	Const	10^{-3}	10^5	10^{-5}	0	Full	FCT	0	Fir $\pm$67°	96	DMcW
OC-5	Const	10^{-3}	10^6	0	0	Full	FCT	0	Ψ Fir 79.5°N	96	shallow
OC-6	Const	10^{-3}	10^5	10^{-5}	0	Full	FCT	0	—	96	DMcW
OC-7	Isopyc	$2\cdot10^{-3}$	10^6	$5\cdot10^{-5}$	10^3	Cox	CD	10^3	Four $\pm$57°	96	DMcW
OC-8	Isopyc	$2\cdot10^{-3}$	10^6	$5\cdot10^{-5}$	10^3	Cox	FCT	10^3	Four $\pm$57°	96	DMcW
OC-9	Isopyc	$2\cdot10^{-3}$	10^6	$5\cdot10^{-5}$	0	Cox	FCT	10^3	Four $\pm$57°	96	DMcW
OC-10	Isopyc	$2\cdot10^{-3}$	10^6	10^{-5}	0	Cox	FCT	10^3	Four $\pm$57°	96	DMcW
OC-11	Isopyc	$2\cdot10^{-3}$	10^6	10^{-5}	0	Cox	FCT	10^3	Four $\pm$57°	96	shallow
CTRL	Const	10^{-3}	10^6	0	0	Full	FCT	0	Ψ Fir 79.5°N	96	shallow
IOC-3	Const	10^{-3}	10^6	0	0	Full	FCT	0	Ψ Fir 79.5°N	30	shallow
IOC-5	Const	10^{-3}	10^6	0	0	Full	FCT	0	Ψ Fir 79.5°N	180	shallow
IOC-6	Const	10^{-3}	10^6	0	0	Full	FCT	0	Ψ Fir 79.5°N	*NoRI*	shallow

Table 5.1.: *Parameterizations used for ocean sensitivity studies. Abbreviations: Const: horizontal and vertical mixing with constant coefficients; Isopyc: isopycnal mixing with mixing coefficient $A_I = 10^3\,m^2/s$; GMcW: mixing parameterization after* GENT AND MCWILLIAMS *(1990); Cox: convective adjustment after* COX *(1984); Full: convective adjustment using the Rahmstorf scheme; CD: central difference tracer advection scheme; FCT: flux corrected tracer advection scheme; Four: Fourier filtering; Fir: finite impulse response filtering; Ψ: filtering only applied to velocities and streamfunction; NoRI: no restoring under ice, 96 days elsewhere; DMcW: topography after* DANABASOGLU AND MCWILLIAMS *(1995); shallow: topography as explained in section 3.2.2. Further explanations are given in the text.*

where the parameters were chosen comparable to those used by DANABASOGLU AND MCWILLIAMS (1995) – runs OC-7 to OC-11 – and one following MEISSNER (1999) – runs OC-2 to OC-6[b]. Common features for the first class were the usage of isopycnal mixing parameterization with an isopycnal mixing coefficient of $A_I = 10^3\,\mathrm{m}^2/\mathrm{s}$, eddy viscosity coefficients of $\kappa_m = 2 \cdot 10^{-3}\,\mathrm{m}^2/\mathrm{s}$ and $A_m = 10^6\,\mathrm{m}^2/\mathrm{s}$, a bottom drag coefficient $c_{dbot} = 10^3$, convective adjustment after COX (1984) and Fourier filtering poleward from 57°. In the runs OC-2 to OC-6 no bottom drag was applied, the Rahmstorf scheme for convective adjustment was used and a common vertical eddy diffusivity parameter of $\kappa_m = 10^{-3}\,\mathrm{m}^2/\mathrm{s}$. The other parameters and values were varied according to Table 5.1.

The sensitivity runs were performed for a range of 2500 to 3400 model years each. Not all of them reached an equilibrium state by then. For the purpose of identifying whether the models yielded realistic circulation patterns and values, however, the integration times were sufficient. This is demonstrated for example in Table 5.2, in which mean values for characteristic quantities as Drake Passage throughflow and the maxima and minima of the overturning rates in the Atlantic for different centuries of the model runs are given. For instance the differences of these quantities between centuries 17 and 23 of all runs show only minor adjustments. Hence, the quantities reached after shorter run times can be well used for an evaluation of a model run's suitability.

	ACC [Sv]			NADW [Sv]			AABW [Sv]		
Century	17	23	33	17	23	33	17	23	33
OC-2	101.2	101.3	—	7.5	7.6	—	0.82	0.84	—
OC-3	368.1	367.3	—	N / A	27.6	—	N / A	5.36	—
OC-4	293.8	300.5	—	N / A	27.0	—	N / A	4.34	—
OC-5	187.9	190.6	194.6	16.9	17.1	17.5	1.14	1.03	0.96
OC-6	273.5	291.0	306.1	N / A	N / A	25.8	N / A	N / A	4.21
OC-7	189.2	193.6	196.2	N / A	N / A	23.1	N / A	N / A	2.93
OC-8	192.3	197.8	200.8	23.0	23.2	23.4	3.82	4.17	4.32
OC-9†	216.4	N / A	223.1	21.2	N / A	22.6	3.34	N / A	3.48
OC-10†	175.6	174.4	169.2	15.7	15.9	15.9	1.15	1.28	1.29
OC-11†	193.2	197.4	197.7	18.3	19.3	19.9	1.70	1.49	1.41

Table 5.2.: *Characteristic values of ocean sensitivity runs averaged over one century. ACC: Drake Passage Throughflow; NADW: maximum of the streamfunction for the zonally integrated volume transport below 500 m in the North Atlantic; AABW: amount of the minimum of the streamfunction below 3000 m depth in the North Atlantic. †: values in the "33" columns are from the 30th century. N/A: values not available due to technical reasons; —: values not available due to length of run.*

[b] The runs OC-1 and IOC-1 were unstable and are not subject of investigations presented in this study; the numbering has been kept, though.

Mixing Variations

Variations of the mixing scheme showed that the parameterization after GENT AND MCWILLIAMS (1990) in run OC-2 was extremely time consuming; it needed about 60% more time per grid point and time step than the comparable OC-3 run. This was the reason why this mixing scheme was not used for further investigations. Besides that, the Drake Passage throughflow with 101 Sv and the Atlantic meridional overturning cell (MOC, i.e. the streamfunction for the zonally integrated meridional volume transport) with 7.5 Sv were too weak in the chosen setup. On the other hand, OC-3 produced an ACC which was far to strong; values for the Drake Passage throughflow of more than 360 Sv are beyond any acceptable limit.

To study the models variability with respect to vertical eddy diffusivity parameterizations in OC-4 $\kappa_h = 10^{-5}\,\mathrm{m}^2/\mathrm{s}$ was applied instead of OC-3's $\kappa_h = 5 \cdot 10^{-5}\,\mathrm{m}^2/\mathrm{s}$. A second pair of experiments with these diffusivities is OC-9 ($\kappa_h = 5 \cdot 10^{-5}\,\mathrm{m}^2/\mathrm{s}$) and OC-10 ($\kappa_h = 10^{-5}\,\mathrm{m}^2/\mathrm{s}$). First of all, the mass transport through the Drake Passage is reduced for the runs with smaller diffusivities – it is decreased in both cases by about 20%. The thermocline and the halocline in the subtropics become shallower and the contours of intermediate water are slightly more pronounced for the runs with smaller diffusivities. As an example Fig. 5.1 shows meridional salinity sections across the Atlantic along 30°W for OC-3, OC-9 (upper) and OC-4, OC-10 (middle panel) together with a climatological section. The strong front in the deep South Atlantic in runs OC-3 and OC-4 is remarkable. A less pronounced structure can be seen in OC-9. The salinity structure of OC-10 is very close to the climatology. Globally averaged potential temperature and salinity profiles that are displayed in Fig. 5.2 for OC-9 and OC-10 show substantial differences: clearly visible in the left panel is the deep and diffusive thermocline of run OC-9 (large κ_h - dashed black line). The thermocline structure is clearly improved in OC-10 (solid grey line). The salinity profile in the right plot of Fig. 5.2 shows much fresher water below 1 km depth for run OC-9 than for OC-10. However, the salinity minimum at 1 km depth is clearly too low in both cases. The runs with decreased vertical diffusivity show reduced meridional density gradients at depth which in turn give rise to the reduced water mass transport in the ACC[c]. At the same time the North Atlantic overturning and the AABW cell in the Atlantic are weakened (compare Table 5.2). The decrease in the MOC from OC-3 to OC-4, though, is far less than predicted by the 1/3 power law of BRYAN (1987), which would require a reduction to about 60% in the strength of the NADW for a diffusivity coefficient reduction to 20% of its prior value. For the OC-9 to OC-10 case BRYANS relation approximately holds. The overall structure of the MOC is not affected (compare Fig. 5.7, lower panel and 5.8, upper panel).

[c] This argument follows BOROWSKI ET AL. (2001), who investigated the effects of thermohaline and wind forcing on the large scale steady state transport of a circumpolar channel with blocked geostrophic contours. They find that the Circumpolar Current is to leading order determined by the density field. The direct effect of wind stress and the effects of friction and non-linearity have been found to be of minor importance (compare also GNANADESIKAN AND HALLBERG, 2000).

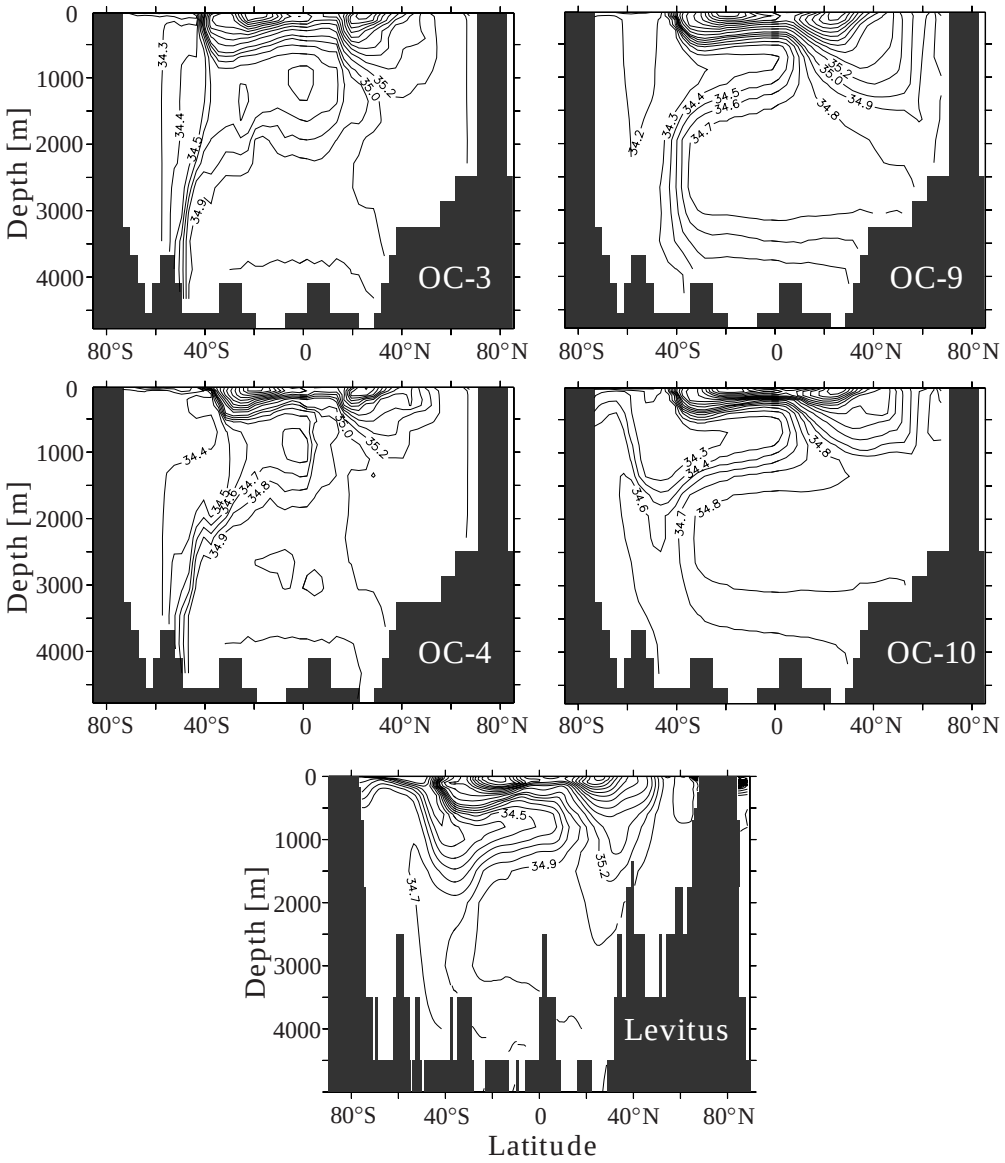

Figure 5.1.: *Salinity sections across the Atlantic Ocean along 30°W for runs OC-3 (top left) and OC-4 (middle left) – mean values for 23rd century of integration and runs OC-9 (top right) and OC-10 (middle right) – mean values for 30th century of integration; the bottom panel shows data from a climatology by* LEVITUS *(1982). Contour interval is 0.2 psu; between 34 and 35 psu it is set to 0.1 psu.*

The total kinetic energy per unit volume[d] for runs OC-9 and OC-10 is displayed in

[d] The total kinetic energy per unit volume E_{kin} is calculated from the discretized form of the integral

$$E_{kin} = \frac{\rho_0}{2}\frac{1}{V}\iiint_{z\,y\,x}(u^2+v^2)\,dx\,dy\,dz$$

with V denoting the total ocean volume.

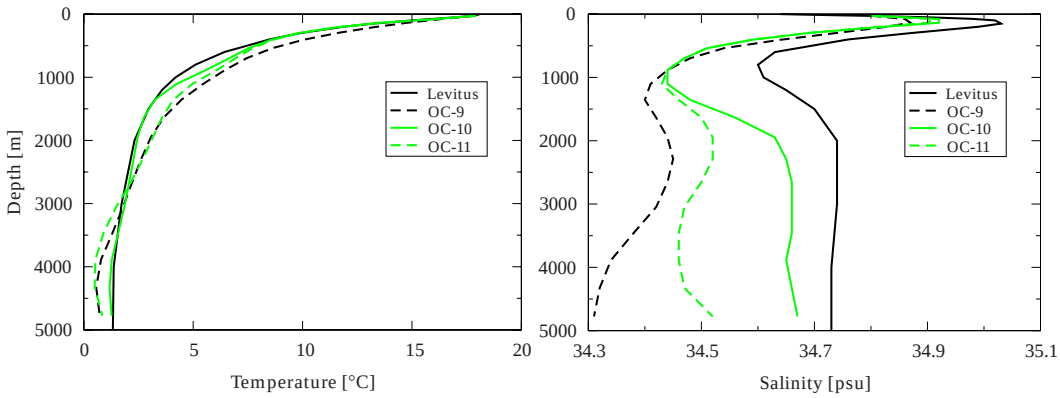

Figure 5.2.: *Globally averaged profiles of potential temperature (left) and salinity (right panel) for runs OC-9 (dashed black), OC-10 (solid grey) and OC-11 (dashed grey) - mean values for 30th century of integration. The solid black lines represent values from a climatology by* LEVITUS *(1982).*

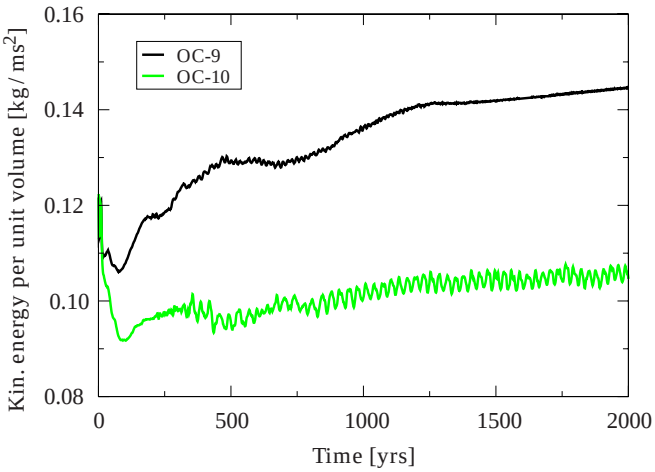

Figure 5.3.: *Total kinetic energy (January values) of runs OC-9 (black line) and OC-10 (grey line).*

Fig. 5.3. The values for OC-10 are lower than for OC-9. This is consistent with the weaker ACC. At the same time OC-10 (the grey line) shows a multidecadal oscillation between two states that is far more distinct than for the run OC-9 with the higher κ_h.

The effect of the horizontal background eddy diffusivity is investigated comparing runs OC-8 ($A_h = 10^3\,\mathrm{m}^2/\mathrm{s}$) and OC-9 ($A_h = 0$). It should be noted, however, that the advection scheme (FCT) provides a certain amount of implicit horizontal diffusion that can be quite significant in areas of high velocities (GRIFFIES ET AL., 2000). The mass transport through Drake Passage is reduced with increased diffusivity (compare Table 5.2). This result is consistent with the studies by MEEHL ET AL. (1982) and DANABASOGLU AND MCWILLIAMS (1995). As explained earlier for the κ_h variations, the reduction can be attributed to the decrease of the meridional density contrast. The strength of the Atlantic overturning cell is not affected significantly, although its shape differs to a minor

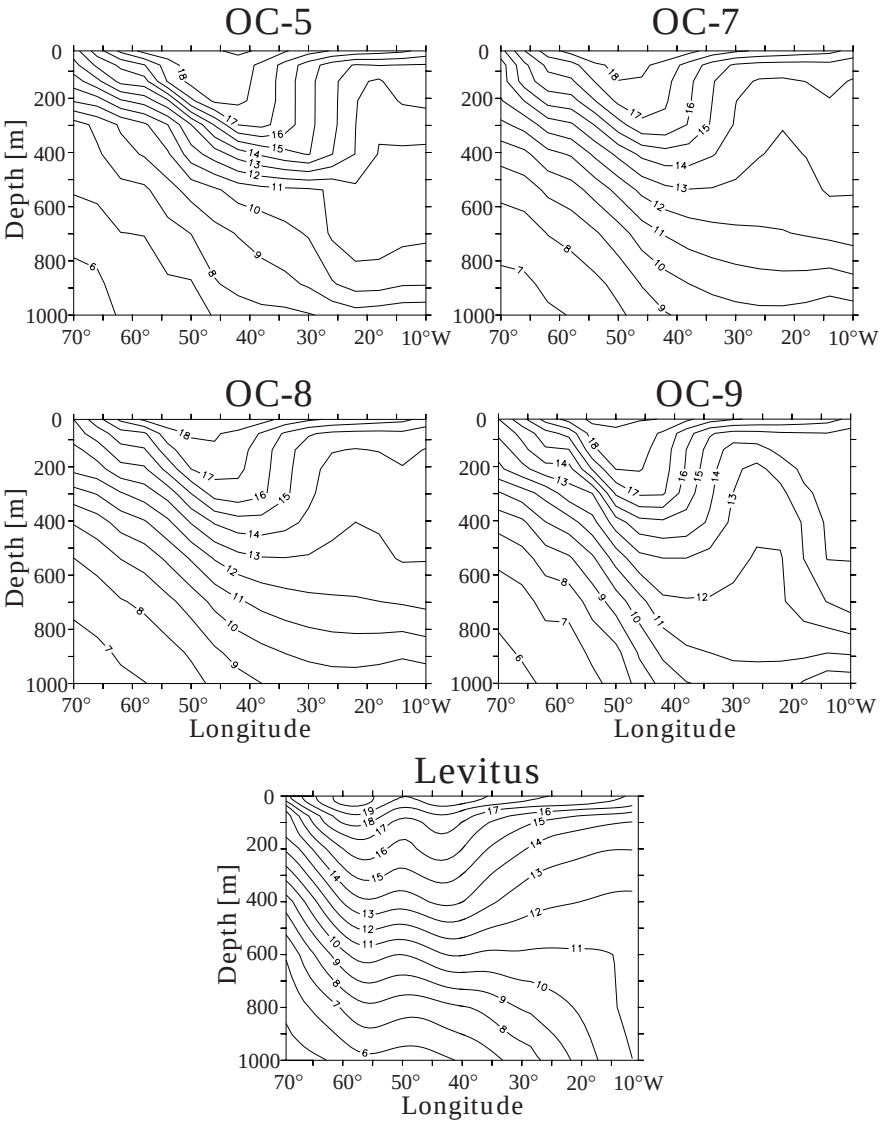

Figure 5.4.: *Zonal temperature section through the Atlantic basin at 40°N, upper 1000 m for runs OC-5 (upper left), OC-7 (upper right), OC-8 (middle left), OC-9 (middle right) - mean values for 30th century of integration - and data from a climatology by (*LEVITUS*, 1982, lower panel). Contour interval is 1°C.*

extent (middle and lower panel of Fig. 5.7 on page 59). Without background diffusivity the MOC cell reaches deeper and the sinking region at 70°N is more confined, whereas in run OC-8 the counter-rotating cell north of it is stronger. One important effect of horizontal background diffusivity is that the horizontal temperature and salinity fields are smoothed out. When comparing the zonal temperature sections across the subtropical gyre in the Atlantic basin at 40°N (Fig. 5.4), the case with background diffusivity (middle left) shows a broadening of the warm core of the Gulf Stream compared to run OC-9 (middle right). In general the slopes of the isothermals are diminished in OC-8.

The eddy viscosity parameters have not been varied systematically in this study. So here some reasoning is given for the values chosen for the control run. Critical regions for horizontal mixing are regions of sharp velocity gradients like the western boundary currents. There, A_m must be big enough that the expression $A_m \nabla^2 v_\lambda$ has the same order of magnitude than βv with $\beta = f \cot\phi / a$. MEISSNER (1999) found in her experiments with the same ocean model that a small value for A_m ($10^5\,\mathrm{m}^2/\mathrm{s}$) has the advantage that the model could do without filtering, but led to an unrealistic circulation with deep water production too far north and a MOC with its maximum north of the Greenland-Scotland-Ridge. This problem did not appear with an increased eddy viscosity of $10^6\,\mathrm{m}^2/\mathrm{s}$. Here, the erroneous position of the MOC maximum was not reproduced with low mixing coefficients, but the combination of higher A_m and a filtering restricted to velocities and the streamfunction seemed reasonable to use with this setup (see also upcoming paragraph on filtering).

BRYAN (1987) stated that the large scale circulation is influenced only to a minor extent by the vertical eddy diffusivity coefficient κ_m. Here, as a constraint on κ_m, the Ekman depth should lie within the top level of the model grid. This was surely the case for $\kappa_m = 10^{-3}\,\mathrm{m}^2/\mathrm{s}$, the value used in the control run.

Advection Schemes

The FCT advection scheme promises a better representation of fronts, or more general, regions of sharp gradients. This effect is (at least partly) obliterated when the diffusivity coefficients are not set to 0. Therefore it is not surprising that the results of runs OC-7 and OC-8 are almost identical. Although they differ in the advection scheme for the tracers (central difference vs. FCT), they have high diffusion coefficients of $\kappa_h = 5 \cdot 10^{-5}\,\mathrm{m}^2/\mathrm{s}$ and $A_h = 10^3\,\mathrm{m}^2/\mathrm{s}$, so that the diffusion eliminates the effect of the different advection schemes. A comparison of the temperature sections of Fig. 5.4 (upper right and middle left) as well as of the MOCs (Fig. 5.7 – upper and middle) show no discernible differences. The effect of FCT can be seen more clearly by looking at the temperature sections of runs OC-9 (middle right) and OC-5 (upper left) in Fig. 5.4. In both cases, the horizontal diffusivity A_h is zero; the gradients east of the Gulf Stream are much sharper than for OC-8 (middle left). The frontal zones to be found in meridional sections show similar results.

Filtering

As explained in section 5.1 filtering the highest wave numbers allows to run models with reasonable time steps. On the other hand, there are disadvantages arising. Especially in regions with small-scale topographic features as narrow straits problems can result from the truncation of Fourier series. This can lead to unrealistic, non-physical values for the temperature and salinity fields. For example temperatures thus falling below the freezing

point of sea water are not compatible with the equation of state. This can lead to unrealistic phase transitions and violates the model's energy balance. An overestimation of the ice production in coupled models can result from this deficiency as has been reported by MEISSNER (1999).

In this study runs OC-4 and OC-6 differ only with respect to filtering. In the former tracers, velocities, and the streamfunction are filtered with a finite impulse response filter on both hemispheres poleward from 67°. The latter used no filtering at all. Fig. 5.5 shows the difference between the zonally averaged mean temperature fields. There is a pronounced anomaly north of the Greenland-Scotland-Ridge extending to the abyssal layers. A weaker anomaly can be seen in the southern hemisphere close to Antarctica.

The problem of the convergence of the meridians is especially important for the velocity fields in higher latitudes. There, the high propagation speed of barotropic waves sets the limit for the time step. To account for the need to filter those and to avoid the problem of non-physical tracer values, filtering in the control run is restricted to velocities and the streamfunction. The results showed that the model thus can run stably producing realistic results.

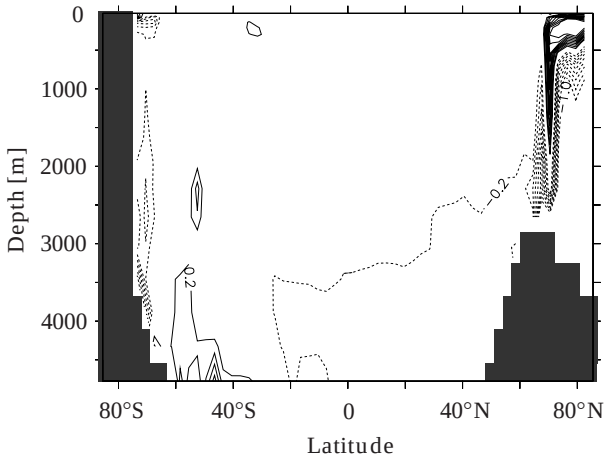

Figure 5.5.: *Difference of zonal averaged global potential temperatures between runs OC-4 and OC-6 for 23rd century of integration. Contour interval is 0.1°C, only values smaller than -0.2°C or bigger than 0.2°C are shown; solid lines denote positive, dashed ones negative values.*

Topographic Effects

Models show substantial sensitivity to changes in their topography (REDLER AND BÖNING, 1997; MEISSNER, 1999, and many others). To facilitate comparisons with published model results, the investigations were started with the bottom topography used by DANABASOGLU AND MCWILLIAMS (1995). It was known from previous experience (MEISSNER, 1999) that the very smooth and deep topography could lead, under certain

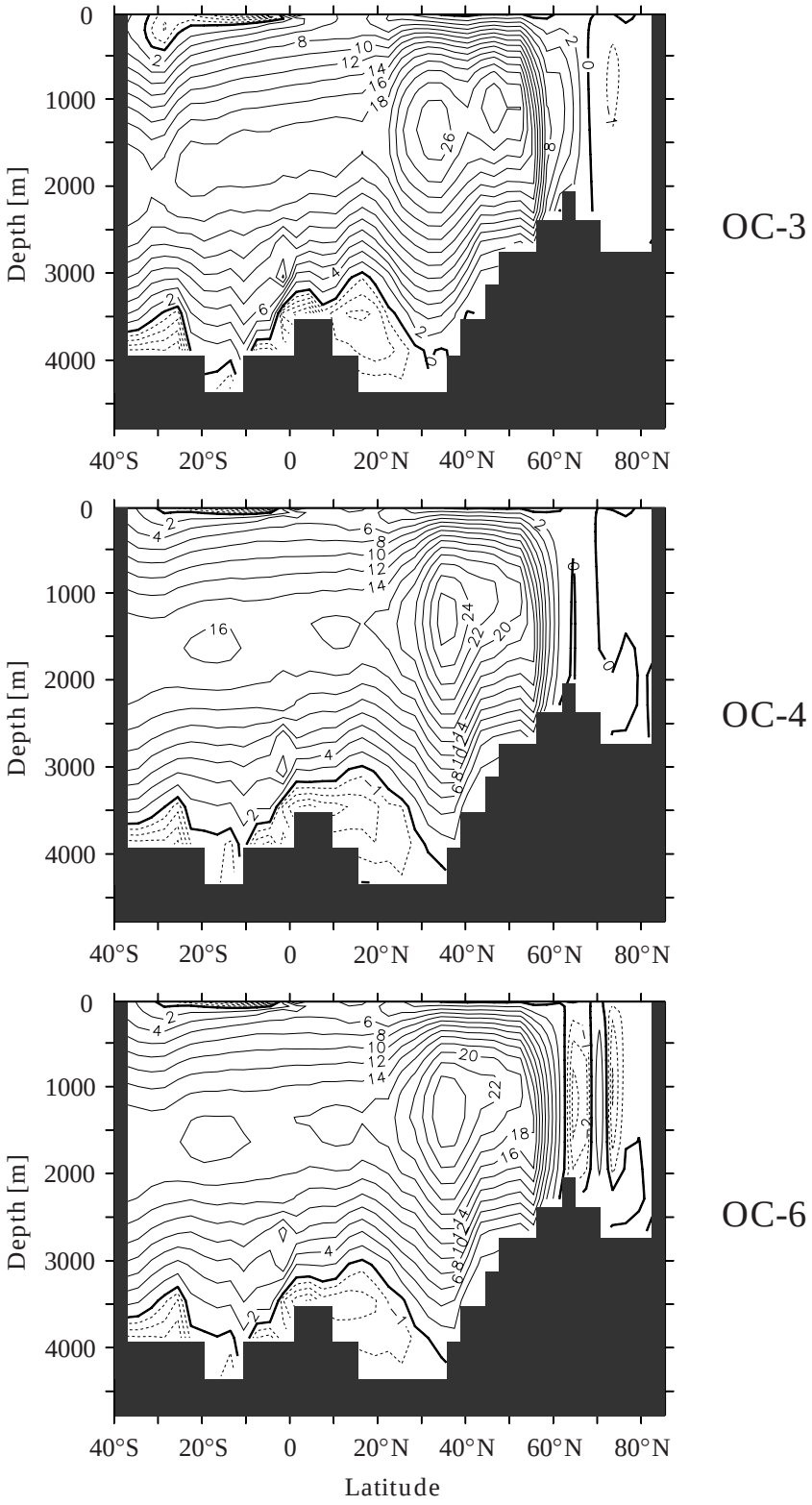

Figure 5.6.: *Mean meridional overturning streamfunction for the Atlantic in Sv – integration year 2300 to 2399 for runs OC-3 (upper), OC-4 (middle), year 3300 to 3399 for OC-6 (lower panel). Contour interval is 2 Sv for positive (solid lines), 1 Sv for negative values (dashed lines).*

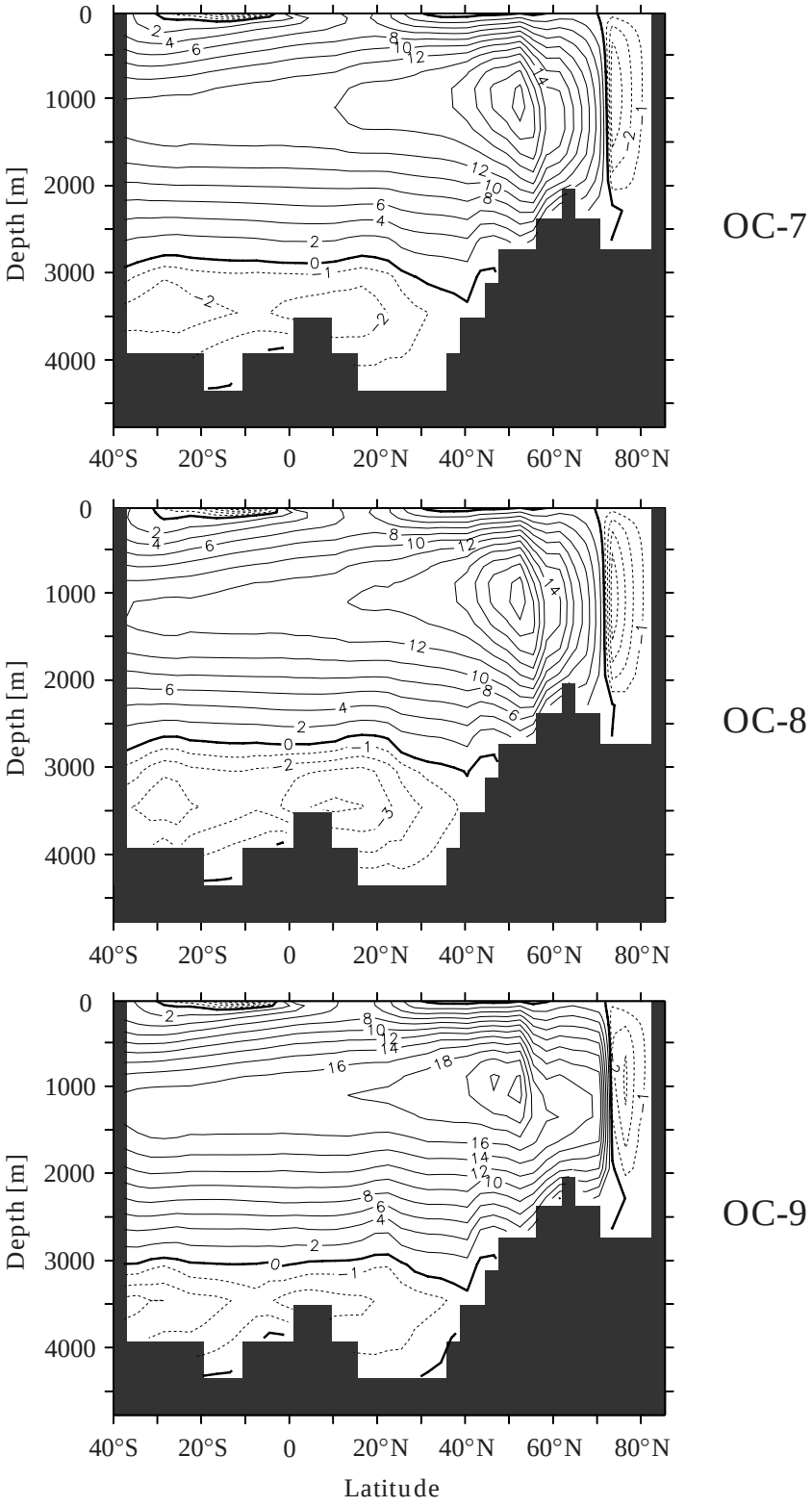

Figure 5.7.: *Mean meridional overturning streamfunction for the Atlantic in Sv – integration year 3000 to 3099 for runs OC-7 (upper), OC-8 (middle), OC-9 (lower panel). Contour interval is 2 Sv for positive (solid lines), 1 Sv for negative values (dashed lines).*

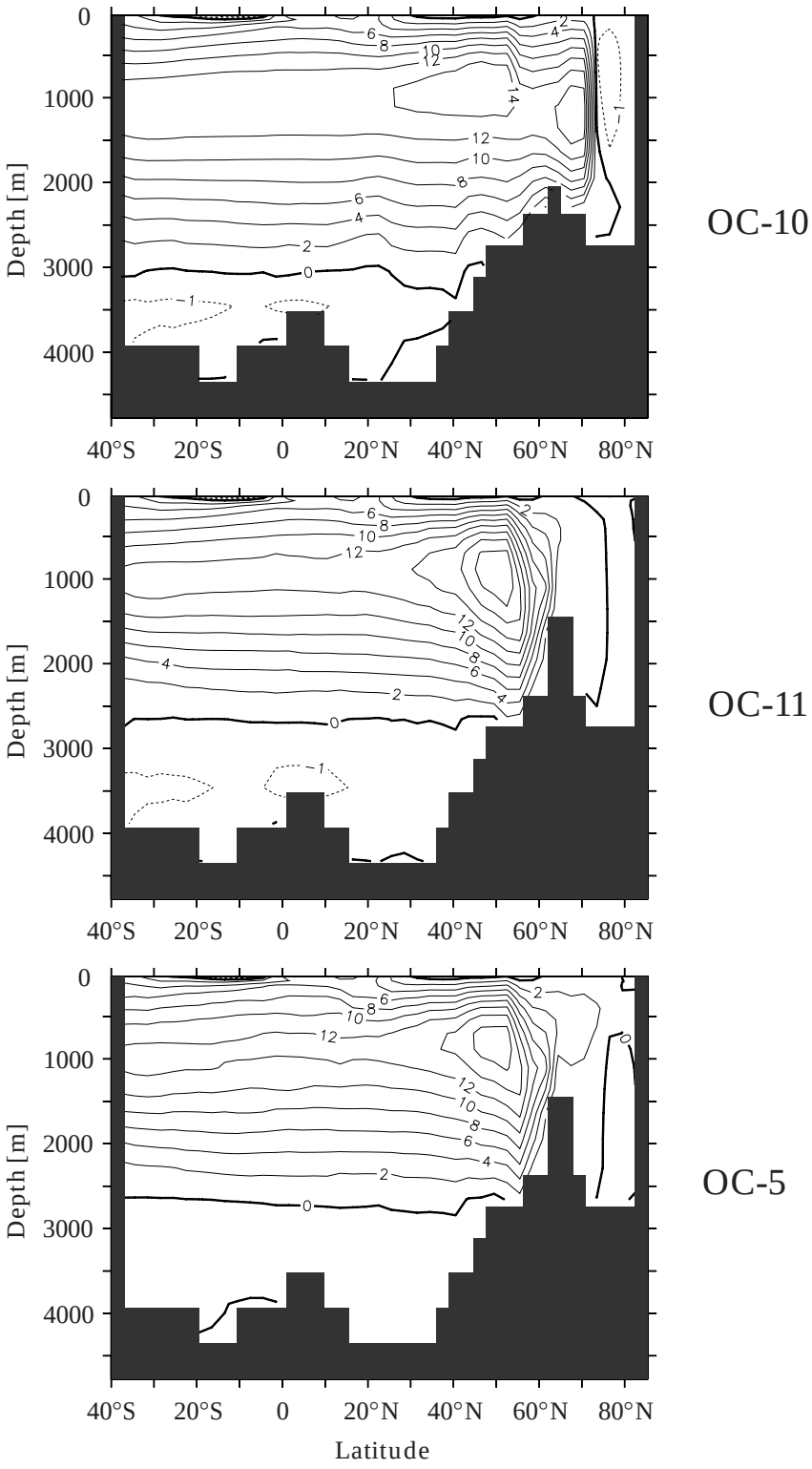

Figure 5.8.: *Mean meridional overturning streamfunction for the Atlantic in Sv – integration year 3000 to 3099 for runs OC-10 (upper), OC-11 (middle), OC-5 (lower panel). Contour interval is 2 Sv for positive (solid lines), 1 Sv for negative values (dashed lines).*

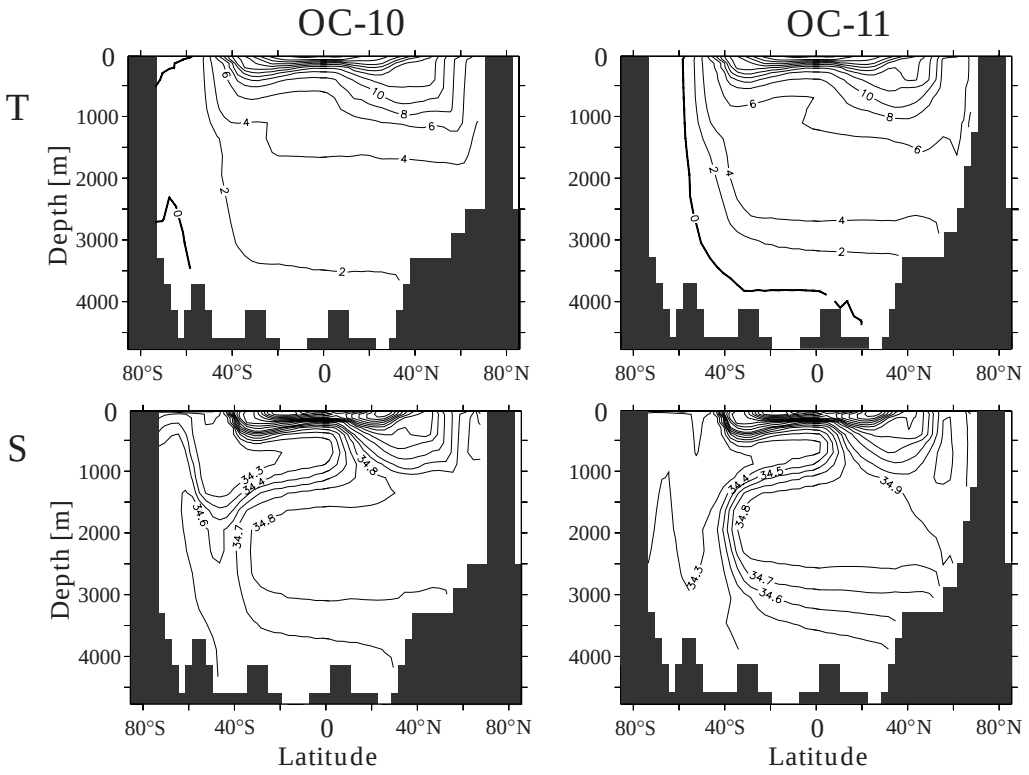

Figure 5.9.: *Potential temperature (upper panel) and salinity sections (lower panel) across the Atlantic Ocean along 30°W for run OC-10 (left) and OC-11 (right) – mean values for 30th century of integration. Contour interval is 2°C for temperature, 0.2 psu for salinity, between 34 and 35 psu it is 0.1 psu.*

circumstances, to a relocation of the northern deep water production sites into the Arctic. The effect of the introduction of a Barents Sea shelf and a higher Greenland-Scotland-Ridge as described in section 3.2.2 is investigated here. Run OC-10 uses the original topography after DANABASOGLU AND MCWILLIAMS (1995), OC-11 the modified version with additional shallow regions. Changes in the topography of the northern North Atlantic alter the global ocean circulation dramatically. With the shallow topography present the Drake Passage throughflow is stronger by about 15% (200 Sv compared to 170 Sv with the original topography; see Table 5.2). The maximum of the Atlantic meridional overturning streamfunction increases from 16 to 20 Sv. The cell is shallower and the sinking region shifts southwards from 70°N to 55°N, i.e. south of the Greenland-Scotland-Ridge (upper and middle plot of Fig. 5.8). This must be regarded as more realistic. While dense water is formed north of the ridge, the bulk of the deep water in the North Atlantic is formed by entrainment of ambient waters in the overflows of the Greenland-Scotland-Ridge. Sinking of more than 10 Sv in the Nordic Seas, on the other hand, is not observed. The deep streamfunction minimum (representing the AABW) increases slightly. A changed structure of the global temperature and salinity fields (Fig. 5.2) is associated with changes in the MOC. The temperature structure of run OC-11 (dashed grey

line) is characterized by weaker gradients. The salinity in the upper kilometer remains unchanged, in deeper levels it is lowered by approximately 0.2 psu. Meridional temperature and salinity sections across the Atlantic along 30°W (Fig. 5.9) reflect the broader thermocline as well as a warming of the intermediate depths for OC-11. The 4° isotherm is shifted from 1600 m (OC-10) to 2600 m (OC-11). In the abyssal ocean the temperatures become colder, the 0° isotherm expands to 20°N, while the entire Atlantic deep ocean becomes significantly fresher. At intermediate depths there is a pronounced difference between the hemispheres. While in the North Atlantic there is only a slight salinity increase close to the Greenland-Scotland-Ridge, a fresh tongue with values smaller than 34.3 psu reaches down to 3 km in the Southern Ocean. Thus, in run OC-11 the NADW is warmer and therefore less dense, while the associated overturning cell has become shallower. This allows the AABW to penetrate underneath despite its relatively low density. These changes in temperature and salinity produce a strong density gradient in the model's deep levels. This is the reason for the increased strength of the ACC in the run with shallow topography. These mechanisms will be investigated further in section 7.1.

In addition to the effects discussed so far, the new topography in OC-11 made it necessary to reduce the time step for numerical reasons. While a time step of 2400 s for the internal and external mode velocity was sufficient for run OC-10 to be numerically stable, for run OC-11 a time step of only 1728 s led to a stable integration. For run OC-5, in which the same topography was used but a different mixing scheme and a different filtering region, the time step even had to be decreased to 864 s for the external mode velocities.

5.3. The Coupled Model

Coupling the ocean to the ice model has the effect of changing surface boundary conditions from the ocean's "point of view". Therefore, the equilibrium state of the ocean is different from that of the uncoupled ocean case. Table 5.3 lists values for the characteristic quantities that have already been used in the previous section for the uncoupled sensitivity runs. Run OC-5 is the uncoupled "version" of the control run described in chapter 4. It showed a reasonable behavior with respect to all applied criteria taking the coarse resolution of the model into account. The MOC (Fig. 5.8, lower panel) has a maximum of 17.5 Sv with the center of the cell located at 900 m depth at 52.5°N. Meridional sections through the Atlantic along 30°W (Fig. 5.10, upper graphs) show a well defined thermocline and a clear intermediate water signal. In depths between 1000 m and 3000 m the Atlantic is slightly too warm and salty; in greater depths it is a bit too cold and fresh. The maximum of the AABW cell is too weak, while the strength of the ACC is overestimated. In summary, the main features of the Atlantic and global ocean circulation are reproduced quite well. The control run (CTRL) is identical to OC-5 except for the changed forcing fields and the existence of the ice model. The values for the Drake Passage throughflow and the strength of the NADW and AABW cells are increased in the coupled runs. A com-

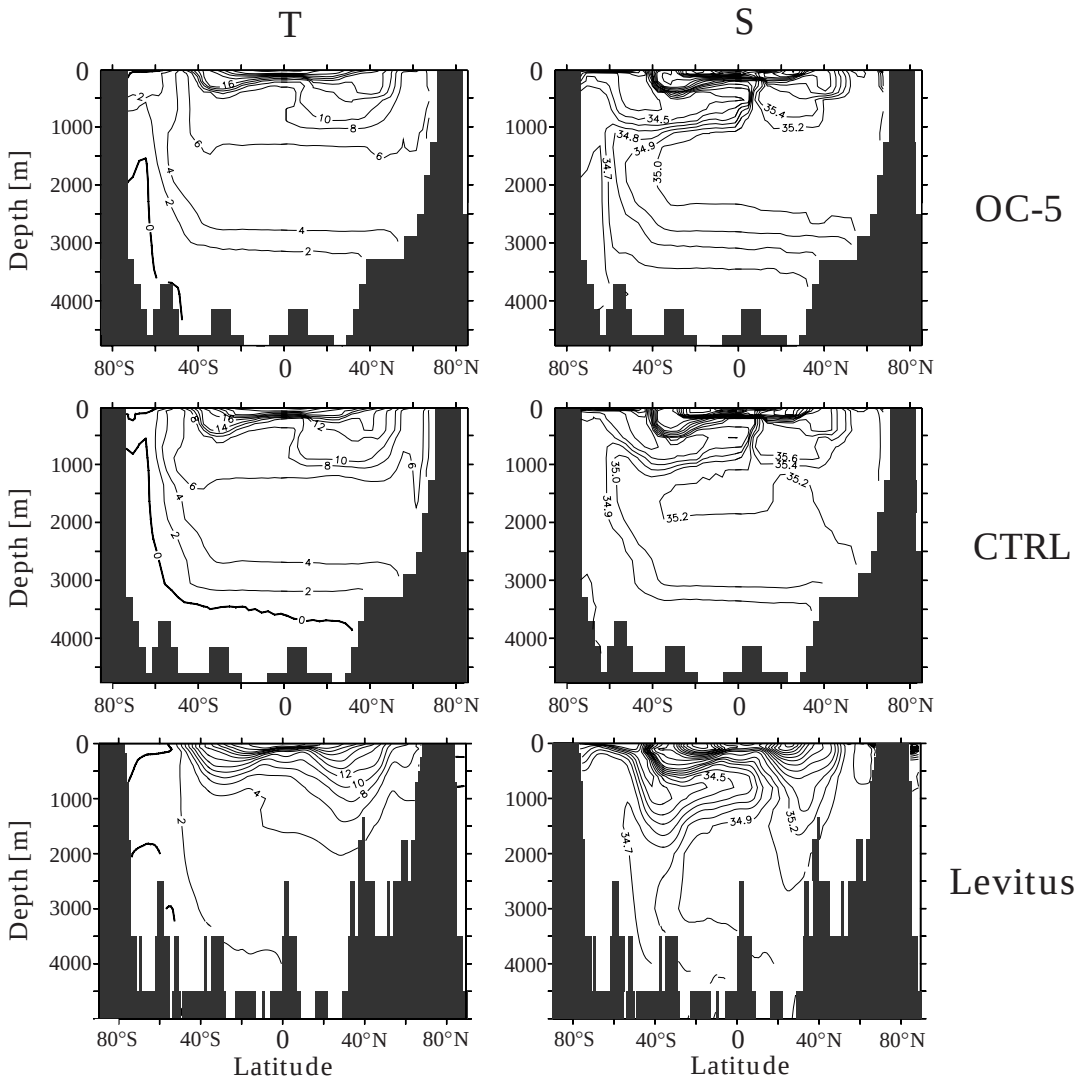

Figure 5.10.: *Potential temperature (left) and salinity sections (right) across the Atlantic Ocean along 30°W for run OC-5 (top), CTRL (middle) – mean values for 30th century of integration – and data from a climatology by* LEVITUS *(1982) (bottom). Contour interval is 2°C for temperature, 0.2 psu for salinity, between 34 and 35 psu it is 0.1 psu.*

parison of Fig. 5.8, lower panel, and Fig. 4.5 reveals that the structure of the MOC has not been altered - only its strength has increased from 18 Sv to almost 25 Sv by adding the ice model.

In Fig. 5.10 the 30°W-sections across the Atlantic are compared for OC-5 (top) and CTRL (middle). The temperature structures are very similar for the biggest part of the basin. The main differences are found along the Antarctic continental margin and over the whole section below 4000 m depth, where the CTRL-temperatures lie below 0°C. The salinity changes are more drastic. Almost the entire basin has become saltier, especially in the abyssal layers the values are increased by more than 0.2 psu.

	Δt_{rS} [d]	ACC [Sv]			NADW [Sv]			AABW [Sv]		
Century		23	33	49	23	33	49	23	33	49
OC-5	96	190.6	194.6	194.6	17.1	17.5	18.0	1.03	0.96	1.35
CTRL	96	236.6	235.2	236.6	24.9	24.6	24.9	1.65	1.61	1.50
IOC-3	30	236.5	235.5	235.1	25.0	24.8	25.3	1.68	1.62	1.71
IOC-5	180	236.1	235.1	236.4	24.9	24.8	25.2	1.72	1.60	1.50
IOC-6	—	270.0	265.6	266.1	22.6	22.3	21.1	2.15	1.99	1.54

Table 5.3.: *Restoring time scales and centennial means for characteristic values of coupled sensitivity runs and the ocean reference run OC-5. ACC: Drake Passage Throughflow; NADW: maximum of the streamfunction for the zonally integrated volume transport below 500 m in the North Atlantic; AABW: amount of the minimum of the streamfunction below 3000 m depth in the North Atlantic.*

Fresh water fluxes at the surface influence the ocean circulation to a great extent. Restoring boundary conditions therefore play an important role in controlling the model runs. The models sensitivity to changes in the restoring time scale for salinity Δt_{rS} has been investigated with runs CTRL, IOC-3 and IOC-5. The values for Δt_{rS} are listed in Table 5.3. Examining the characteristic values contained in this table reveals immediately that for a Δt_{rS} range from 30 to 180 days there are no detectable differences between the runs (besides a slight increase of the strength of the AABW cell in IOC-3). A comparison of streamfunction, velocity and tracers revealed only minor differences, too (not shown).

In run IOC-6 restoring was completely switched off for ice covered regions. Elsewhere it was set to 96 days – the value of run CTRL. The system reacted with a weaker and shallower overturning cell (compare Figs. 5.11 and 4.5). The globally averaged salinity (temperature) is increased (decreased) over the entire water column with deviations growing with depth (Fig. 5.12); the values deviate stronger from the LEVITUS (1982) climatology than those for the control run. The total ice volume increased by almost 20% in the Arctic Ocean and by more than 30% in the Southern Ocean. However, the net effect is stronger in the northern hemisphere due to the much larger mean ice volume there. Most of the volume increase can be attributed to the increase of ice thickness, the ice covered area remained almost unchanged. The stronger stratification induced by the temperature and salinity changes that are most intense in the northern hemisphere lead to an increased meridional density gradient at depth in the southern hemisphere, thereby causing a more intense ACC: the Drake Passage throughflow increases from 236 Sv to 266 Sv. So, omitting restoring under ice degrades all considered model quantities.

As long as a – even weak – salinity restoring is maintained, the model is insensitive to the restoring time scale. Nevertheless, restoring, even under sea ice, is necessary to constrain the model within reasonable limits.

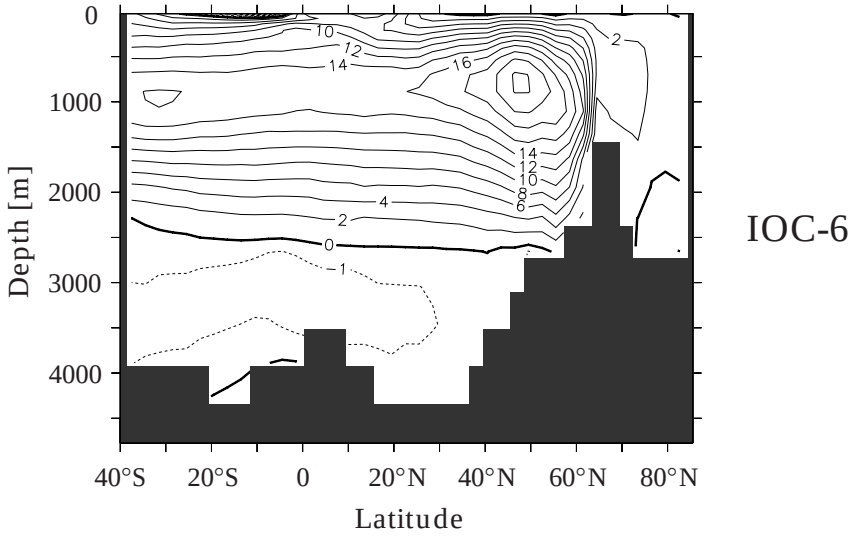

Figure 5.11.: *Mean meridional overturning streamfunction for the Atlantic in Sv – integration year 3300 to 3399 of run IOC-6. Contour interval is 2 Sv for positive, 1 Sv for negative values.*

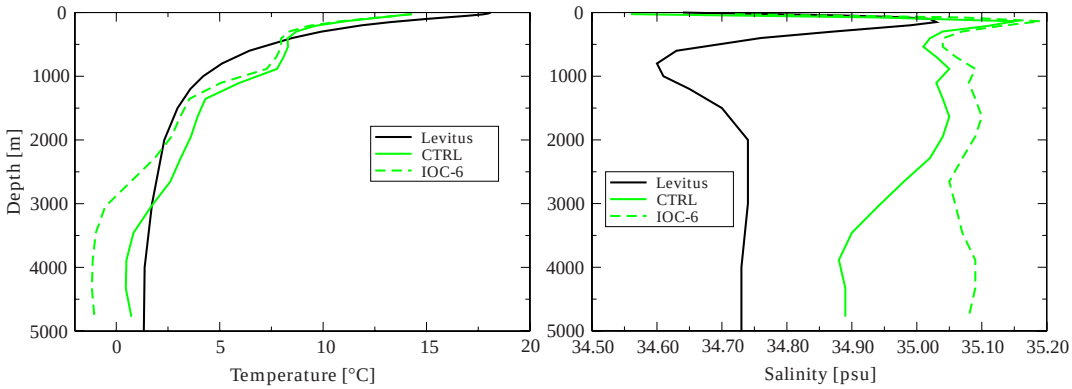

Figure 5.12.: *Globally averaged profiles of potential temperature (left) and salinity (right panel) for runs CTRL (solid grey), and IOC-6 (dashed grey) – mean values for 49th century of integration. The solid black lines represent values from a climatology by* LEVITUS *(1982).*

6. Interhemispheric Signal Transmission and Internal Variability

How does the ocean transmit information over long distances? There are two important processes to be named: advection and waves. The transmission is bound to distinct pathways: the ocean's margins can serve as wave guides for Kelvin waves and topographic waves; equatorial Kelvin and Rossby waves follow the 0° parallel; internal Kelvin waves travel along boundaries set up by the ocean's stratification. Advective signal propagation is effected by water mass transport in the ocean currents. Signals can be sent out into the interior of the ocean basins by Rossby waves from these pathways. Another means of spreading the advected information is eddy mixing. In order to examine the nature of these processes in the ocean, two approaches are used here. In this chapter the system's inherent variability will be investigated by applying statistical methods. In chapter 7, its sensitivity to variations of boundary conditions is studied.

In recent years much effort has been put into the attempt to identify teleconnection patterns, i.e. linkages over great distance of seemingly disconnected anomalies (GLANTZ, 1991). Prominent examples for this kind of patterns are the ENSO (El Niño / Southern Oscillation) phenomenon and the NAO (North Atlantic Oscillation). These long distance interactions can be described as irregular, but roughly cyclic, low-frequency climate variations (MANN AND PARK, 1999). The investigation of climate fluctuations in this frequency range is undertaken to separate a possible anthropogenic climate change from natural climate variability and to assess the potential predictability of climate anomalies several years in advance (JUNG, 2000).

The complexity of interactions – in the climate system as well as in the model used here – and the enormous amount of output data produced by the latter make it necessary to introduce statistical techniques to be able to differentiate between signals on different time scales. Moreover, advanced statistical methods, as used frequently in modern geosciences, open the possibility to reveal mechanisms and processes that are hidden from a direct approach. The statistical techniques used in this work are explained in appendix A.

As it has already been stressed the largest amount of energy in the world ocean is associated with the water mass transport in the ACC. Furthermore, the Southern Ocean is connected directly to all other ocean basins. Hence, it seems reasonable to start looking

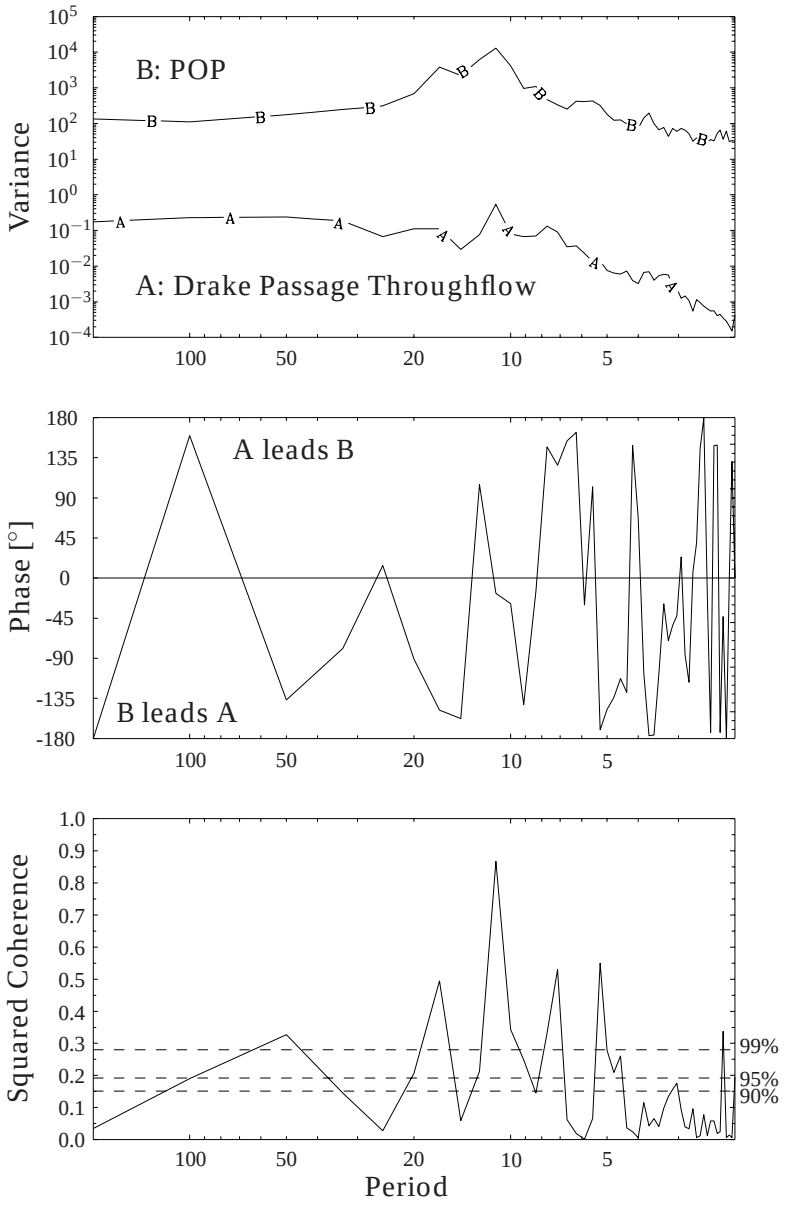

Figure 6.1.: *Spectral analysis of the Drake Passage throughflow (A) and the imaginary part of the first POP of the depth of the 27.5 isopycnal (B) for integration years 3500 to 5000 of the control run; variance density spectrum (top), phase spectrum of the cross correlation (middle) and square of coherence of the density spectra (bottom).*

for interdecadal signals there. In the top panel of Fig. 6.1[a] the curve marked with an "A" shows the result of a spectral (Fourier) analysis of the Drake Passage throughflow (which is, as all of the upcoming results, retrieved from the model output for the control run). A clear maximum can be identified at a period of 11 to 12 years.

[a]The other panels of this figure will be used and explained later in the text.

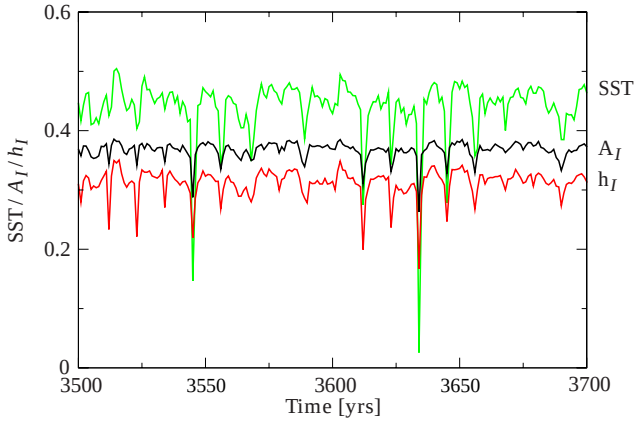

Figure 6.2.: *Time series of annual means of SST, sea ice concentration (A_I) and thickness (h_I) in the Weddell Sea (55° to 15°W and from 55°S to the Antarctic continent) for integration years 3500 to 3700 of the control run; SSTs in °C are multiplied with −1; unit for ice thickness is m; ice concentration is given in its dimension-less form.*

Following the idea of a possible influence of the ACC onto the deep water production in the southern hemisphere (which will be explained in more detail in section 7.3), the logical next step is to look for the prominent frequencies of the Drake Passage throughflow in other quantities in the Southern Ocean. Fig. 6.2 gives the time series of annual means for SST, ice concentration, and ice thickness averaged over the deep water production area in the Weddell Sea region (taken from 55° to 15°W and from 55°S to the Antarctic continent). The SST has been multiplied by −1, that is negative peaks indicate high temperatures. The SST as well as the sea ice concentration and thickness show a very regular behavior with negative peaks every 11 years. The ice concentration and thickness minima in the annual means of Fig. 6.2 result from minima in the three winter months of July to September; the spring, summer and fall values compare to those of all other years (not shown). To investigate the nature of the anomalies in those years with extrema, composites have been calculated for the mean of the winter months July to September of all years showing ice thicknesses in the Weddell Sea smaller by one standard deviation compared to their 500 years mean. These composites are compared to those of the winter months of all years following directly after the "peak" years. Fig. 6.3 shows the difference in SST, SSS (top panels), sea ice concentration, heat flux (middle) and convection depth[b] (bottom) between the composites for winters with extrema and their successors. The positive SST anomalies are located in the region of the ACC north of 64°S with maxima of more than 2°C located in the north-eastern part of the graph. The SSS is raised over almost the entire area reaching values of up to 0.3 psu. In the Weddell Sea the surface waters of the "peak" winters remain almost unchanged. Ice concentration anomalies are negative in the ACC region representing a decreased ice extension. Again the Weddell Sea shows only very weak signs of variability. There are intense negative heat flux anomalies east of

[b]The depth at which the density is 0.01 kg / m^3 larger than its respective surface value is taken as a measure for the depth of convection here.

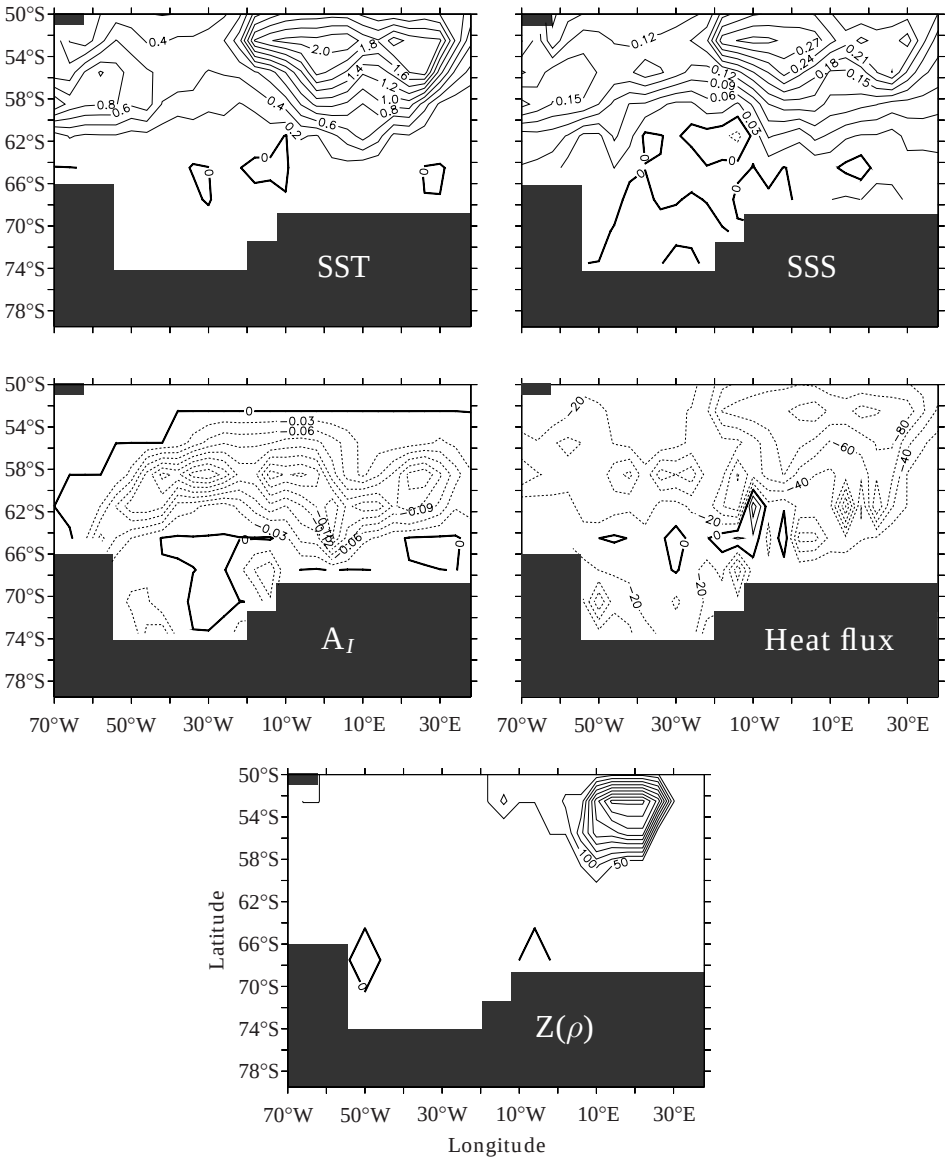

Figure 6.3.: *SST (top left), SSS (top right), sea ice concentration (A_I, middle left), heat flux (middle right) and depth of density 0.01 kg/m^3 larger than its respective surface value (z, bottom) in the Weddell Sea and adjacent regions; differences between the composites of winter means (July to September) of years with strong anomalies and those of their following years; positive heat flux is defined into the ocean; contour intervals are 0.2°C, 0.03 psu, 0.03, 20 W/m^2 and 50 m, respectively; solid lines denote positive, dashed ones negative values.*

the 0° meridian at about 62°S, representing a stronger ocean heat loss at these positions in "peak" years. Further north where the maxima of the SST and SSS anomalies are located the ocean heat loss has maxima of more than 100 W / m^2 and shows a convection depth of about 500 m (which also is the absolute value of the convection depth as this region is stably stratified in "regular" years).

An explanation for the features detected from these composites could be the following: in "peak" years the surface temperatures and salinities are increased north of about 62°S. The positive SST anomalies in the ACC region force the ice cover to become thinner and retreat. The large ice-free areas lead to an intensified heat loss of the ocean to the cold overlying atmosphere. At the same time the increased salinities weaken the stratification of the ocean. In the region east of Greenwich Meridian and north of about 60°S this effect compensates the buoyancy gain due to higher temperatures, thus leading to convective activities there. Despite reaching down only half a kilometer this convection could possibly trigger a signal that can be traced to other regions of the ocean.

A method to detect the principal modes of a quantity's variability is the Empirical Orthogonal Function analysis (EOF, also known as Principal Component Analysis – see appendix A.1). Here, this technique was used to investigate annual mean data for the years 3500 to 4000 of the control run. The first EOF of the barotropic mass transport streamfunction (explaining 23% of the variance of the global field – not shown) revealed maxima in the Ross Sea and in the region detected by the analysis of the composites of Fig. 6.3. To follow a possible path of theses anomalies into deeper layers a Canonical Correlation Analysis (CCA – see appendix A.2) has been performed between the barotropic mass transport streamfunction and the potential temperature in the model's 17th level (approximately 3500 m depth). This linear technique helps to identify patterns of time series of two multivariate data sets with maximum correlation. The CCAs are ordered according to their correlations. The patterns of the first CCA do not show signals in Atlantic sector of the Southern Ocean. The second CCA between the horizontal streamfunction and the 17th level's temperature is displayed in Fig. 6.4. The correlation between the time series is 0.94. The spectra of both series are peaked at a period of about 11 years and are coherent at a significance level of more than 99% for that frequency. The pattern of the streamfunction explains 13.8% of the variance of the global field, that of the temperature 6.5%. The temperature shows a clear signal in the Atlantic sector of the Southern Ocean. This implies that a link of the kind hypothesized before between surface anomalies and the deep ocean could exist.

Presuming that information about the anomalies in the deep ocean propagates into the Atlantic one possible route would be that of the AABW; other candidates could be paths following the continental slopes (e.g. reversing the pathway of the Deep Western Boundary Current). In following the track of AABW, the time series (upper right panel of Fig. 6.4) of the second CCA of the potential temperature of the 17th layer is regressed onto the streamfunction for the zonally integrated mass transport in the Atlantic Ocean (performing a lagged regression analysis as described in A.3). This technique is applied here to examine the spreading of signals with the time characteristic of the 17th layer's temperature anomaly. The results for the regression without lag and a lag of four years are displayed in Fig. 6.5. The regressions show a clear signal spreading northward in the intermediate and lower model levels. To test the significance of the correlation (displayed in Fig. 6.6 for the 4 year-lag) an auto-regressive process of first order AR(1) was applied to the original time series $\alpha(t)$. Monte-Carlo-experiments have been used to produce

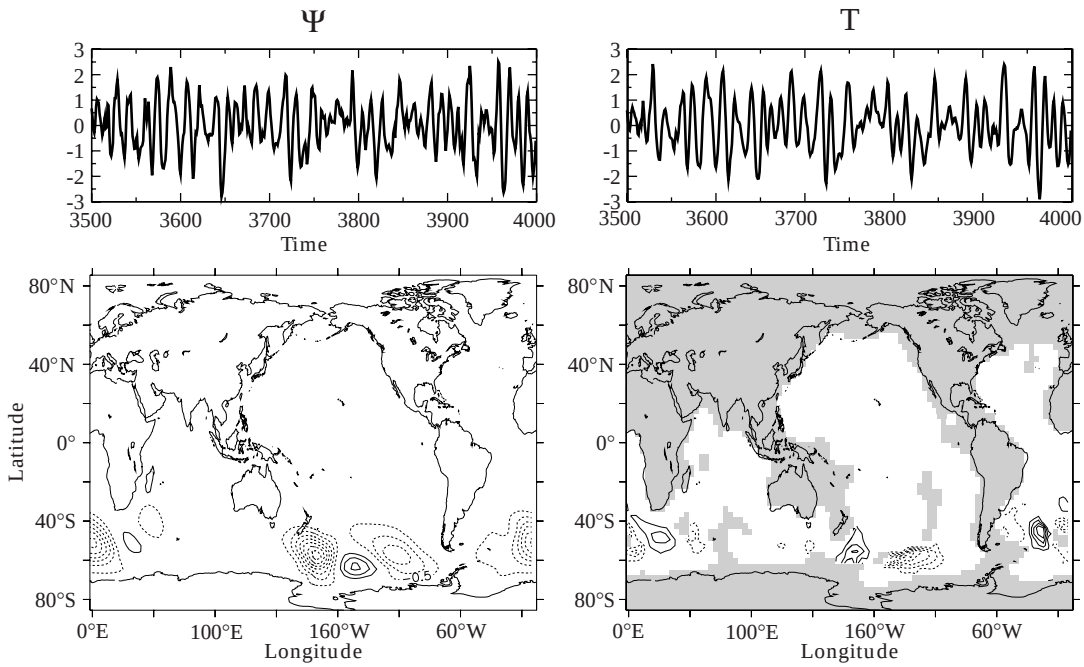

Figure 6.4.: *Second CCA between the barotropic mass transport streamfunction (left side) and the potential temperature in the 17th model layer (3459 m - right); the upper panels show the time series for the years 3500 to 4000, the lower the CCA patterns; contour intervals are 0.5 Sv and 0.02°C, respectively; the grey shading shows the topography of the 17th level; the correlation between the time series is 0.94, the explained variance for the streamfunction is 13.8% , for the potential temperature 6.5%.*

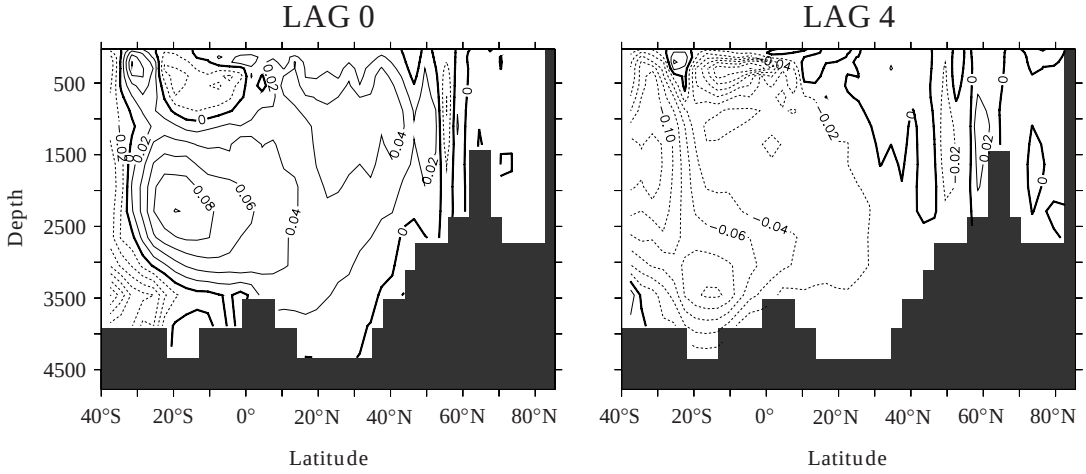

Figure 6.5.: *Regression between the time series of the second CCA of the potential temperature of the 17th model layer and the streamfunction for the zonally integrated transport in the Atlantic Ocean; the left panel shows the regression pattern without lag, the right the regression pattern with a lag of 4 years; contour interval is 0.02 Sv.*

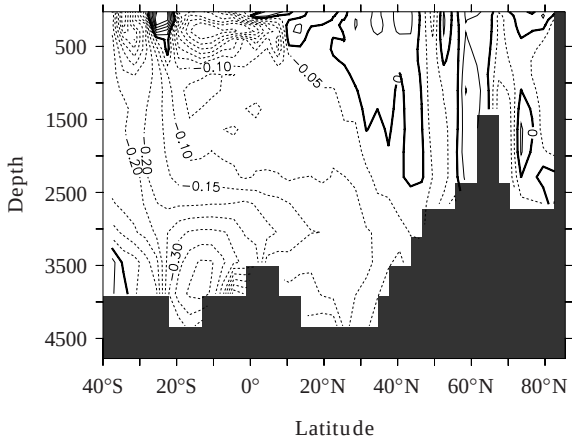

Figure 6.6.: *Correlation coefficient for the 4 years lagged regression of Fig. 6.5; contour interval is 0.05 Sv.*

random time series with the same auto-correlation as $\alpha(t)$. Then, the correlations with $\alpha(t)$ were calculated. The result shows that correlations larger than 0.13 are significant on a 90% level, those larger than 0.19 on a 99% level. The result of the regression analysis can therefore be regarded as statistically robust. However, the vertically integrated mass transport streamfunction is zonally averaged for the Atlantic basin. Therefore it is not possible to detect detailed pathways for the spreading of signals from this quantity.

Meridional wave propagation predominantly occurs bound to topographic features and internal boundaries (trapped Kelvin waves for instance, compare PEDLOSKY, 1987). If this class of signal transmission was involved here, wave-like structures are likely to be found over the continental slopes of the South American continent. To concentrate on the time scale determined before, the model data were treated with a highpass filter keeping periods between 2 and 20 years. Potential temperature anomalies were calculated for a section of the 17th model level along the Deep Western Boundary Current region, as indicated by the grey line in Fig. 6.7. Fig. 6.8 displays a Hovmöller diagram of the southern part of this section for the model years 3900 to 3950. There is a clearly recognizable propagation from South to North with a period of about 10 to 12 years. The propagation is not uniform, though. Between 30° and 35°S there is a shift indicating the appearance of a different mode of signal propagation. The signals intensify north of this shift and then become weaker when approaching the equator. North of it no corresponding signature is found. The described signals are not of advective nature as a comparison with the long time annual mean of the velocities in this level (Fig. 6.7) reveals; over the entire section the average velocities are southward.

Principal Oscillation Pattern (POP) analysis is a method to diagnose and investigate the space-time variability of a complex system (for details see appendix A.4). This method allows to follow the temporal evolution of a quantity (i.e. propagating signals in this investigation) on a distinct frequency band. Reconstructed POPs give a time series of this quantity reduced to variability patterns belonging to these distinct frequencies. Wave

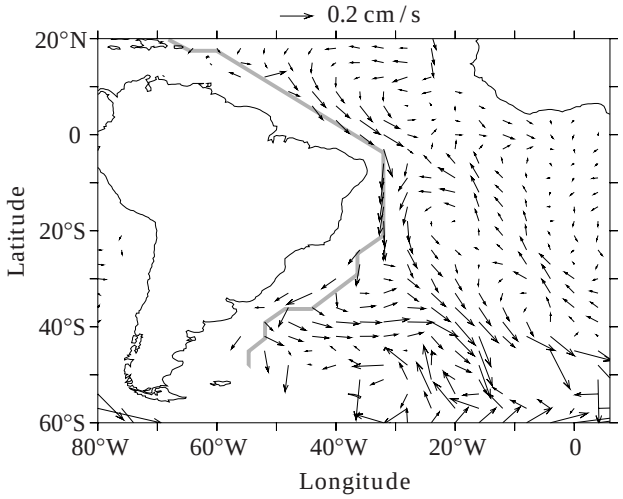

Figure 6.7.: *Velocities in the 17th level - i.e. 3459 m depth - for the Southern Atlantic and the Atlantic part of the Southern Ocean; annual mean for the integration year 3500 to 3999 of the control run. The length of the reference arrow equals 0.2 cm/s; the grey line denotes the section along the continental slope as referenced in the text.*

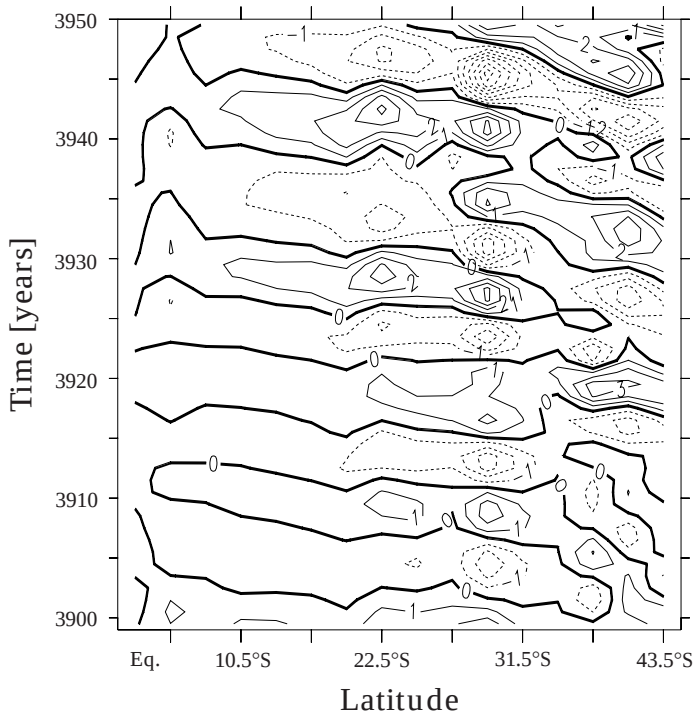

Figure 6.8.: *Hovmöller plot of a section of potential temperature anomalies in the 17th layer along the Deep Western Boundary Current as indicated by the grey line in Fig. 6.7 for the model years 3900 to 3950; units are in 0.01°C; solid lines denote positive, dashed ones negative values.*

propagation in the deep ocean is known to be associated with the displacement of density surfaces. Therefore, the depths of isopycnals and their anomalies were studied here. The temperature of a distinct level appeared not to be an appropriate quantity for this investigation as density surfaces may vary with depth. A number of different isopycnals were investigated with respect to their suitability for detecting propagating anomalies. It turned out that the 27.5 isopycnal (located at depths between 900 and 1200 m between 40°N and 40°S) showed the strongest signal. The POP analysis was applied to the unfiltered data. A cross spectral analysis of the time series of the second CCA of the 17th level potential temperature with the imaginary part of the first POP has been performed to test the connection of the investigated quantities. Fig. 6.9 (top) shows the variance density spectra. Both quantities have a clearly marked peak at about 11 years. The two time series show a strong coherence that is significant at more than 99% at this period (Fig. 6.9, lower panel). They are in phase as can be seen from the phase spectrum of the cross correlation (middle).

Figs. 6.10 and 6.11 show a series of the reconstructed first POP for the 27.5 isopycnal of the Atlantic Ocean for 12 model years (in yearly steps). This first mode represents 17.6% of the total variance of the anomalies in the isopycnal's depth. In the southernmost part of the graphs there are alternating positive (red) and negative (blue) anomalies that propagate eastward. After reaching the southern tip of Africa the anomalies split into two parts, one continuing eastward into the Indian Ocean, the other moving north and into the South Atlantic basin (see the positive anomaly of years one to three or the negative for years six to nine). At the same time there is a direct northward path along the South American coastline. For example the small negative anomaly of the second year at the southern end of the graph at 40°W expands to the north-west in year 3 and merges with the negative anomaly north of it at about 30°S in year 4. This combination of two northbound propagating signals at this latitude may serve as an explanation for the "shift" observed at the same position in the potential temperature section of Fig. 6.8. Further north at the equator the anomalies arriving from the south split into two parts. The positive anomaly that fills the central South Atlantic Ocean in year 4 is cut off over the next three years in the equatorial region. In year 7 two separate small positive anomalies can be seen in this area. The western anomaly stays approximately at its position while the eastern one moves towards the African coast. On reaching the continental margin it expands and covers the entire West African equatorial region in years 10 and 11. In year 12 it has enlarged further, merging with the positive anomaly advancing from the south along the southern African coastline. At the same time it has expanded to the north along the eastern boundary of the ocean and fills the interior of the North Atlantic basins with an anomaly of the same sign. This kind of expansion can be seen more clearly in the negative anomaly developing at the eastern margin of the Atlantic Ocean in years 5 to 8. The period of these signals ranges from 9 to 12 years depending on the observed feature. Having the 11 year period of the ACC signal in mind the striking resemblance of the graphs of years 2 and 12 can at least been interpreted as a strong hint that an anomaly with this frequency influences the entire Atlantic basin.

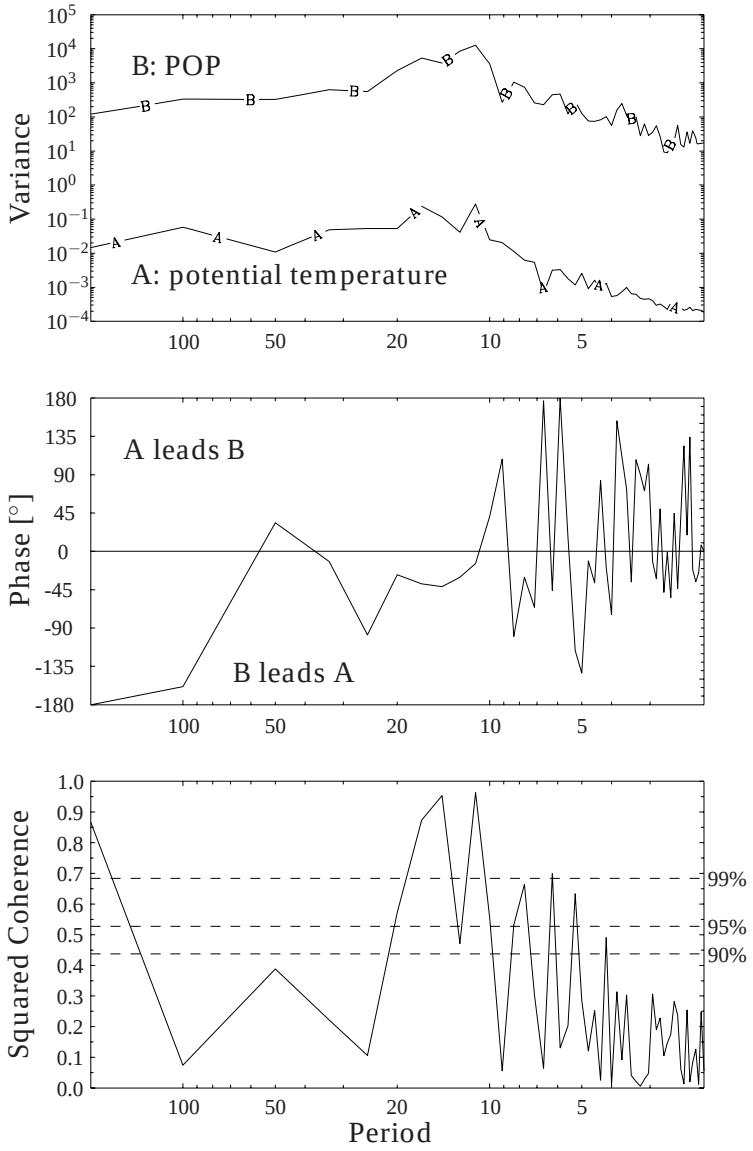

Figure 6.9.: *Spectral analysis of the time series of the second CCA of the potential temperature in the 17th model level (A) and the imaginary part of the first POP of the depth of the 27.5 isopycnal (B) for integration years 3500 to 4000 of the control run; variance density spectrum (top), phase spectrum of the cross correlation (middle) and square of coherence of the density spectra (bottom).*

In order to test the quality of this investigation a cross spectral analysis between the real and the imaginary part of the used first POP has been performed. Both quantities have a clearly marked peak in their variance density spectra (Fig. 6.12, top) at approximately 11 years and show a very similar structure. The two time series show a strong coherence that is significant at the 99% confidence level for most of the frequency range (Fig. 6.12, lower panel). The imaginary part leads the real part by 90° as can be seen from

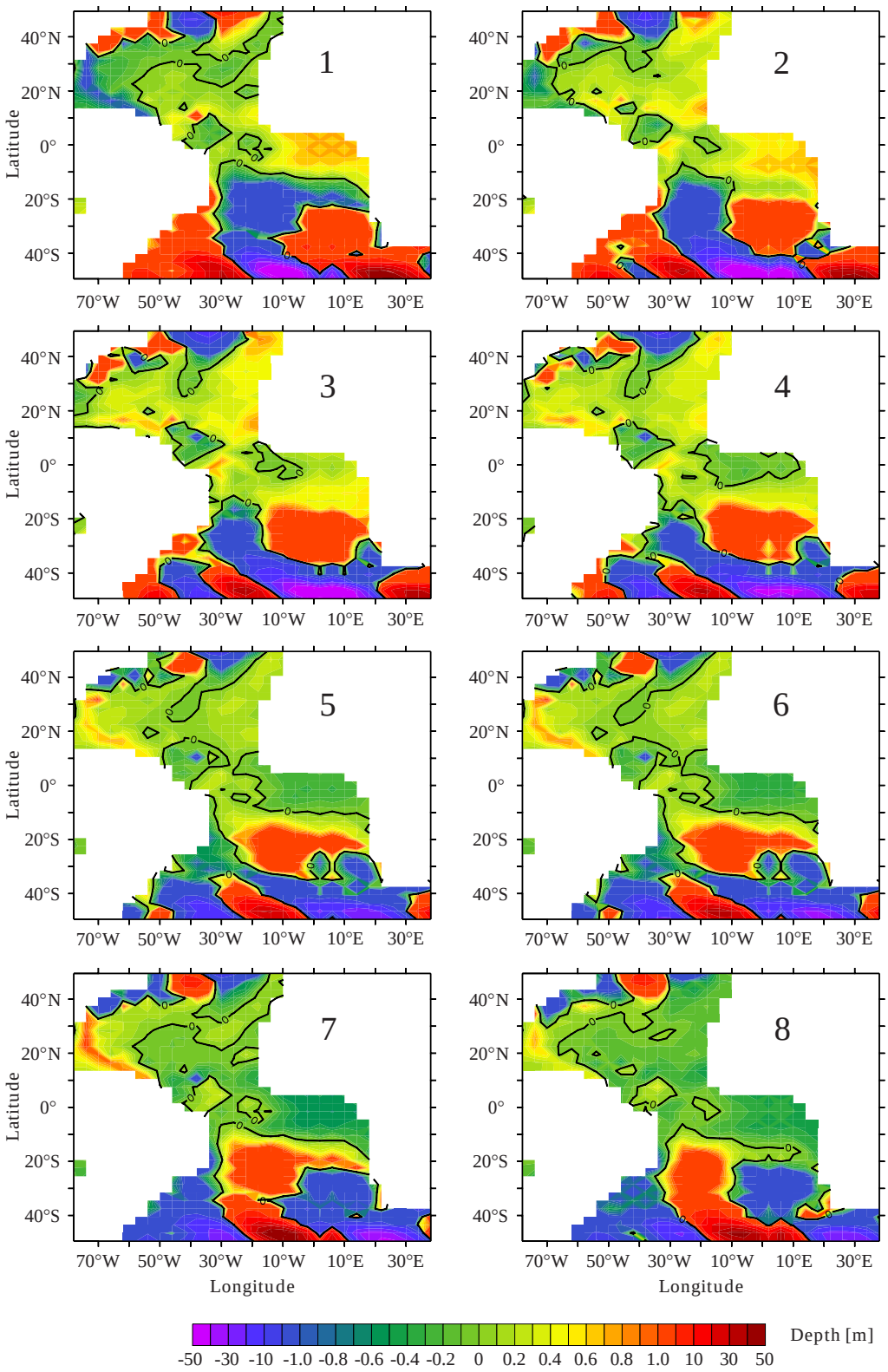

Figure 6.10.: *Reconstructed time series from the first POP for anomalies of the depth of the 27.5 isopycnal in the Atlantic Ocean in m; this mode represents 17.6% of the total variance. The years (1 to 8) are counted from model year 3536.*

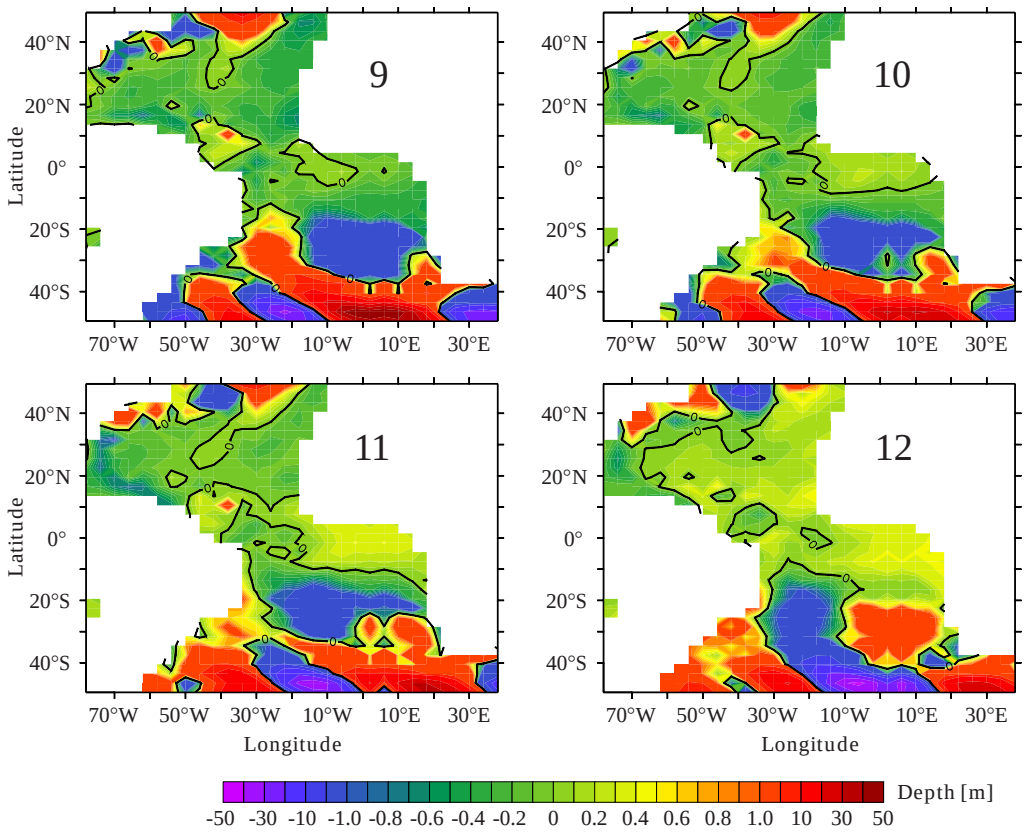

Figure 6.11.: *As in Fig.6.10 for years 9 to 12.*

the phase spectrum of the cross correlation (middle). This characteristic is in accordance with the requirements for a successful POP analysis (VON STORCH AND ZWIERS, 1998, chapter 15). Another cross spectral analysis between the Drake Passage throughflow and the imaginary part of the POP is shown in Fig. 6.1. The variance density spectrum of the Drake Passage throughflow ("A" in the upper panel) shows its maximum at the same period as the POP series ("B"). The phase spectrum reveals that both quantities are in phase at this frequency. The correlation between the two is coherent at a very high significance level.

Part of the described signal transmission can be attributed to propagating Kelvin and Rossby waves. A signal is propagating eastwards along the path of the ACC[c]. At the exit of the Drake Passage the ACC turns to the north before bending back to the east. At this point Kelvin waves are triggered that move northward along the continental slope of South America. Before the ACC enters the Indian Ocean another signal is send out that propagates into the central South Atlantic with the characteristics of a long Rossby wave.

[c]It may be speculated that a Rossby wave could be involved here. The phase speed of Rossby waves is always directed to the west (PEDLOSKY, 1987), while their group velocity can be directed eastward traveling with the main flow. A prominent example for this kind of "eastward traveling" planetary waves are the undulations of atmospheric westerlies in the midlatitudes.

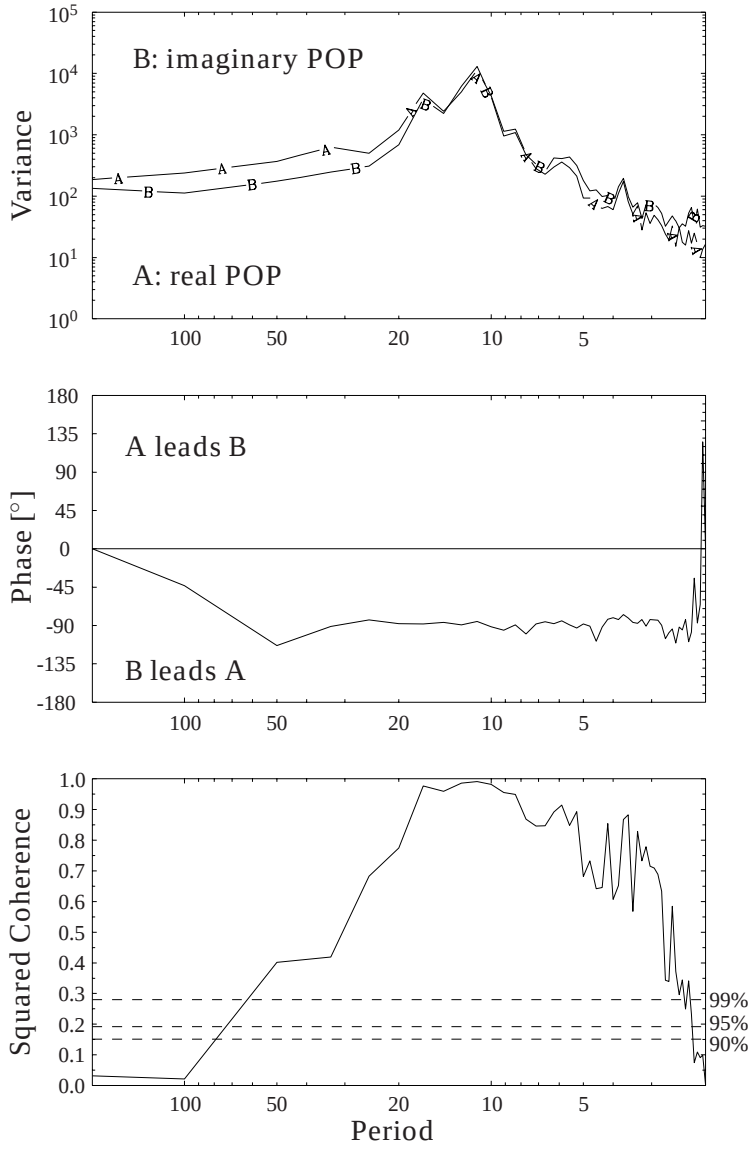

Figure 6.12.: *Spectral analysis of the real (A) and imaginary (B) part of the first POP of the depth of the 27.5 isopycnal for integration years 3500 to 5000 of the control run; variance density spectrum (top), phase spectrum of the cross correlation (middle) and square of coherence of the density spectra (bottom).*

After crossing the Atlantic this wave signal is superimposed on the one coming from the south along the continental slope. The newly composed signal continues along the South American coastline as a Kelvin wave. When it reaches the equator it is deflected to the east and travels along the 0° parallel as equatorial Kelvin wave. At the African coast, part of the wave's energy is reflected as an equatorial Rossby wave; the other part feeds two Kelvin waves that travel poleward along the continental margins of both hemispheres. On their way they disperse long Rossby waves into the interior of the ocean basins. In the

North Atlantic this leads to a distribution of the carried anomaly over almost the entire basin.

A conceptual picture for the spreading of Kelvin and Rossby waves in the manner just explained has been developed by KAWASE (1987). The results of his investigations of the deep ocean circulation with a two-layer model as well as those of KARCHER AND LIPPERT (1994) for a realistic topography served as a guideline for the above argumentation. In a complex OGCM such as the one used here wave processes cannot be observed without disturbances and superpositions. Particularly in the tropical latitudes the superposition of different types of waves together with their small amplitudes make it almost impossible to follow a single signal. Furthermore the West-East course of the equatorial African coastline does not allow wave reflections as in the idealized theory. Another complicating factor is the model's coarse resolution. Baroclinic Kelvin waves with their typical Rossby radii of deformation of only 20 to 30 km at midlatitudes cannot be resolved in the model used here with a spacing of adjacent model grid points of 300 to 400 km. The "Pseudo" Kelvin waves found in the model travel with phase speeds in the order of some cm / s. This is consistent with HSIEH ET AL. (1983), who found a typical underestimation of the phase speed of "real" baroclinic Kelvin waves (0.5 to 3 m / s) by models of the type used here by more than one order of magnitude. Due to these factors the model results cannot be regarded as a true reproduction of reality with respect to time scales and detailed spatial features. Nevertheless, the principal mechanisms, as outlined, appear to be relevant.

The validation of this part of the model results with observational data is difficult due to the sparseness of oceanographic measurements. Comparison with another model study dealing with similar topics, though, does at least serve for an evaluation of the robustness of the phenomenon under different numerical representations. STÖSSEL AND KIM (2001) report periodic events of enhanced convection in the southern high-latitudes with most pronounced amplitudes in the Weddell Sea. Their frequency is similar to the one found here. STÖSSEL AND KIM (2001) suggest two possible mechanisms for the self-sustained character of this oscillation: one involves the advection of sea-level anomalies with the Weddell Gyre. The time scale of one of its full cycles matches that of their decadal oscillation. The other names the propagation of baroclinic Kelvin waves northward along the western boundary and eastward along the equator. The temperature and salinity anomalies associated with this wave propagation modify the outflow of NADW across 30°S and influence the properties of Lower Circumpolar Deep Water, which in turn preconditions the periodic convective instabilities. The periodic changes in NADW outflow could not be found in the investigation performed here. On the other hand, STÖSSEL AND KIM (2001) do not detect a signal comparable to the one crossing the South Atlantic towards America in the present study, nor do they discuss possible influences on the northern hemisphere. In the present study, the periodic enforcement of convective activities takes place in the region east of the Weddell Sea. Due to the differences between the results presented here and those of the study by STÖSSEL AND KIM (2001) their explanation for this oscillation seems not generally valid. The question remains: what is the

nature of this self-sustaining oscillation and which mechanisms maintain it? The number of frequencies contained in the present model and the complexity of interactions on different time scales did not allow to give a final answer. Future investigations will have to unveil the nature of this variability. As the detected anomalies are very prominent in the Drake Passage throughflow an explanation will have to consider the influence the ACC exerts on the deep water production in the Southern Ocean.

7. Forcing Variations

In the previous chapters the *status quo* of the ocean and part of its inherent variability have been described. This kind of investigation is restricted to the natural variability of the system and weak modifications of a quasi-equilibrium state. To study the interplay of water masses more closely perturbations of the surface forcing have been introduced into the system. This allows to investigate the temporal evolution of anomalies revealing mechanisms of interaction and information transfer. Two sets of experiments have been performed: changes of the surface buoyancy forcing with its possible direct influence on the thermohaline circulation will be examined in section 7.1. Alterations of the wind forcing are treated in section 7.2.

In all of the following experiments the disturbances were introduced into the model in the year 3490 of the control run. Then the model was integrated for another 1500 years keeping these disturbances. As a reference the control run was continued unchanged over the same time.

7.1. The Buoyancy Experiments

The convective process is very sensitive to perturbations in certain areas as shown e.g. by LENDERINK AND HAARSMA (1994). They identified potentially convective regions, where convection can easily be triggered or stopped. The idea here was to use such sensitive areas to strengthen or slow down convective activities and deep water formation. The passive tracer plots of Figs. 4.7 and 4.8 point to the regions where this approach could be promising: the Labrador Sea and the Weddell Sea. Nine grid boxes were selected in each region (compare Fig 7.1). There, the values to which the salinity was restored, were manipulated by adding or subtracting 0.5 or 1 psu to or from the climatological values as indicated in Table 7.1. These changes lie within the range of observed anomalies (as e.g. during the great salinity anomaly as described in section 2.5, also compare DICKSON ET AL., 1988).

In Fig. 7.2 the total kinetic energy per unit volume is displayed. From this graph, four conclusions can be drawn immediately: the runs with the positive salt anomalies show stronger deviations from the control run than those with negative ones. The deviations have opposite signs between the hemispheres, i.e. positive salt anomalies in the Weddell

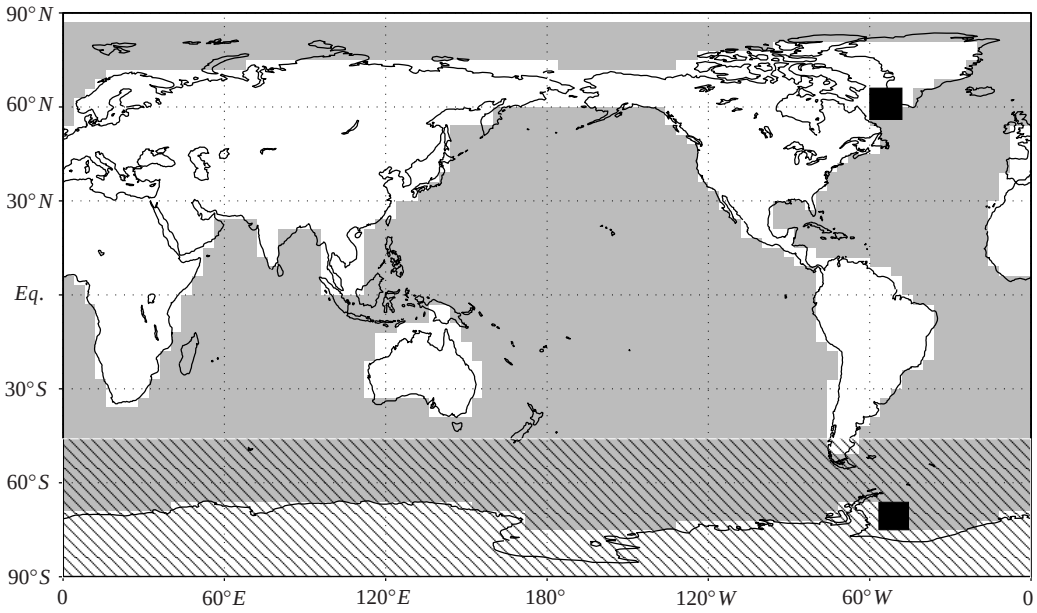

Figure 7.1.: *Manipulated regions for sensitivity studies. The black boxes mark the grid cells where the salinity restoring was changed. The hatched area is that of changed wind stress in the TAU experiments.*

Experiment	Salinity	ACC		NADW		AABW	
		[Sv]	Δ[%]	[Sv]	Δ[%]	[Sv]	Δ[%]
CTRL	$\pm 0\,psu$	236.0	0	24.81	0	1.61	0
LAB++	$+1\,psu$	220.9	−6.3	30.83	24.3	1.91	18.6
LAB+	$+0.5\,psu$	224.0	−5.1	31.17	25.6	1.87	16.1
LAB––	$-1\,psu$	237.4	0.6	23.78	−4.2	1.55	−3.7
WED++	$+1\,psu$	267.5	13.3	22.95	−7.5	2.15	33.5
WED––	$-1\,psu$	229.2	−2.9	25.12	1.2	1.48	−8.1

Table 7.1.: *Characteristic values for LAB and WED experiments. The salinity column gives the respective restoring changes as explained in the text. ACC: Drake Passage throughflow; NADW: maximum of the streamfunction for the zonally integrated volume transport below the surface layer in the North Atlantic; AABW: amount of the minimum of the streamfunction below 3000 m depth in the North Atlantic – all values are means of the 49th century of integration. The Δ columns give the deviation from the control run in %.*

Sea lead to a positive energy deviation, while positive salt anomalies in the Labrador Sea show negative energy deviations and vice versa. The amplitude of the WED experiments are bigger than those of the LAB runs with the same anomaly strength and the system does not instantly switch to another state, but is slowly adjusting to a new equilibrium.

The magnitude of the ACC dominates the global kinetic energy budget as it is by far the strongest current system on earth. Table 7.1 reflects this connection; runs with positive

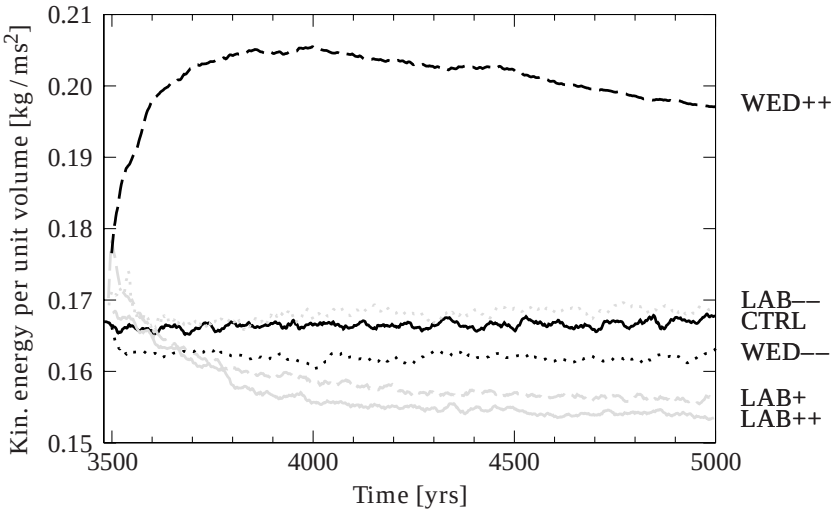

Figure 7.2.: *Total kinetic energy (20 years running average over January values) of runs CTRL (solid black line), LAB++ (solid grey), LAB+ (dashed grey), LAB–– (dotted grey), WED++ (dashed black) and WED–– (dotted black).*

kinetic energy deviations from the control run also show positive deviations in the Drake Passage throughflow and vice versa. At the same time positive (negative) anomalies in the ACC strength are connected to negative (positive) anomalies in the NADW strength. The reaction of AABW is non-uniform. The reason for different behavior of the LAB and WED runs could possibly lie in different mechanisms and processes that are set off by introducing the anomalies either in the northern or the southern hemisphere. They will therefore be investigated separately.

7.1.1. Labrador Sea Salinity

It seems to be straightforward that adding salt to the surface waters of the Labrador Sea triggers a strengthening of the North Atlantic MOC. It weakens the stratification and hence leads to an intensification of the convective activity. The threshold value needed to increase deep water production appears to be rather low. There is no significant difference in the strength of the NADW cell between runs LAB+ (+0.5 psu: 31.2 Sv) and LAB++ (+1 psu: 30.8 Sv). Both show a small cell with positive anomalies close to the southern slope of the Greenland-Scotland-Ridge, with an adjacent small negative anomaly (Fig. 7.3). This indicates a northward shift of the overturning cell for these experiments. The entire cell south of 40°N is strengthened resulting in an intensified cross-equatorial transport. At the same time the cell extends to greater depths (almost 3.5 km instead of little more than 2.5 km in the control run (Fig. 4.5). The altered overturning cells have a direct effect on the temperature and salinity fields of the Atlantic Ocean. As can be seen from the zonally averaged sections of Fig. 7.4 the ocean at intermediate depths becomes colder and fresher. This is due to a subduction of Labrador Sea surface water that is cold and fresh compared to these depths. As the overturning cell now reaches

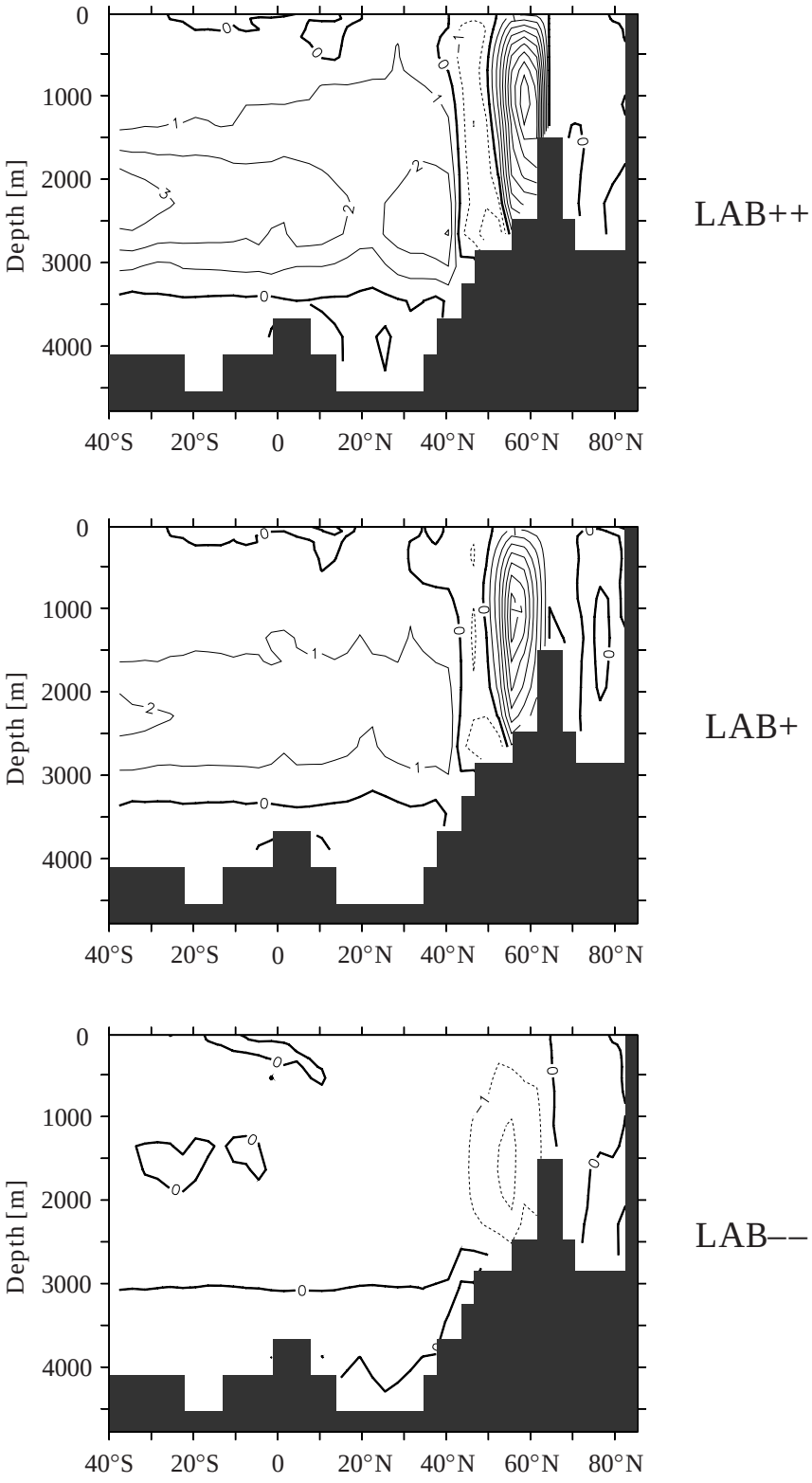

Figure 7.3.: *Mean meridional overturning streamfunction for the Atlantic in Sv – deviations from run CTRL; integration years 4900 to 4999 for runs LAB++ (upper), LAB+ (middle) and LAB–– (lower panel). Contour interval is 1 Sv.*

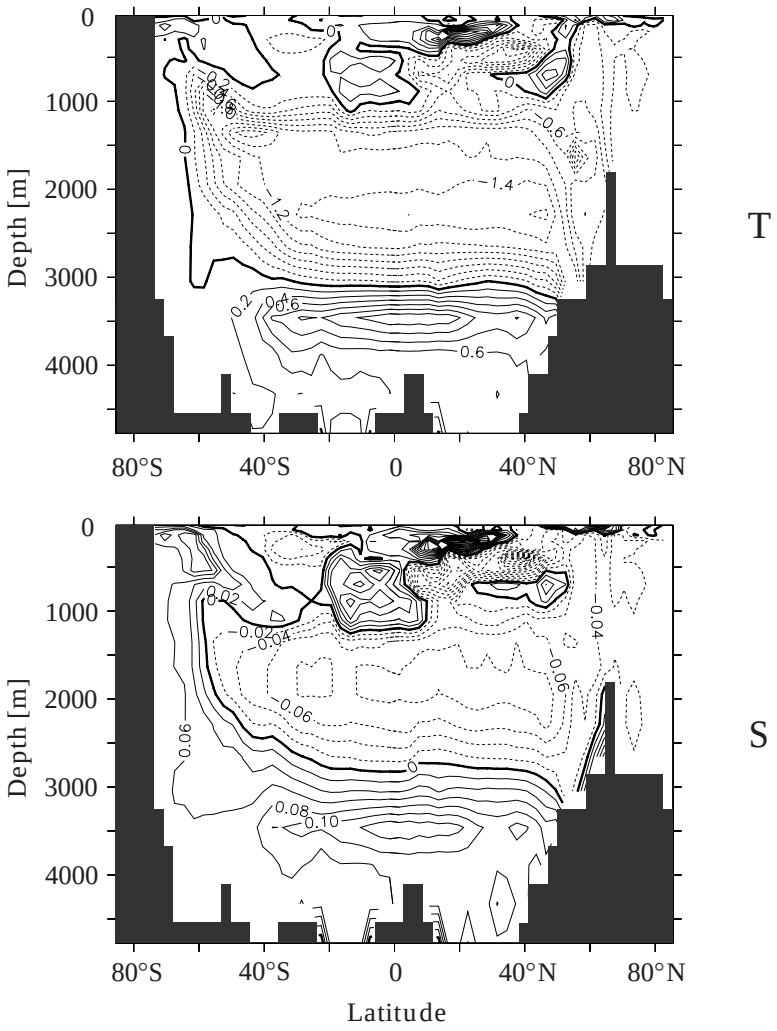

Figure 7.4.: *Atlantic zonal mean of potential temperature (top) and salinity (bottom); deviations of run LAB++ from CTRL; integration years 4900 to 4999. Contour interval is 0.2°C and 0.02 psu, respectively.*

deeper, Labrador Sea surface water is transported also into depths below 3 km. There it causes the deep ocean to become warmer and saltier. The effect of the strengthening of the AABW cell in the LAB++ case (approximately 0.3 Sv according to Table 7.1) can not be detected in temperature and salinity of the deep ocean as the increase of the NADW cell (by 6 Sv) is predominant there. The changes in the characteristics of the upper 1000 m can be explained by a shift of the pycnocline induced by changed upwelling and the stronger intrusion of subpolar mode waters. For LAB–– the deviations from the control run are small. There is a negative anomaly in the meridional overturning south of the Greenland-Scotland-Ridge (Fig. 7.3, bottom). This indicates a weaker overturning, which in turn leads to a weak temperature decrease in deeper layers (not shown). There is no salinity signal for that case.

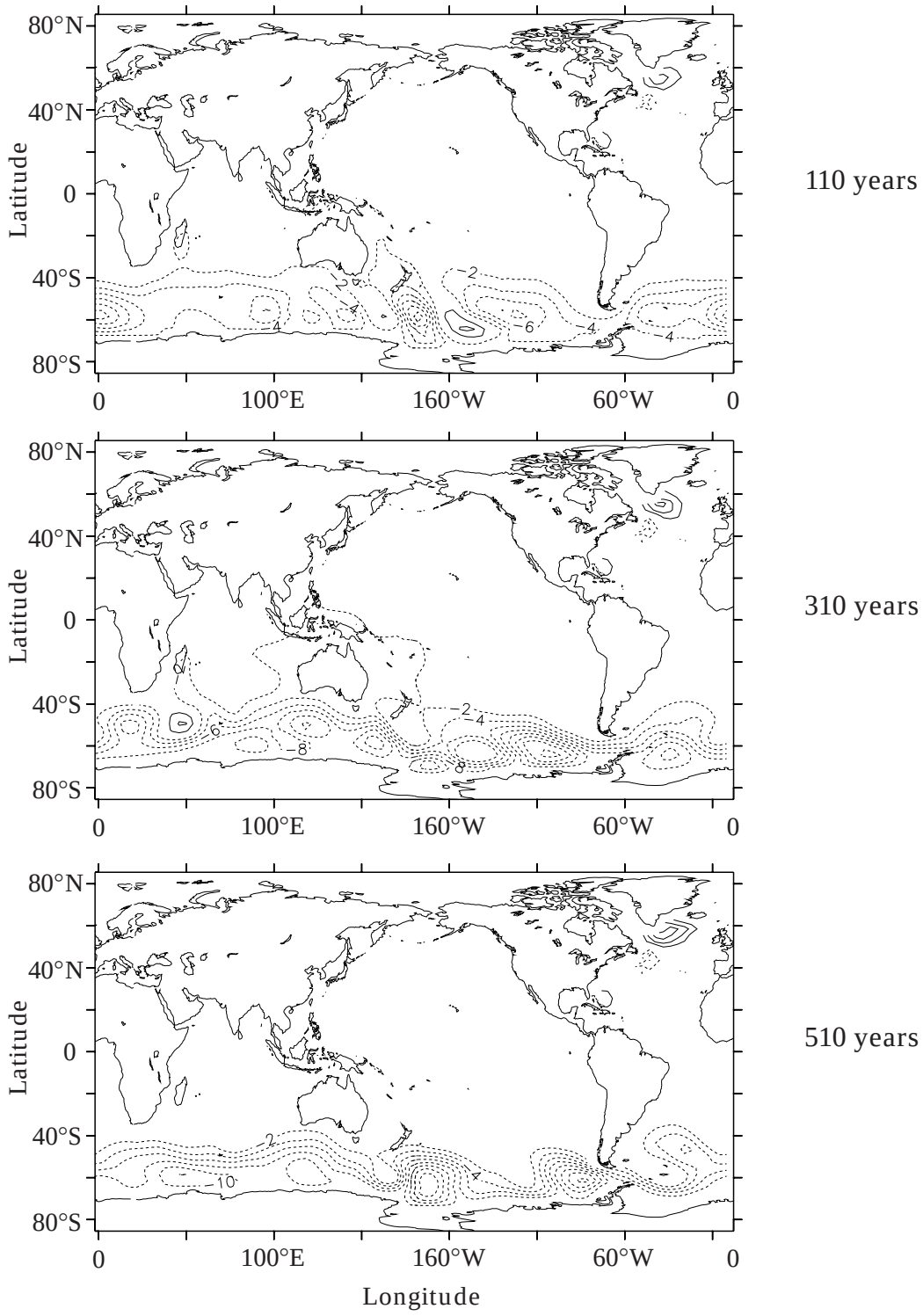

Figure 7.5.: *Mean barotropic mass transport streamfunction; deviations of run LAB++ from CTRL; annual means for integration years 110 (top), 310 (middle) and 510 (bottom) after introduction of the salinity anomaly. Contour interval is 2 Sv; the 0 Sv contour is suppressed.*

In run LAB++ the changes of the barotropic mass transport streamfunction are dominated by the weakening of the ACC transport (Fig. 7.5). There is no instantaneous reaction of the streamfunction to the alteration in salinity restoring, but a gradual diminishing. After 110 years (top of Fig. 7.5) no coherent trend for the ACC as a whole can be described. A weak wave-like pattern of negative anomalies has formed. After 310 years (middle) the single patches have merged and form a circumpolar structure that intensifies over the next 200 years (bottom). This pattern then persists during the further integration. Outside the Southern Ocean, there is a positive anomaly at the source region of the disturbance, which decreases the strength of the cyclonic cell existing there, thereby deviating parts of the Gulf Stream and the North Atlantic Current (Fig. 7.6). The surface waters are now transported directly into the Labrador Sea to feed the strengthened NADW cell. The LAB–– experiment shows only minor changes in the streamfunction (not shown). There is no clear signal of a strengthening of the ACC. Its centennial mean value exceeds that of the control run by less than 1% after 1500 years of integration. There is a very weak wave-like pattern with a similar structure as that of Fig. 7.5 (middle) for single years, but in centennial means this pattern is not visible.

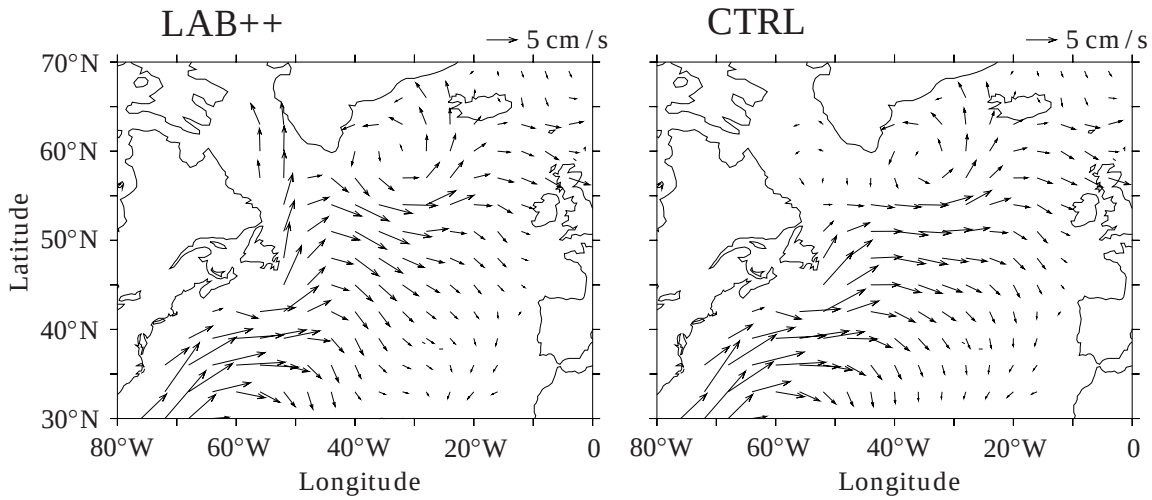

Figure 7.6.: *Surface velocities in the North Atlantic; runs LAB++ (left) and CTRL (right); mean over integration years 4900 to 4999; the reference arrows represent 5 cm/s.*

The temporal evolution of the main characteristics of the global and Atlantic Ocean circulation after introducing the anomalies is illustrated in Fig. 7.7. On the left deviations of annual means from the control run for the first 110 years after switching on the anomalies are displayed; the right panels show 50 years running averages for the first 510 years. In both plots the deviations are in % relative to the control run. For the LAB++ experiment (upper panels) an instantaneous reaction of the NADW strength (solid black line) can be seen with an intensification of the streamfunction maximum by almost 70%, followed by a smooth decline to its final value of 25% 500 years later. The absolute value of the deep minimum of the overturning streamfunction in the Atlantic Ocean repre-

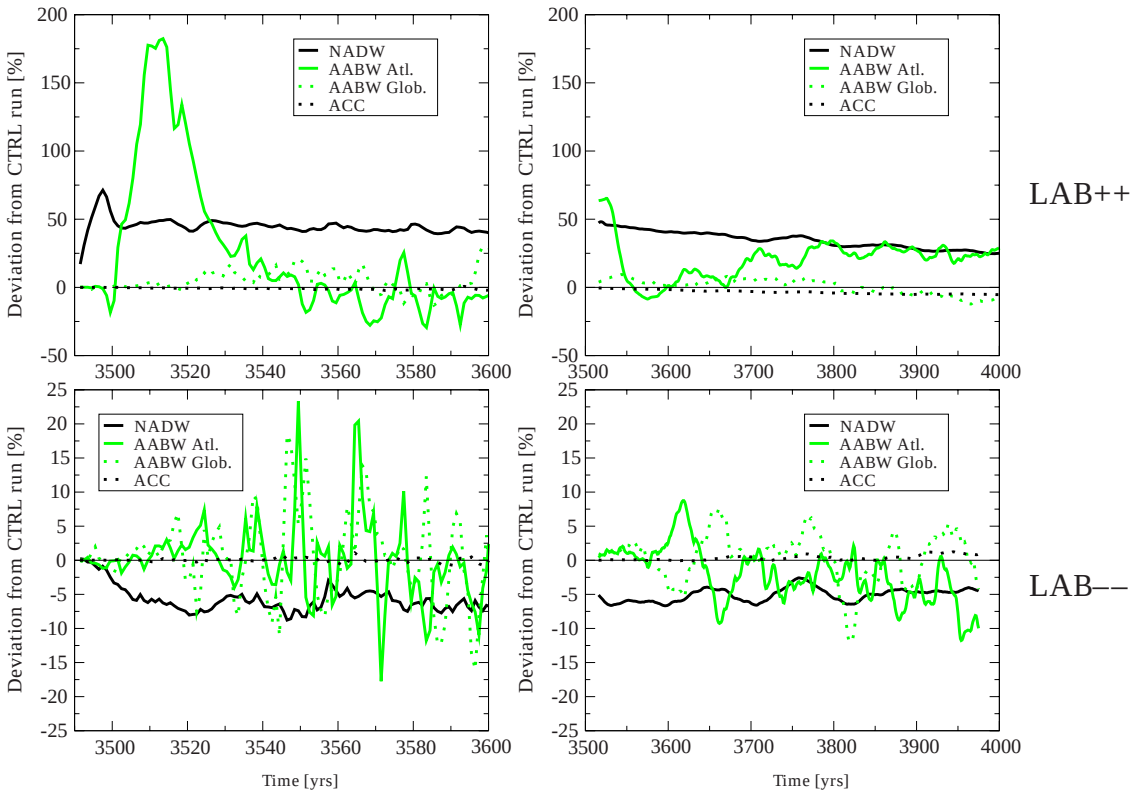

Figure 7.7.: *Temporal evolution of deviations from CTRL in % for NADW (solid black), ACC (dotted black), Atlantic (solid grey) and global AABW (dotted grey). NADW, ACC and (Atlantic) AABW are defined as in Table 7.1; global AABW: amount of the minimum of the global overturning streamfunction below 300 m depth. Top: LAB++; bottom: LAB––. Left: annual means for the first 110 years after introduction of the anomalies; right: 50 years running averages for the integration years 3490 to 4000; scales are different between the plots; note that the dotted black ACC curve meets the abscissa or is close to it during most of the time.*

sents the maximum strength of the AABW in this basin, which is located in the northern hemisphere. Its reaction has a delay of about 10 years (solid grey line) compared to the NADW signal and shows an intense peak with an amplification by almost 200% after 20 years. In the course of the integration it reaches an increase in the order of magnitude of the NADW signal. It should be kept in mind that in the control run the strength of the AABW cell is less than 2 Sv, while the NADW value almost reaches 25 Sv. Furthermore, there is variability on a number of different time scales superimposed on this signal. A similar degree of variability can be found in the global AABW extremum (defined as the absolute value of the minimum of the global vertical overturning streamfunction below 300 m depth which typically is located south of 40°S – displayed by the dotted grey curve). It takes 30 years before a deviation from the control run becomes noticeable. The signal in the Drake Passage throughflow (dotted black line) is more steady showing a continuous decrease of the ACC strength. The LAB+ experiment shows characteristics and amplitudes similar to those of LAB++ (not shown). For the LAB–– experiment

the amplitudes of the deviations are far weaker than for the runs with positive salinity anomalies. The outstanding peaks of the first years in the LAB++ case are not present. Except for NADW, which shows a decrease of about 5%, the deviations oscillate around zero. Fig. 7.7 indicates that the global and the Atlantic AABW signals are out of phase.

The mechanism revealed by the Labrador Sea experiments can be described as follows: introduction of additional salt into the surface layer of the Labrador Sea destabilizes the water column. An unstable water column triggers additional convection, strengthens the deep water production, and deepens the meridional overturning cell. The altered density structure changes the ambient conditions in the intermediate and deep layers of the Atlantic Ocean. In a first phase the Atlantic branch of the AABW intensifies and then collapses. Then the AABW cell slowly re-establishes. The density anomalies are advected southwards with the Atlantic conveyor and subsequently change the water mass properties in the southern hemisphere. The altered structure of the deep density field with decreased meridional gradients in turn changes the magnitude of water mass transport in the ACC. The experiment with the negative salinity anomaly in the Labrador Sea does not show substantial changes in the circulation patterns and water mass properties. Theoretically, a freshwater injection into the ocean (which the negative salinity anomaly amounts to) stabilizes the water column, thereby weakening and/or hindering deep water formation. This does not take place in the LAB−− experiment. The explanation is that the model's deep water formation region was not met with the grid boxes chosen[a]. As there is only little to no deep water formed in this region, it is obvious than it can not be diminished by stabilizing the stratification. The effect of a slight weakening of the NADW cell that can be seen from the lower graphs of Fig. 7.7 is then to be explained by the advection of the less saltier water masses to the adjacent convection sites with subsequent stabilization of the stratification there.

7.1.2. Weddell Sea Salinity

The Weddell Sea experiments show some substantial differences to the Labrador Sea runs. The changes in the Drake Passage throughflow and the strength of the AABW cells are much more pronounced than in the NADW cells. In contrast to the LAB experiments the changes in AABW and NADW have opposite signs (compare Table 7.1). NADW is less affected than in the LAB experiments by about two thirds. This is not surprising as there is no direct influence on the North Atlantic MOC in form of changed boundary conditions in the region of deep water formation. A closer look at the overturning streamfunctions of run WED++ (Fig. 7.8, a and c) reveals a strengthening of the global AABW cell with its deep extremum in the southern hemisphere increasing from about 8 to more than 13 Sv. The AABW cell becomes thicker and extends now from 2600 m to the bottom. The positive anomaly along the continental slope of Antarctica indicates that

[a]This was not realized before the model integration had been carried out completely. As another run (WED−−) that included the desired effect of slowing down deep water production was successful, I decided to keep LAB−− even if its results highlight different mechanisms than those originally in mind.

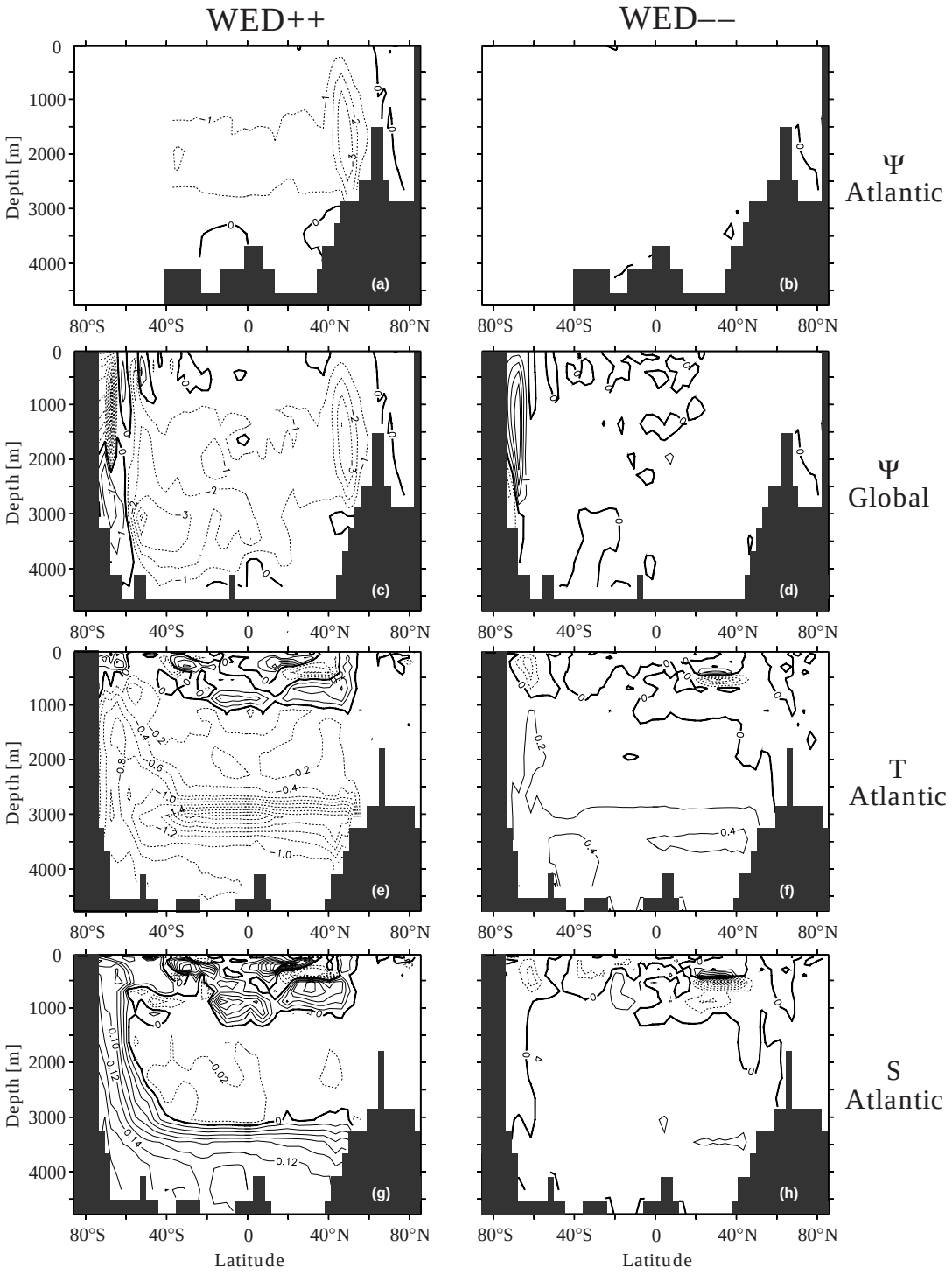

Figure 7.8.: *Mean meridional overturning streamfunction in Sv, for the Atlantic (a and b) and worldwide (c and d); Atlantic zonal means of potential temperature (e and f) and salinity (g and h) – deviations from CTRL; integration years 4900 to 4999 for runs WED++ (left) and WED−− (right). Contour interval is 1 Sv, 0.2°C and 0.02 psu, respectively.*

the sinking into the deeper levels now takes places further North. The Atlantic Ocean only gets a small share (less than one Sv) of this intensification in the abyssal levels. On the other hand, the negative anomaly in the global overturning extends to the North in intermediate levels. This part of the signal is dominated by the Atlantic MOC which shows a negative maximum of 3 Sv close to the Greenland-Scotland-Ridge with a weakening of the cross-equatorial transport by more than one Sv. In the WED–– case (Fig. 7.8, b and d) the reaction of the ocean is far weaker, but definitely more intense than in the LAB–– case. The global overturning (Fig. 7.8 d) shows a positive anomaly in the upper 3 km along the Antarctic continental slope indicating decreased sinking. This weakening, however, has almost no influence onto the abyssal layers and the rest of the overturning streamfunction. Especially in the Atlantic there are no relevant changes (Fig. 7.8 b).

An intensified deep water production south of the ACC results in subduction of cold ($T < -1°C$) and salty (34.9 – 35.1 psu) water in run WED++, thus changing the abyssal water mass properties accordingly (compare Fig. 7.8, e and g). The meridional density gradient of the Atlantic Ocean is increased. In intermediate depths between 1 and 2.5 km temperature and salinity are almost unchanged. The WED–– experiments yield slightly higher temperatures in the abyssal ocean, while there is only little change in the salinity properties there (Fig. 7.8, f and h).

As in the experiments of the previous section the horizontal streamfunction anomaly (Fig. 7.9) is dominated by the ACC. Unlike the LAB++ run there is no wave-like structure but smooth isolines showing an overall intensification of the ACC. It reaches its equilibrium value faster than in the LAB cases. Fig. 7.9 shows no major adjustments after the state of 310 years has been reached. The Weddell Sea and the Ross Sea gyre are intensified. The southern hemisphere subtropical gyres in the Atlantic, Pacific and Indian Oceans are strengthened, too, while there are almost no signals in the North. WED–– is similar to LAB–– with respect to the longer time that is needed to reach a steady pattern. The difference, though, lies again in the amplitudes that are more pronounced for the Weddell Sea salinity anomaly run (not shown).

The temporal evolution of the global AABW maximum as indicated by the dotted grey line in Fig. 7.10 shows the immediate reaction of the deep water production to changes in surface salinities. Unlike the LAB experiments the instantaneous onset of the global AABW signal can be seen in the case of the negative anomaly (bottom panels) as well. The expected sensitivity to freshwater intrusions as formulated by LENDERINK AND HAARSMA (1994) is confirmed here. The WED++ run (Fig. 7.10, top) shows an intensification of the AABW production to about two and a half times its size with a slow subsequent fall to twice its strength. The Atlantic AABW signal reacts with a delay of 10 to 15 years to the disturbance, also showing an increase. The proximity of the deep water formation region in the Weddell Sea to the ACC allows a fast change in the water mass transport of the latter. An increased density gradient in the deep Southern Ocean is established rapidly. Hence, the onset of an ACC intensification can be observed within the first years after the anomaly is introduced. The NADW cell shows no detectable de-

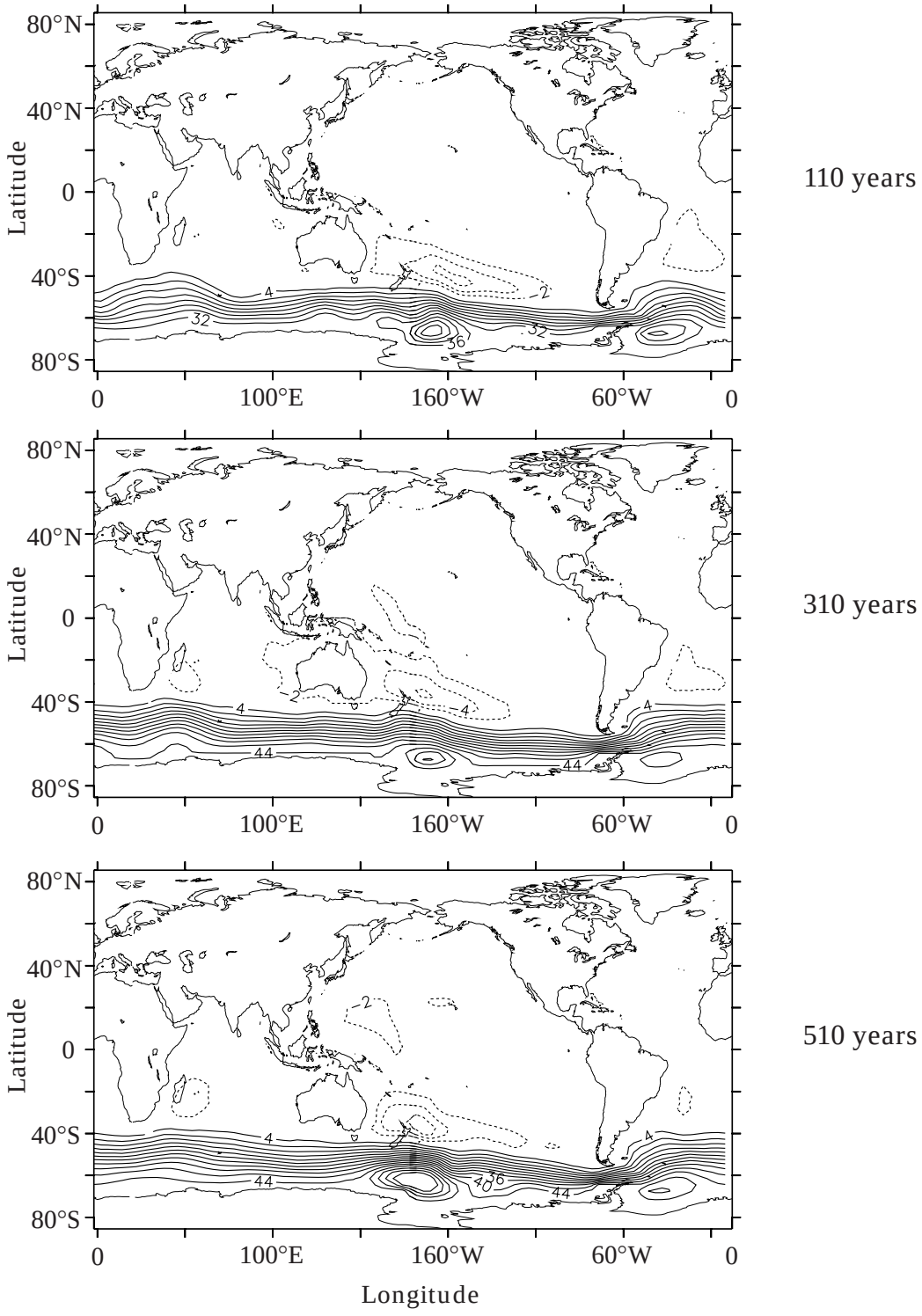

Figure 7.9.: *Mean barotropic mass transport streamfunction; deviations of run WED++ from CTRL; annual means for integration years 110 (top), 310 (middle) and 510 (bottom) after introduction of the salinity anomaly. Contour interval is 4 Sv for positive, 2 Sv for negative values; the 0 Sv contour is suppressed.*

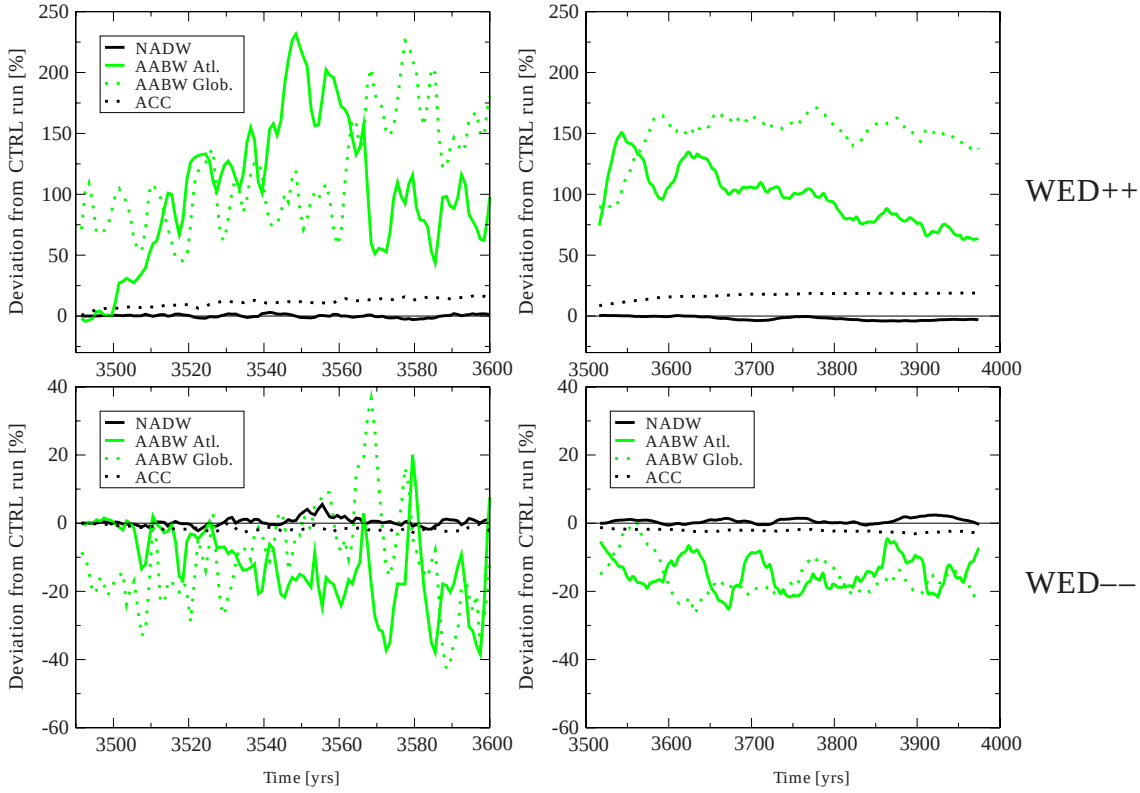

Figure 7.10.: *Temporal evolution of deviations from CTRL in % for NADW (solid black), ACC (dotted black), Atlantic (solid grey) and global AABW (dotted grey). NADW, ACC and (Atlantic) AABW are defined as in Tab. 7.1; global AABW: amount of the minimum of the global overturning streamfunction below 300 m depth. Top: WED++; bottom: WED−−. Left: annual means for the first 110 years after introduction of the anomalies; right: 50 years running averages for the integration years 3490 to 4000; scales are different between the plots.*

viation from the control run for the first 150 years. Afterwards a slight decrease can be observed. For the WED−− run the above argumentation holds with reversed signs, i.e. the strength of the AABW cell and the ACC decreases, while the NADW signal remains almost unchanged with a slight tendency to higher values. However, the amplitudes are clearly weaker (note the different scales of the ordinates in Fig. 7.10).

7.2. The Wind Stress Experiments

The strongest wind fields around the globe are observed in the southern hemisphere in the latitude band that is not blocked by continents. Hence, it can be expected that the influence of variations in the wind forcing on the ocean circulation is substantial in this region. Indeed, several studies with models of different degrees of sophistication (TOGGWEILER AND SAMUELS, 1993a, 1995, 1998; CAI AND BAINES, 1996; MCDERMOTT, 1996;

GNANADESIKAN, 1999; HASUMI AND SUGINOHARA, 1999) have shown the fundamental sensitivity of the global circulation and deep water production to variations in Southern Ocean wind stress. In the context of the present work this kind of experiments is repeated for two reasons: to compare the model's capability to represent dynamical processes to that of other models and to complete the set of possibly important manipulations to the deep water production processes. The model's sensitivity to altered wind forcing is investigated by analyzing the results of three experiments. To portray the manipulations carried out, the mean zonal component of the annual mean windstress is displayed in Fig. 7.11. To ensure a smooth transition to the altered values the wind stress is amplified gradually to 1.5 times of its amplitude for run TAU+, to half of its strength for TAU– and to zero for TAU 0 between 30°S and 50°S. South of 50°S (i.e. covering the latitude band of the Drake Passage) the amplification factor is kept constant. The use of zonal means in Fig. 7.11 serves only as an illustration; the amplification factors have been applied to the zonal as well as to the meridional wind stress components, using time dependent ECMWF climatological data (FRITZSCH ET AL., 2000) as described in section 3.5.

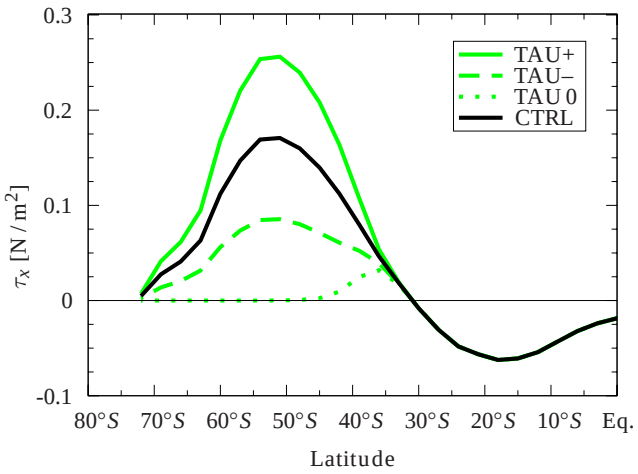

Figure 7.11.: *Zonally averaged annual mean of the zonal wind stress in N/m^2 as a function of latitude for the southern hemisphere. The black curve denotes the ECMWF climatological value (FRITZSCH ET AL., 2000); the grey lines show the amplifications used for TAU+ (solid), TAU– (dashed) and TAU 0 (dotted).*

The production rate of NADW (circles in Fig. 7.12), the cross-equatorial volume transport of the Atlantic deep circulation (not shown) and the extrema of the Atlantic AABW cell (squares) are approximately proportional to the factor by which the wind stress is multiplied. If one only takes into account the cases with wind stress (TAU+, CTRL and TAU–), a quasi-linear relation is also valid for the strength of the Drake Passage throughflow (stars in Fig. 7.12). For TAU 0 the ACC stops almost completely (6.5 Sv), while a linear extrapolation of the other runs' behavior would yield about 50 Sv. The quasi-cessation of the ACC is in contradiction to the results of CAI AND BAINES (1996), who report ACC strengths between 24 and 85 Sv for their experiments without wind forcing but with bottom topography depending on the other model parameters chosen. A possi-

ble reason for this discrepancy could be a too short integration time in their model runs. In the experiment presented here the strength of the ACC is subject to a gradual decrease (compare Fig. 7.17, bottom) that can be explained by a slow consumption of potential energy stored in the ocean. As the time scale for the adjustment of the ACC's strength is larger than 1000 years, the use of rates of change of the global-mean temperature and salinity as criterion for an equilibrium state as used by CAI AND BAINES (1996) may be misleading. The maximum of the global AABW cell (triangles in Fig. 7.12) does not fit into the picture of a quasi-linear decrease with reduction of the wind stress at all: it has its maximum in the control run and values that are smaller by 20% for the TAU+ and TAU– cases. For TAU 0 the Antarctic bottom water production has ceased almost completely.

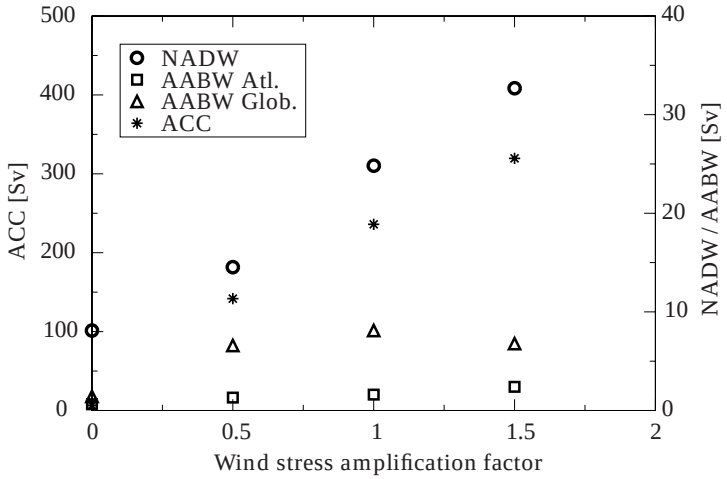

Figure 7.12.: *Maxima of NADW (○), Atlantic AABW (□) and global AABW (△) cells and strength of ACC at the Drake Passage (∗) for integration years 4900 to 4999 plotted against the factor by which the climatological wind stress over the Southern Ocean is multiplied; the numbers on the left ordinate reflect the ACC values, the right ordinate all others.*

The quasi-linearity of the relation between the wind stress amplification and the water mass transport in the ACC for TAU+ and TAU– is illustrated by the upper two panels of Fig. 7.13, showing the deviations of the horizontal streamfunctions for the runs TAU+ (top) and TAU– (middle) from the control run for the last century of the integration. The patterns look alike; just the signs are reversed. In TAU+ the intensification of the Drake Passage throughflow by more than 80 Sv is accompanied by stronger subtropical gyres in the southern hemisphere. The differences in case of the TAU– anomalies (besides their sign) lie in a stronger amplitude for the subtropical gyre of the Indian Ocean and in a positive anomaly at the south-eastern tip of Greenland. This is illustrated further by Fig. 7.14, which shows surface velocity anomalies. For TAU+ (left) the Gulf Stream / North Atlantic Current system intensifies and penetrates further north, while in the TAU– run it is weakened and hardly reaches 60°N. The horizontal streamfunction of experiment TAU 0 in the lower panel of Fig. 7.13 reflects the almost complete shut down of the Circumpolar Current. The southern hemisphere's subtropical gyres are weakened. They now have a strength comparable to their northern hemisphere counterparts. Again the only notable

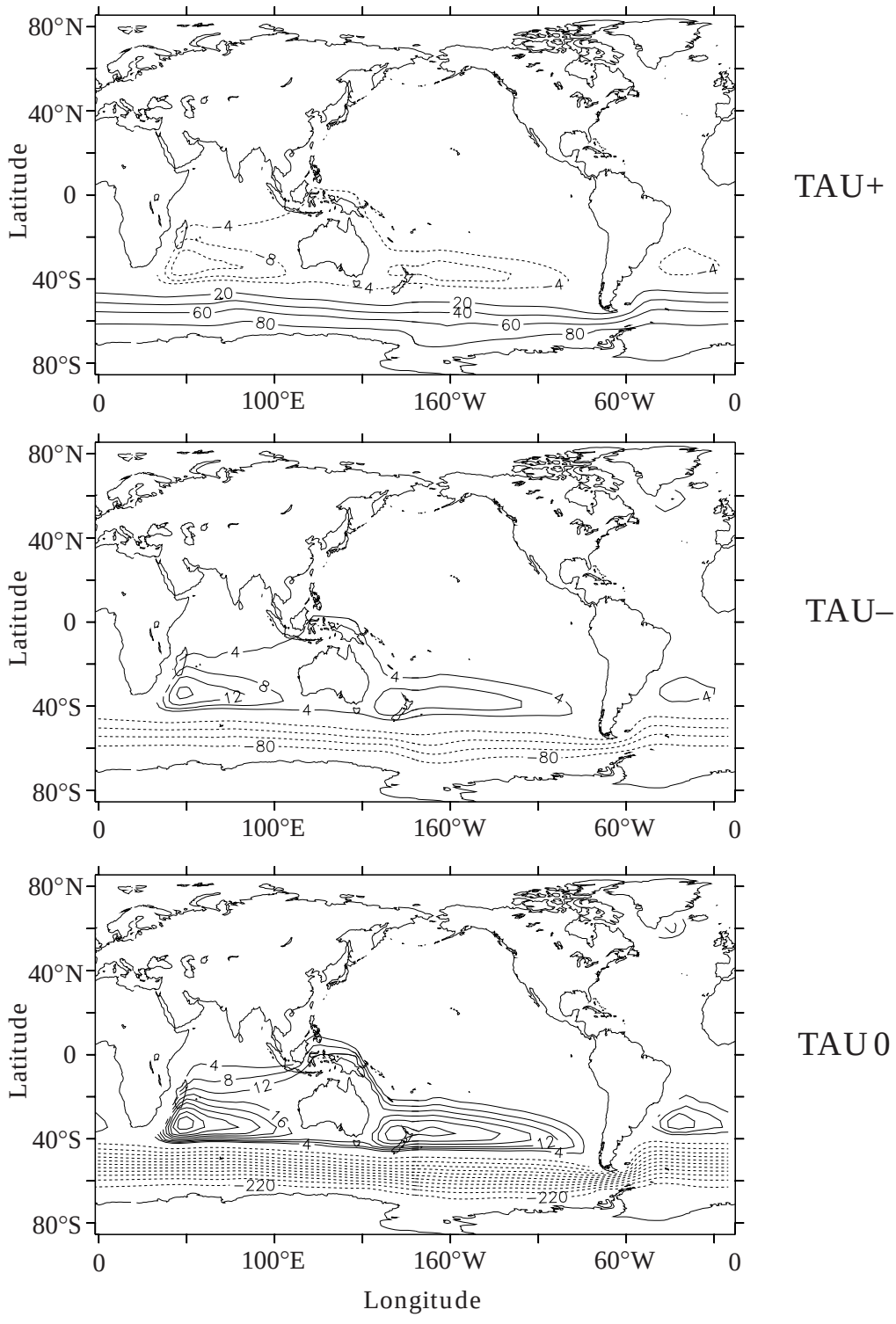

Figure 7.13.: *Mean barotropic mass transport streamfunction; deviations of run TAU+ (top), TAU– (middle) and TAU 0 (bottom) from CTRL; annual means for integration years 4900 to 4999. Contour intervals differ between the runs: for negative values they are set to 4 (20) Sv, for positive to 20 (4) Sv for TAU+ (TAU– and TAU 0), respectively; the 0 Sv contour is suppressed.*

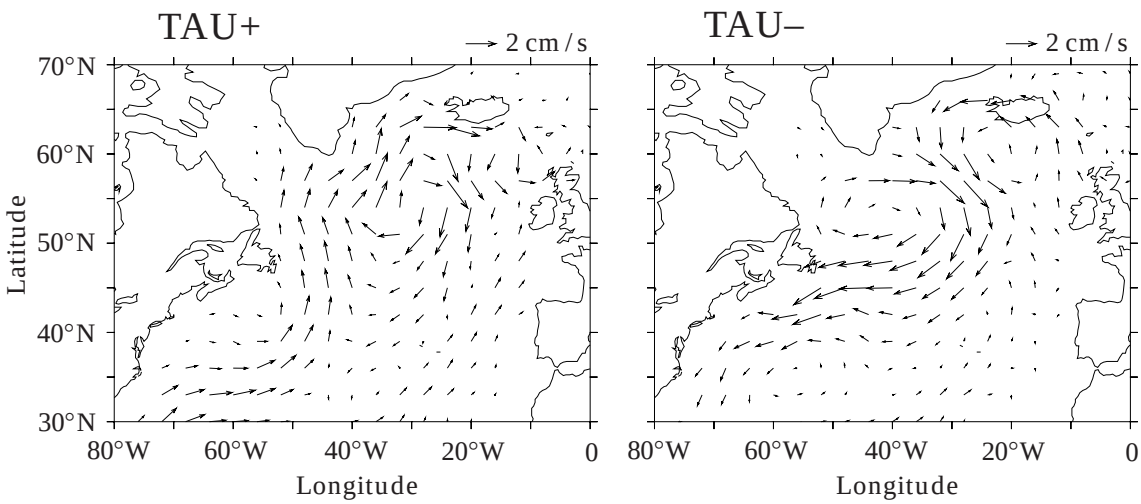

Figure 7.14.: *Surface velocity anomalies in the North Atlantic; deviations of run TAU+ (left) and TAU– (right) from CTRL; mean for integration years 4900 to 4999; the reference arrows represent 2 cm/s.*

anomaly outside the southern hemisphere lies in the northern North Atlantic. The Gulf Stream there is weakened further compared to TAU– and takes a more zonal course (not shown).

The altered circulation in the northern North Atlantic Ocean is also reflected in the meridional overturning. Fig. 7.15 shows the temporal evolution of the global (left) and Atlantic (right) cells for run TAU+. The annual means for the first year after the wind anomalies have been applied (top graph) show a strong signal with a positive anomaly in the Deacon cell, i.e. centered at 50°S and reaching down to the bottom of the ocean. Part of this anomaly can be seen in the Atlantic Ocean extending almost to the equator. After 10 years (upper middle graphs) a strong positive anomaly at the Greenland-Scotland-Ridge has developed, while the anomaly in the southern hemisphere extends further to the north. Another 10 years later (lower middle) the anomaly in the North Atlantic Ocean has weakened, broadened and moved southward, merging with the cell expanding from the South. Thus, the entire ocean basin up to 42°N is covered by a positive anomaly. North of it there is a small and shallow (reaching only down to 1500 m) negative anomaly with a maximum of 4 Sv located in the Atlantic basin. This indicates that the sinking regions for NADW are temporarily shifted southwards. The small cell vanishes within the next years (not shown). In year 510 (lowest panel) the overturning anomalies have reached a “final” state that is characterized by a positive cell in the Atlantic Ocean with strongly enhanced sinking at the Greenland-Scotland-Ridge and regions of massive upwelling in the Southern Ocean. The intense positive anomaly of year 10 at the Greenland-Scotland-Ridge can be interpreted as evidence for a thermohaline signal leading to a locally altered stratification. This contradicts the idea of the “Drake Passage effect” (compare section 2.7 and the discussion later in this chapter) as causing a “purely

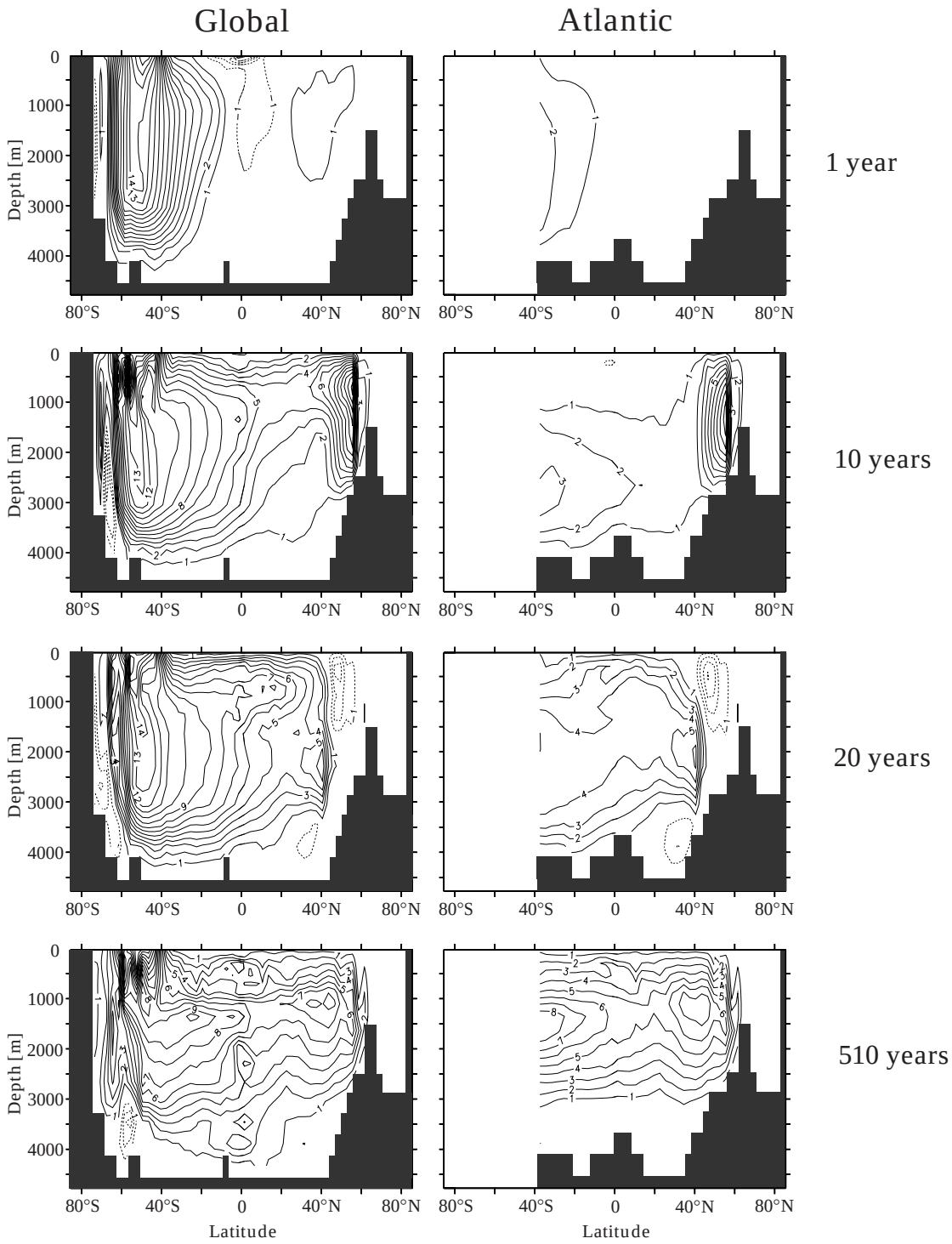

Figure 7.15.: *Mean meridional overturning streamfunction in Sv, worldwide (left) and for the Atlantic (right) – deviations of run TAU+ from CTRL; annual means for integration years 1 (top), 10 (upper middle), 20 (lower middle) and 510 (bottom) after introduction of the wind anomaly. Contour interval is 1 Sv.*

passive transit" of wind induced mass transport into the Northern Atlantic with subsequent sinking there due to the presence of stable stratification elsewhere.

The structure of the water mass characteristics in the Atlantic Ocean is of course influenced by the dramatically changed deep water formation. In Fig 7.16 the potential temperature (top) and salinity deviations (bottom) for the zonally averaged Atlantic Ocean of run TAU+ show a warming of almost the entire basin north of 60°S. Nearly the same region has also become saltier. Both quantities exhibit basin-wide maxima in 1 km and 3.5 km depth. The only exceptions are the intermediate water tongues showing negative temperature anomalies and lower salinities, as well as the surface layers.

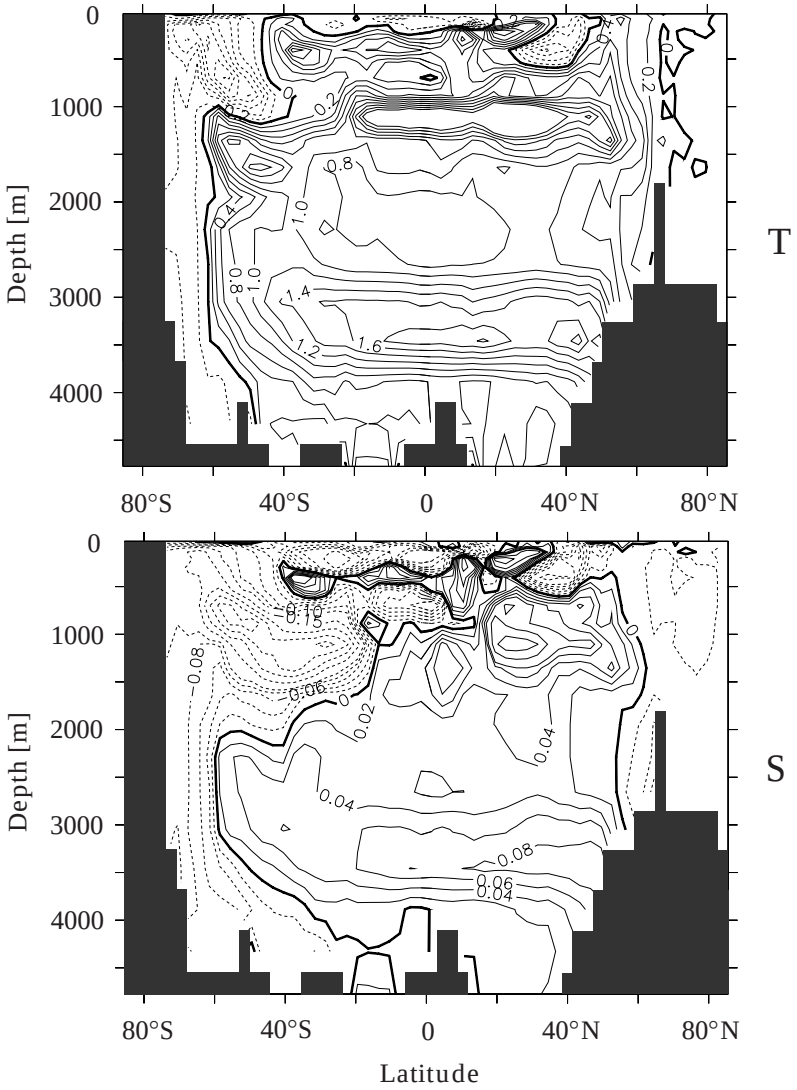

Figure 7.16.: *Atlantic zonal mean of potential temperature (top) and salinity (bottom); deviations of run TAU+ from CTRL; integration years 4900 to 4999. Contour interval is 0.2°C for temperature; 0.1 psu for salinity, between -0.1 and 0.1 psu it is 0.02 psu.*

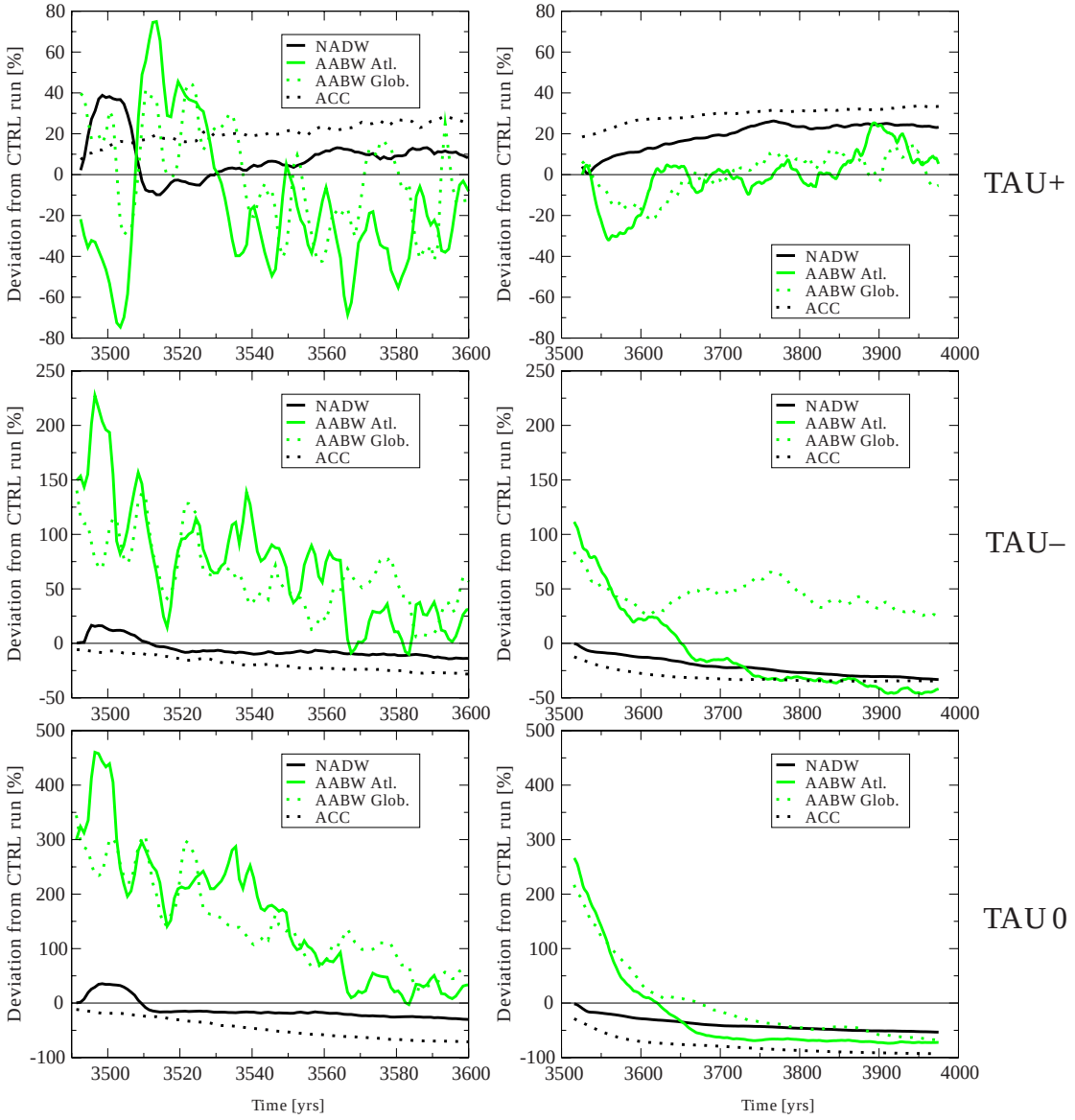

Figure 7.17.: *Temporal evolution of deviations from CTRL in % for NADW (solid black), ACC (dotted black), Atlantic (solid grey) and global AABW (dotted grey). NADW, ACC and (Atlantic) AABW are defined as in Table 7.1; global AABW: amount of the minimum of the global overturning streamfunction below 300 m depth. Top: TAU+; middle: TAU–; bottom: TAU 0. Left: annual means for the first 110 years after introduction of the anomalies; right: 50 years running averages for the integration years 3490 to 4000; scales are different between the plots.*

The temporal evolution of the characteristic quantities as used in the analyses of the buoyancy experiments is displayed in Fig. 7.17. The upper panels show the results for run TAU+. The strong NADW cell close to the Greenland-Scotland-Ridge (that could be seen in the overturning of year 10 after the wind stress was intensified) can be identi-

fied clearly in the black NADW line in the top left graph of Fig. 7.17. This signal lasts only for about 10 to 15 years before it vanishes completely. After some years of weaker overturning the NADW cell develops continuously until it reaches a steady strength after approximately 300 years. The Atlantic AABW cell exhibits a contrary behavior during the first years with an pronounced weakening that is recovered 15 years after the onset of the disturbances and followed by a positive peak of about the same strength. Its further development is dominated by multidecadal oscillations, as is the global AABW signal. The ACC shows a gradual and steady increase in its strength. The graphs for TAU– (middle panels of Fig. 7.17) do not exhibit a mirror image to those of TAU+ as could be expected from the quasi-linear behavior explained before. The NADW cell's first reaction is very similar to TAU+, with a positive anomaly lasting for about 20 years, but with only half of the amplitude (note the ordinates' differing scales). Later, the NADW strength continuously decreases over the following 1500 years. Both AABW cells show a fast amplifying reaction with a slow subsequent decline. The ACC is the only quantity of run TAU– corresponding to the "linear expectation", i.e. its temporal evolution is that of the TAU+ case with reversed sign; it exhibits a continuously decreasing strength. For the experiment with the wind stress switched off over the Southern Ocean (bottom panel of Fig. 7.17) all deep water cells show an increase within the first few years. The temporal evolution as well as the amplitude of the NADW signal are very similar to those of run TAU+. After this positive phase has passed, the maxima of the NADW and AABW cells decrease steadily. It is obvious that the strong oscillations superimposed onto the AABW signals that are observed in all LAB and WED experiments and also in the the TAU+ case vanish after a transient phase in run TAU 0. For run TAU– the intensity of the oscillations is weakened.

A number of different processes influences the ocean's reaction to an altered wind stress over the Southern Ocean. In their theory JOHNSON AND BRYDEN (1989) proposed that the Drake Passage transport is proportional to the square root of the zonal wind stress for latitudinally constant wind stress. Otherwise they found the transport to be proportional to the square root of the average meridional Ekman transport at the latitude of the Drake Passage. In the present investigation aspects of the relationship between the Drake Passage transport and the magnitude of the wind stress amplification, have been called "quasi-linear". The interdependence between the two is surely not that simple, nor does the JOHNSON AND BRYDEN (1989) concept fit the model results. A monotonic but not linear relationship between the two quantities as has been confirmed recently by GENT ET AL. (2001) with a set of twelve experiments with two coarse resolution OGCMs seems to be more appropriate. However, the results of the present model runs do not allow a final judgment on this question. A more detailed discussion of this subject is beyond the scope of this work, anyway.

Long and short time scales in the models reaction to the wind stress alterations can be distinguished. The long term reaction of the North Atlantic deep water production can be explained by the "Drake Passage effect". In run TAU+ stronger winds lead to an enhanced northward Ekman drift and stronger upwelling in the latitude of the Drake

Passage (as can be deduced from the intensified Deacon cell). The water mass transport out of the Southern Ocean into lower latitudes is increased. In the Atlantic these water masses are transported across the equator into the region of the Gulf Stream and the North Atlantic Current until they reach the deep water production regions. There, they contribute to an intensified sinking. For TAU– this mechanism works with reversed signs, thus being the basis of the quasi-linear part of the relationship outlined before.

The "Drake Passage effect" is of advective nature, so its time scales are multidecadal to centennial. The changes in the upwelling alter the density structure, especially the density gradient across the ACC, immediately. This explains the fast changes in the strength of the ACC. The fact that its magnitude continues to increase slowly over hundreds of years in run TAU+ can be regarded as a further proof that the Circumpolar Current is not primarily driven by direct vertical momentum transfer from the atmosphere to the ocean. A direct momentum input from the wind stress would have an instantaneous effect and change velocities and mass transport rapidly. Instead, the mechanism works indirectly via changes of the water mass properties in the deep Southern Ocean (thus being consistent with the findings of GNANADESIKAN AND HALLBERG (2000) and BOROWSKI ET AL. (2001) as outlined in the footnote on page 52).

There is also an even longer time scale present in the results of the TAU experiments. It mainly influences the AABW values after the changes associated with the "Drake Passage effect" have led to new stable conditions in the magnitudes of NADW and ACC. The AABW cell does not reach a new equilibrium within 1500 years after the changes were applied. There is still a trend that can be explained by the global nature of the adjustment processes in the deep ocean. With new boundary conditions the model needs to adapt to a new equilibrium; it took the control run more than 3000 years to reach such an equilibrium state. It is not surprising, thus, that these adjustments are still to be completed after 1500 years for these strong changes in the model's boundary conditions.

Besides the centennial and millenial time scales the model results also exhibit variability with higher frequencies. These are most prominent in the oscillations that are superimposed on the AABW curves. The single NADW events that are present in all three wind stress runs shortly after the disturbances have been introduced into the model cannot be explained by advective processes. In this context, the theory of the "Drake Passage effect" by TOGGWEILER AND SAMUELS (1993a, 1995) can account only for a part of the results obtained here. Even if one were to accept that water parcels can reach the northern hemisphere's deep water production regions that are 8,000 to 10,000 km away within 3 or 4 years, there would still be no explanation for the identical sign of the anomalies in all three cases. The solution must therefore be attributed to a wave signal triggered by the "shock" of an abrupt change of the windstress magnitude causing a remote change of the local stratification in the Northern Atlantic's deep water production regions.

There are a number of uncertainties and limitations concerning the "Drake Passage effect" that should be kept in mind when transferring model results to reality: the Deacon cell, for instance, is only present in a global streamfunction integrated zonally along

depth levels. DÖÖS AND WEBB (1994) pointed out that this cell virtually disappears if the integration is performed along density layers. They found in their model study that there is no mass transport across isopycnals associated with the Deacon cell. Furthermore, it can be doubted that the "Drake Passage effect" is robust at higher resolutions than the one used here; studies with high resolution models for the Southern Ocean (D. OLBERS, personal communication) showed that the residual of the Deacon cell is very shallow (a few hundred meters) when including the effects of eddy mixing. Moreover, a more realistic topography than the one used here would allow a southward return flow at shallower depths eroding the constraint that the sinking of the water masses transported northward is only possible in the northern North Atlantic. Besides that, the prohibition of any *net* geostrophically balanced flow across the latitude band of the Drake Passage holds only for the zonal mean. There may well be bi-directional basin-scale geostrophic flows and small scale eddies. It should be remembered also that in the present study no atmospheric feedbacks exist that would weaken the control that the "Drake Passage effect" exerts on the NADW according to RAHMSTORF AND ENGLAND (1997).

7.3. Common Processes and Differences

The general picture that can be developed from the results of the buoyancy experiments is the following: disturbances introduced in the source regions of deep water formation can have a direct influence on the strength of the associated meridional overturning cells. Thereby, they alter deep and abyssal water mass characteristics by introducing water from a different environment. Advective processes act to transport the changed properties to distant regions. In the deep basins of the Southern Ocean meridional density gradients are the driving force for the ACC. Changing these gradients leads to different equilibria, i.e. different water mass transports around Antarctica. For a positive salinity anomaly in the Labrador Sea the intensified NADW production causes a decreased meridional density gradient in the Southern Ocean and thus weakens the ACC. The situation is different for the positive Weddell Sea anomaly. Here the density gradient and the ACC strength increase. As the Weddell Sea is closer to the latitude of the Drake Passage throughflow the reaction takes place faster and its amplitudes are bigger. The connection between strengthened NADW production and a weaker ACC and vice versa as present in the LAB and WED runs is in accordance with the model results of MIKOLAJEWICZ AND MAIER-REIMER (1990), who find a negative correlation between the two quantities. ENGLAND (1993) attributes this interplay to adjustments in the deep density field on either side of the Drake Passage. However, when comparing results of different model runs one should be aware of the mechanisms causing these changes. HIRST AND CAI (1994) and CAI AND BAINES (1996) report increases in both NADW and ACC strengths when manipulating the vertical diffusivities in their experiments.

From the point of view of interhemispheric interactions, there are more differences than those explained before between the two sets of buoyancy experiments. The LAB

experiments show a distinct influence on the southern hemisphere, even for the LAB–– run in which deep convection was not slowed down directly. This is due to the direct export of subducted water masses into the South Atlantic and their subsequent incorporation into the global water cycle. For the WED runs the situation is different. AABW is, at least in part, exported across the equator, but it recirculates without intense effects onto the circulation or water mass properties of the northern hemisphere. The surface layers north of 30°S are hardly affected in the WED experiments at all, nor is the NADW cell. The interplay of NADW and AABW is surely not a linear one in the sense, that an intensification of one leads to a weakening of the other and vice versa. This connection could have been suspected from values for NADW and AABW in Table 7.1 for the buoyancy experiments. This "seesawing" behavior of deep water production as proposed by STOCKER (1998) and BROECKER ET AL. (1999) and confirmed by the findings of FIEG AND GERDES (2001) in their model studies has been described in section 2.7. There are a number of details of the model results that contradict this simple assumption. First, the cells evolve with different speeds. The NADW cell adjusts to a new equilibrium within about 500 years, while the AABW cell needs longer than the integration time performed here. Second, in the global zonal average the AABW cell behaves in a different way than in the Atlantic average. In the LAB++ run, for instance, the global cell intensifies, while the Atlantic part weakens. Reducing this reflection to the Atlantic AABW branch (as has been done in Table 7.1), the postulated relation of positive NADW anomalies taking place together with negative AABW and vice versa is only true after long integration times. In the LAB runs, there are extended phases of anomalies sharing the same sign. Third, the TAU runs show no relationship of the suspected kind at all.

A possible mechanism for an interaction between NADW and AABW could involve the ACC. It has been demonstrated that changes in the deep water production rate of both cells alter the water mass transport of the ACC. On the other hand, it is difficult to detect an influence of the ACC onto NADW and AABW. However, an altered ACC will definitely influence its surroundings, e.g. by intensifying or weakening of the adjacent Ross and Weddell Sea gyres (compare Fig. 7.5 for the LAB++ case). A strengthening of the cyclonic Weddell Sea gyre, for instance, would lead to an elevation of the pycnocline, thus preconditioning the region for convection (following the argumentation of MARSHALL AND SCHOTT, 1999). Hence, an influence of the NADW cell via the ACC on the AABW cell appears to be possible. A similar conclusion has been drawn by GOODMAN (1998), who performed experiments with an OGCM with idealized ocean basins. For his run with an existing NADW cell he finds, that the AABW production does not depend on the NADW production. The strength of the AABW formation and the northward flow of bottom water is, however, affected by the transport in the ACC in his experiment. To what extent these conclusions reflect reality cannot be said from the results of the model runs performed here. The deep water production is parameterized in the model. In this respect the real process and the modeled process are very different. The model does not resolve the Antarctic shelf that is very important for the convective process. Therefore, this model does not permit a detailed conclusion on the nature of this

specific feature, the interrelation of the ACC's magnitude and deep water formation in the southern hemisphere. Nevertheless, the possibility exists that the proposed mechanism is at work in reality.

Not every feature of the model results can be explained in the framework of advection of water masses. Especially the oscillations that are present in the time series of both AABW values point to another way of signal transmission. Both, the Atlantic portion of the AABW and the global zonally averaged cell show a high variability on different time scales pointing to a variety of processes that influence this cell. It seems plausible to suspect that the observed oscillations are part of an internal variability of the model's system. In fact, the period of the oscillation in the control run as described in chapter 6 can be detected in the AABW time series of the buoyancy and wind stress experiments. To avoid superpositions due to additionally triggered phenomena in the sensitivity experiments future investigations of the prominent frequencies – which appear to be a promising approach – should concentrate on the absolute values of these quantities instead of the differences to the control run analyzed in this chapter.

8. Summary and Conclusions

The present study aimed at understanding the natural variability of the climate system, interactions between its components and the way they exchange information. Only a profound knowledge of these mechanisms allows to evaluate the modifications of the present climate state known as global change. In the long run this can help to predict the system's future developments. In the present work a coupled ocean-sea ice-model is used to investigate the variability and interactions of water masses. The study concentrates on the Atlantic Ocean, its thermohaline circulation and the role of the Southern Ocean as the link of the former to the other ocean basins.

The ocean model used here is a global three-dimensional general circulation model based on the primitive equations of thermo- and hydrodynamics (MOM-2 developed at the GFDL; PACANOWSKI, 1995). It is coupled to a dynamic-thermodynamic sea ice model with a viscous-plastic rheology (HARDER, 1996; HARDER ET AL., 1998). For use in this investigation its code has been modified for a global setup with cyclic boundary conditions. The present model configuration with $4° \times 3°$ resolution resolves the central processes involved in the global redistribution of water masses and allows to account for mechanisms influencing the nature and stability of the thermohaline circulation. The model is forced by an annually repeating cycle of monthly means of atmospheric quantities (wind stress, temperatures and others) obtained from climatological data sets. The model's sea surface salinity is restored to climatological values.

The model integrations reproduce important features of today's global ocean state. Its surface circulation patterns resemble the main circulation systems (e.g. SCHMITZ, 1996). Most of the upwelling areas at the eastern boundaries are reproduced properly. Deep water production takes place in the Irminger and Greenland Sea, as well as in the Weddell and Ross Sea. The NADW cell is reproduced properly with its maximum strength lying in the upper range of other model results. The Atlantic part of the AABW overturning cell is relatively weak. The Atlantic basin shows too high temperatures at intermediate depths and is too cold in the abyssal levels. Compared to observations salinity is overestimated in the entire basin. Owing to the model's coarse resolution the circulation in the Arctic cannot be reproduced. Around Antarctica surface salinities are overestimated. The water mass transport of the ACC is too high. These deficiencies are common in similar models (ENGLAND, 1993; HIRST AND CAI, 1994; CAI AND BAINES, 1996). Despite these shortcomings the overall structure of the ocean's present state is met. As the emphasis of this study is laid on variability of the large scale circulation an exact match with obser-

vational quantities is regarded to be of less importance. It should be kept in mind that this model configuration is a substantial improvement compared to zonally averaged two-dimensional models. It still allows to realize numerous runs within reasonable time, while accounting e.g. for regional features and the investigation of wave propagation.

When addressing variability a distinction can be made between internal processes and the system's reaction to external changes, that is alterations in its boundary conditions. Statistical analyses served to investigate the former. A set of experiments manipulating the ocean's wind and thermohaline forcing was used to study the latter. The results of both can be categorized by the affected time scales: remote processes on interannual to interdecadal scales are mainly triggered by wave propagation, while long-term variability involves advective processes and slow reorganization of water mass properties. The way in which the ocean transmits information depends on the nature of perturbations as well as on the location of their occurrence.

Changes that involve the abyssal ocean and its hydrographic properties can take far more than thousand years as the ocean needs to adapt to a new equilibrium state. This can be seen for example from the results of the model runs with altered wind stress forcing. A strengthened wind stress field over the Southern Ocean leads to increased upwelling due to stronger Ekman pumping. This causes a stronger northward transport of Atlantic surface waters. In the Northern Atlantic Ocean they sink and are transported southward at depth. This mechanism thus causes changes in the strength of the NADW cell that in turn influence the magnitude of the ACC's water mass transport. This mechanism is known as the "Drake Passage effect" (TOGGWEILER AND SAMUELS, 1993a, 1995). The adjustment of the abyssal ocean associated with this mechanism was not completed within the 1500 years of integration in this model run.

The studies performed here show remote effects of the key quantities influencing the Atlantic Ocean: an altered NADW production leads to a transport of water masses with characteristics differing from those of the location they are transported to. Thereby, not only the AABW is affected locally in the North Atlantic Ocean but also the meridional density gradients in the Southern Ocean are changed. This in turn has an effect on the strength of the ACC. The experiments in which buoyancy forcing is manipulated show the common feature that a strengthening of the NADW cell is associated with a weakening of the water mass transport in the ACC. This is due to the altered water mass structure in the deep ocean causing a weakening of the meridional density gradients in the Southern Ocean. There are hints for a connection between the ACC strength and the AABW formation rate, that involves a change in the gyre systems south of the ACC. It should be emphasized, that the interaction between the components of the circulation system is not a mechanistic one. An intensification of the NADW cell does not automatically cause a weakening of the AABW cell, as could have been suspected from the results of previous studies (STOCKER, 1998; BROECKER ET AL., 1999; FIEG AND GERDES, 2001). For example, in the model runs with altered wind stress the long term reaction of the NADW and AABW cells contradicts the behavior found in the studies cited before. Both

cells show common strengthening (weakening) for intensified (decreased) wind stresses. Thus, a distinction must be made concerning the nature of perturbations: altered wind stress forcing in the Southern Ocean influences both Atlantic overturning cells directly via a change in the surface circulation patterns and their strength. Buoyancy forcing changes in the present experiments influence deep water production rates of one hemisphere leading to altered water mass properties in the interior of the oceans, that in turn exert an (indirect) effect on the overturning cell of the other hemisphere.

In the model run without wind stress over the Southern Ocean an almost complete cessation of the ACC was found. This contradicts the results of CAI AND BAINES (1996). As the strength of the water mass transport in the ACC is subject to a slow gradual decrease after turning off the forcing, the integration of this experiment needs to be continued for more than thousand years, even if the deep ocean's global mean water mass properties (used as criterion for a new equilibrium by CAI AND BAINES, 1996) only show minor changes.

Short-term variability has been addressed in this study by analyzing the results of the control integration with statistical techniques. A number of quantities in the Southern Ocean (e.g. Drake Passage throughflow, Weddell Sea ice thickness and others) revealed a distinct internal decadal oscillation. Its frequency could be also be found in the deep ocean. A series of Rossby and Kelvin waves gives a plausible explanation for the northward transport of anomalies of this time scale. To get a more detailed picture of the nature of their pathways and to separate advective signals from wave propagation further experiments are necessary. A promising approach is the introduction of a disturbance pulsed with the frequency of the internal oscillation into the model's the southern hemisphere. The wind stress experiments show a very fast reaction (within less than ten years) in the strength of the NADW cell after the anomalies have been applied. Surely, these fast reactions cannot be explained in the framework of the "Drake Passage effect" theory which attributes circulation changes to the advection of water masses. They rather have to be due to local stratification changes in the North Atlantic triggered by the abrupt change of the wind stress field over the Southern Ocean. It can be speculated that the pathway described for the internal oscillation could also be a realistic one for the transmission of information about changes in the wind stress field into the North Atlantic.

Despite the insights gained from analyzing the results of the model runs, there are a number of remaining questions: why does the NADW cell's fast reaction show the same sign for positive as well as for negative wind stress anomalies? What causes the global and the Atlantic AABW cell to be out of phase in most of the experiments? What is the role other ocean basins in this context? What causes the detected internal oscillation and could it possibly be an model artifact?

To address these questions in future investigations the shortcomings of the present model results have to be taken into account. Part of them is associated with the coarse horizontal resolution. The almost complete absence of shelf regions especially in the high latitudes of both hemispheres leads to an unrealistic representation of the deep

water formation processes. In the North Atlantic Ocean a more detailed simulation of overflow processes at the Greenland-Scotland-Ridge is desirable. In the Southern Ocean there is no observational proof for the convective activities east of the Greenwich meridian and north of 60°S that were found in the model. These may thus be a model artifact. Furthermore, the representation of the deep western boundary currents is dissatisfying and could be improved using a higher resolution. This would also allow a more realistic reproduction of the circulation in the Arctic Ocean. On the other hand the strongly increased amount of computational resources required by a model of higher resolution limits the number of experiments that could be performed. A reasonable improvement would be the use of more sophisticated parameterizations (like the mixing scheme of GENT AND MCWILLIAMS (1990) that increases the required computer time "only" by about 60% as demonstrated in the sensitivity chapter of this study).

A coupling of the present model to the energy and moisture balance model (EMBM) developed by MEISSNER (1999) has been prepared. This setup will allow to consider atmospheric feedbacks as e.g. those named by RAHMSTORF AND ENGLAND (1997) leading to a weakening of the control the "Drake Passage effect" exerts on NADW formation. In this context it would be relevant to investigate if the instantaneous reaction of the NADW to changes in the wind forcing is influenced by atmospheric feedbacks. Another aspect to be addressed with a model version coupled to an EMBM is the nature of the internal oscillation described here. Restoring is known to exert a damping effect on oscillations. It would therefore be important to see if the oscillation is intensified in the presence of atmospheric feedbacks. A disadvantage of coupling the ocean-sea ice-model to an EMBM will be the higher complexity of interactions. It can be expected that the variety of additional processes that are included then will complicate the detection of single mechanisms.

To concentrate on single aspects detected in this model study the use of models with simple geometries could help clarifying mechanisms. A comparison of the results obtained here in the wind stress experiments with those of a simplified model for the Atlantic basin with a circumpolar channel (D. BOROWSKI, personal communication) appears to be promising. Especially the behavior of the deep water cells could thus be approached more systematically.

A variety of processes and non-linear interactions govern the interplay of the water masses in the Atlantic Ocean. This system cannot be understood if the influence of the ACC is neglected. On one hand the conditions in the Southern Ocean are marked by the influence of the overturning cells on the density structure of the deep ocean and thereby on the strength of the ACC. On the other hand the ACC seems to have a regulating influence on the AABW cell that interacts with the North Atlantic overturning. Furthermore, changes in the oceans of the southern hemisphere can be quickly propagated by waves to the North where they influence the North Atlantic Ocean at least on decadal time scales. The nature of these interactions will remain subject to further investigations, or as Aristotle puts it in his "Meteorologica": *Of these things some puzzle us, while others admit of explanation in some degree.*

Appendix

A. Statistical Tools

The description of statistical methods in this appendix is – with kind permission – mainly taken from KAUKER (1998). Unless other references are given in the text it is based on the publication by VON STORCH AND ZWIERS (1998).

A.1. Empirical Orthogonal Functions

Principal Component Analysis or Empirical Orthogonal Function (EOF) Analysis as it is called in geosciences was introduced into meteorology by LORENZ (1956). Its purpose is to derive dominant patterns of variability from a statistical field, which in practice is equivalent to a data reduction. This is achieved by converting data sets with many degrees of freedom into data sets with less degrees of freedom, while keeping the most of their variability. A key aspect for use in geosciences is that EOFs allow for an analysis of interdependencies within investigated data sets.

A principal component analysis identifies a series of orthogonal patterns $\vec{e}^k$, called the *Empirical Orthogonal Functions (EOFs)*, which for any number K minimize the mean-squared error

$$\sum_t [\vec{X}(t) - \sum_{k=1}^{K} \alpha_k(t)\vec{e}^k]^2, \tag{A.1}$$

where t usually represents time and $\vec{X}$ is a multivariate random vector. Because of the orthogonality of the EOFs, the optimal coefficients $\alpha_k(t)$ are given by the projection of the EOF $\vec{e}^k$ onto the random vector $\vec{X}$:

$$\alpha_k(t) = < \vec{X}(t), \vec{e}^k > . \tag{A.2}$$

These coefficients are called *EOF coefficients,* or *principal components.* They are pairwise uncorrelated.

It can be shown that the EOFs are the eigenvectors of the sample covariance matrix and that the EOF coefficients are statistically independent if the involved distributions are Gaussian.

If the EOFs are normalized, the total variance of the vector time series $\vec{X}$ may be decomposed into independent contributions from the EOFs

$$\sum_t |\vec{X}(t)^2|^2 = \sum_{t,k} \alpha_k(t)^2, \tag{A.3}$$

i.e., the EOFs form a orthogonal basis of the random vector $\vec{X}$.

A.2. Canonical Correlation Analysis

In certain problems, it is useful to identify *pairs* of patterns in two observed or simulated random vectors simultaneously. The *Canonical Correlation Analysis (CCA)* is a technique that is based on optimizing the correlation between patterns (HOTELLING, 1936). The CCA decomposes two random vectors $\vec{X}(t)$ and $\vec{Y}(t)$ ($\vec{X}(t)$ and $\vec{Y}(t)$ are *anomalies*, i.e., the time means have been subtracted prior to the analysis) into K patterns

$$\vec{X}(t) = \sum_{k=1}^{K} \alpha_k(t)\vec{p}_k \tag{A.4}$$

$$\vec{Y}(t) = \sum_{k=1}^{K} \beta_k(t)\vec{q}_k, \tag{A.5}$$

where $\vec{p}_k$ and $\vec{q}_k$ are the kth CCA patterns and $\alpha_k(t)$ and $\beta_k(t)$ are the kth CCA time series. Note that in general $\vec{X}(t)$ and $\vec{Y}(t)$ and therefore $\vec{p}_k(t)$ and $\vec{q}(t)$ have different spatial dimensions. The patterns and time series fulfill the following constraints:

1. The coefficients $\alpha_k(t)$ and $\beta_k(t)$ are *optimal* in the sense that they minimize the equations

$$||\vec{X}(t) - \sum_{k=1}^{K} \alpha_k(t)\vec{p}_k|| \tag{A.6}$$

$$||\vec{Y}(t) - \sum_{k=1}^{K} \beta_k(t)\vec{q}_k||. \tag{A.7}$$

2. The correlations between α_k and α_l, between β_k and β_l, and between α_k and β_l are zero for all $k \neq l$.

3. α_1 and β_1 have the maximal possible correlation.

4. α_2 and β_2 have the next highest correlation by being orthogonal to the former pair, and so on.

An important caveat to keep in mind is the method's intrinsic tendency to return overestimated correlation coefficients from a finite sample. Often a EOF truncation is performed to reduce the dimensionality of the calculation. The results may depend on the EOF truncation of the data.

A.3. Regression Analysis

Regression Analysis is used here to investigate the link between two concurrent events as well as between time-lagged events. The approach used is to calculate a regression for every (spatial) point x_j between a time series $\alpha(t)$ and a random vector $\vec{X}(x,t)$. The analysis aims at determining a time-independent vector $\vec{Y}(x)$ – the *regression coefficient* – under the constraint of minimizing

$$||\vec{X}(x,t) - \alpha(t)\vec{Y}(x)||. \tag{A.8}$$

To calculate lagged regressions the discrete time steps of $\alpha(t)$ and $\vec{X}(x,t)$ are delayed against each other. The correlation coefficient of this regression is determined by:

$$Cor = \frac{\vec{Y}(x)}{\sigma(\vec{X}(x,t))}, \tag{A.9}$$

where $\sigma(\vec{X}(x,t))$ denotes the standard deviation of $\vec{X}(x,t)$.

A.4. Principal Oscillation Patterns

The basic idea is to identify a linear system with a few degrees of freedom from a complex system. Consider a discretized linear system

$$\vec{X}(t+1) = \mathbf{A} \cdot \vec{X}(t) + noise, \tag{A.10}$$

where $\vec{X}$ is a n-dimensional random vector. The system matrix $\mathbf{A}$ is a time-independent $n \times n$ matrix. Multiplication of equation (A.10) from the right-hand side by the transposed of $\vec{X}(t)$ and taking expectations leads to

$$\mathbf{A} = Cov(\vec{X}(t+1), \vec{X}(t)) \cdot Cov^{-1}(\vec{X}(t), \vec{X}(t)), \tag{A.11}$$

i.e., $\mathbf{A}$ is the product of the sample lag+1 covariance matrix and the inverse of the sample covariance.

The eigenvectors $\vec{p}_j$ of $\mathbf{A}$ are called the *Principal Oscillation Patterns (POPs)*. In general, $\mathbf{A}$ is not symmetric, i.e., its eigenvalues λ are complex. The discussion is restricted to the case of complex eigenvalues. If $\mathbf{A}$ is not degenerated, the eigenvectors $\vec{p}_j$ form a linear basis

$$\vec{X}(t) = \sum_j z_j(t) \cdot \vec{p}_j, \tag{A.12}$$

with $z_j(t)$ being the *POP coefficients*. Inserting equation (A.12) into equation (A.10) yields (the index j is omitted)

$$z(t+1) \cdot \vec{p} = \lambda z(t) \cdot \vec{p} + noise, \tag{A.13}$$

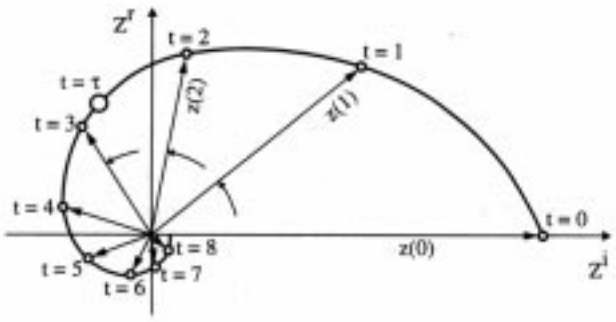

Figure A.1.: *Schematic diagram of the time evolution of POP coefficients $z(t)$ with an initial value $z(0) = (0,1)$. z rotates counter-clockwise in one period T around the origin. The e-folding time τ, for which $z(t) = 1/e$, is marked by an open circle. From* VON STORCH ET AL. *(1990).*

so that, if $z(0) = 1$,

$$z(t) \cdot \vec{p} = \lambda^t \cdot \vec{p} + noise. \tag{A.14}$$

The contribution $\vec{P}(t)$ of the POP $\vec{p}$ to the process $\vec{X}(t)$ is the real part of $z(t) \cdot \vec{p}$

$$\vec{P}(t) = z(t) \cdot \vec{p} + (z(t) \cdot \vec{p})^\star, \tag{A.15}$$

with * representing the complex conjugate operator. Splitting $\vec{p}$ into the real part $\vec{p}^{\,r}$ and imaginary part $\vec{p}^{\,i}$ and writing $2z(t) = z^r(t) - iz^i(t)$ yields (setting $z(0) = 1$)

$$\begin{aligned} \vec{P}(t) &= z(t)^r \cdot \vec{p}^{\,r} + z(t)^i \cdot \vec{p}^{\,i} && \text{(A.16)} \\ &= \rho^t (cos(\eta t) \cdot \vec{p}^{\,r} - sin(\eta t) \cdot \vec{p}^{\,i}), && \text{(A.17)} \end{aligned}$$

with $\lambda = \rho \exp(i\eta)$. The so-called *reconstructed POP* of chapter 6 is the contribution $\vec{P}(t)$ of the first POP, in practice "reconstructed" from the real and imaginary parts of the POP and their coefficients as in equation (A.16).

The geometric meaning of equation (A.17) is a trajectory of a spiral in the space spanned by $\vec{p}^{\,r}$ and $\vec{p}^{\,i}$ (Fig. A.1) with the period $T = 2\pi/\eta$ and the *e-folding time* $\tau = -1/ln(\rho)$. The trajectory passes through $\vec{p}^{\,r}$ and $\vec{p}^{\,i}$ in the consecutive order

$$\ldots \quad \vec{p}^{\,r} \quad \rightarrow \quad -\vec{p}^{\,i} \quad \rightarrow \quad -\vec{p}^{\,r} \quad \rightarrow \quad \vec{p}^{\,i} \quad \rightarrow \quad \vec{p}^{\,r} \quad \ldots \tag{A.18}$$

The e-folding time or *damping time* τ is the time in which the amplitude is damped to $1/e$ th of the initial amplitude.

The pattern coefficients $z_j(t)$ are given as the projection of the random vector $\vec{X}$ onto the *adjoint patterns* $\vec{p}_j^{\,A}$, which are the normalized eigenvectors of the adjoint matrix $\mathbf{A}^A$:

$$z_j(t) = < \vec{p}_j^{\,A}, \vec{X} > = \sum_k z_k(t) (\vec{p}_j^{\,A})^T \vec{p}_k. \tag{A.19}$$

The adjoint patterns can be estimated from the adjoint matrix $\mathbf{A}^A$. This is not always a stable procedure as the eigenvectors $\vec{p}^{\,A}$ of the matrix $\mathbf{A}^A$ have to be orthogonal to the eigenvectors $\vec{p}$, i.e., have to satisfy the constraint $< \vec{p}_i^{\,A}, \vec{p}_j >= \delta_{ij}$. Because some of the POPs represent noise, it is often advisable to estimate the patterns $\vec{p}^{\,A}$ by minimizing

$$||\vec{X} - < \vec{p}^{\,A}, \vec{X} > \vec{p}\,||. \tag{A.20}$$

An alternative is not to derive adjoint patterns but to derive the coefficients z by a least-square fit of the data by minimizing

$$||\vec{X} - z \cdot \vec{p} - (z \cdot \vec{p})^{\star}\,||. \tag{A.21}$$

The auto-spectrum Γ_z of the POP coefficient $z(t)$ is a function the eigenvalue λ and of the auto-spectrum of the noise Γ_n (see equation A.13):

$$\Gamma_z(\omega) = \frac{\Gamma_n(\omega)}{|1 - \rho e^{i(\omega-\eta)}|^2}. \tag{A.22}$$

If the noise spectrum Γ_n is white, the temporal statistics of the signal are determined by the eigenvalue λ. In this case, the width of the spectrum depends only on ρ. The smaller the value of ρ the broader the spectrum. The spectrum has a single maximum, $\Gamma_z = (1-\rho)^{-2}$, at $\omega = \eta$.

B. Philosophical and Historical Aspects

It may seem strange in the context of a geophysical thesis to discus subjects as indicated by the headline of the appendix – nevertheless two arguments convinced me to include this chapter. First, looking for a way to start the introduction of this work I ran into a lot of publications, books, maps and essays covering geographical, philosophical and historical aspects of interhemispheric connections. To me it felt like a waste of time, keeping this information for me. Second, talking to colleagues I noticed astonishment and curiosity everywhere when telling about this aspect of my subject. In a time when the words inter- and multidisciplinary are used almost everywhere, an excursion into humanities at least won't do any harm to natural scientists . . .

As soon as mankind had settled down, started breeding cattle, growing crops and trading with neighbors, there was a need to get some knowledge about geography. In a broader sense than the word is used today, it was part of the myths of the early civilizations settling in Egypt, Mesopotamia, China and elsewhere. Geography first was restricted to the close vicinity of settlements or states and there were only few ideas of how the world "outside" looked like. It is astonishing that in many early cultures the world was seen as a land mass surrounded by the sea. The growing interest in trade and conquests was the motivating force behind travel and explorations. There is evidence that the Phoenicians crossed the Strait of Gibraltar at the beginning of the first millennium B.C. About 600 B.C. the Egyptian king Necho ordered the Phoenicians serving under him to sail around "Libya" (Africa) from east to west. This successful journey that took more than two years was hardly ever mentioned afterwards. Still there was no closed conceptual idea to describe more than single parts of the world.

In the Greek cities in Ionia schools of philosophers started to grow after 600 B.C. Their main achievement was to end the habit of thinking in myths and to begin asking questions on what the world was made of. The common basic assumption was that the universe could be explained and that there is an ultimate "nature" or substance. On this base theories were developed that served to explain the world as a whole. Geography thus became a part of philosophy. This implied that observation (if needed at all) was subordinated to theoretical concepts.

It is not known who was the first to postulate the spheric shape of the earth. Nevertheless, a geocentric picture of a spheric world was common thought within the school of the Pythagoreans (named after Pythagoras of Samos – about 569 to 475 B.C.). As far as

our knowledge of ancient Greek texts is complete, the first to postulate the existence of an inhabitable southern hemisphere was Aristotle (384 to 322 B.C.). He divided the globe into zones and the world into a number of spheres containing the stars, planets, sun, moon and the earth. A central point to his theories was the existence of a "first mover", i.e. a God, who was occupied all the time with keeping the spheres moving. Aristotle's concept was accepted widely in the antique world. For instance in Marcus Tullius Cicero's (106 to 43 B.C.) *Somnium Scipionis (6th book "De res publica")*, the division of the world in habitable and inhabitable zones on a globe is portrayed as a matter of course. It is also reflected by the maps drawn by Claudius Ptolemy (about 87 to 150 A.D.), who adapted the "geographical facts" from Aristotle, but had a more cartographic point of view.

The decline of science that came with the decay of the Roman Empire and the condemnation of parts of astronomy and other "secular wisdom" by the Christian church led to a loss of knowledge that could only be recovered in modern times. The idea of the Earth as a globe survived only in a few copies of the works of Greek philosophers in Arab libraries and to a lesser extent in the libraries of monasteries of the Christian world (where these texts were often misinterpreted, when used at all). That the knowledge of the ancient Greek philosophers was not completely lost in the Middle Ages can be seen for example from the *Divine Comedy* by Dante Alighieri (1265 to 1321 A.D.), who let Odysseus sail into the southern hemisphere in the 26th verse of his *Inferno*.

At the end of the Middle Ages the works of Ptolemy and Aristotle reentered the European cultures. Geography to that time was subordinated to theology. Aristotle's concept of a God acting all the time was the reason why he became so popular during the reformation. Luther introduced a "close" God, who is always around in contradiction to the "distant" God perception of the Catholic church. There, God is regarded as the Creator, who can leave the world to its own for some time. According to this way of interpreting theological questions, geography in Catholic countries based on the works of Ptolemy, while the Protestant world mainly interpreted Aristotle's writings. Columbus' (with order of the "Reyes Catolicos") effort to sail west to seek Asia can be regarded as an indirect effect of Ptolemy's mistake of over-stretching the Old World round the globe. The existence of a great unknown southern continent also mapped by Ptolemy took centuries of exploring until in the late 18th century it turned out to be not the kind of place predicted by Aristotle.

For further reading on this subject – besides the "classic" works of Aristotle, Cicero and Dante mentioned here – the books by THOMSON (1948) and BÜTTNER (1979) may be recommended.

Notations and Abbreviations

a: Mean Earth's radius

A_I: Ice concentration (areal coverage) – as used in the ice model

A_I: Isopycnal mixing coefficient – as used in the ocean model

A_h, A_m: Horizontal eddy diffusivity and viscosity coefficient

C: Ice concentration parameter

c_w: Oceanic drag coefficient (see Table 3.3)

c_{dbot}: Bottom drag coefficient

E_{kin}: Total kinetic energy per unit volume

f: Coriolis parameter ($f = 2\Omega \sin \phi$)

$\mathbf{F}$: Internal ice forces

F^u, F^v: Horizontal terms including friction and diffusion

g: Gravitational acceleration ($g = 9.8\ \mathrm{m\,s^{-2}}$)

$\tilde{G}$: Nonlinear and dissipation terms

G_h: Freezing rate ($G_h = \max(S_h, 0)$)

H: Depth between ocean surface and bottom

h_I: Ice thickness

h_s: Snow thickness

h_0: Lead closing parameter

$\mathbf{k}$: Vertical unit vector

L_I: Specific latent heat (melt energy) of sea ice (see Table 3.3)

m: Ice mass per area

M_h: Melting rate ($M_h = \min(S_h, 0)$)

p, P: Pressure

P_p: Ice strength

P^*: Ice strength parameter

Q_a, Q_o: Net heat fluxes from atmosphere and ocean

Q_c: Conductive heat flux

S: Salinity

S_h, S_A, S_s: Thermodynamic source and sink terms

t: Time

T: Potential temperature

$\mathbf{u} = (u, v, w)$: Longitudinal, latitudinal, and vertical velocity components

$\mathbf{u}_h = (u, v)$: Horizontal velocity

$\overline{u}, \overline{v}$: External, barotropic mode of u, v

$\hat{u}, \hat{v}$: Internal, baroclinic mode of u, v

$\mathbf{u}_{\parallel}, \mathbf{u}_{\perp}$: Horizontal velocity parallel to and velocity perpendicular to the lateral boundaries

$\mathbf{u}_I, \mathbf{u}_w$: Ice drift and ocean velocity

V: Ocean volume

z: Height / depth relative to mean Earth's radius a

δ_{ij}: Kronecker symbol — $\delta_{ij} = \begin{cases} 1 & \forall \quad i = j \\ 0 & \forall \quad i \neq j \end{cases}$

Δ: Total deformation of ice cover

Δ_{min}: Regime parameter

Δt_{rS}: Restoring time constant

Δz: Layer thickness

ϵ: Eccentricity of the yield curve

ε: Ice deformation tensor

$\dot{\varepsilon}$: Ice deformation rate tensor

ζ: bulk viscosity

η: shear viscosity

Θ: Deflection angle between ocean drag and velocity

κ_h, κ_m: Vertical eddy diffusivity and vicosity coefficient

λ, ϕ: Longitude, latitude

ρ, ρ_0: Density, reference density

ρ_I, ρ_s, ρ_w: Density of sea ice, snow and water

σ: Ice stress tensor

τ_a, τ_w: Atmospheric and oceanic drag

τ_{bot}: Bottom drag

Ψ: Streamfunction

Ω: Earth's angular velocity ($\Omega = \frac{\pi}{43082} \text{sec}^{-1}$)

L: Advection Operator

AABW: Antarctic Bottom Water
AAIW: Antarctic Intermediate Water
ACC: Antarctic Circumpolar Current
ACW: Antarctic Circumpolar Wave
CCA: Canonical Correlation Analysis
CFC: Chlorofluorocarbon
CFL: Courant-Friedrichs-Lewy Constraint
DWBC: Deep Western Boundary Current
ECMWF: European Center for Medium-Range Weather Forecasts
EOF: Empirical Orthogonal Function
ENSO: El Niño / Southern Oscillation
FCT: Flux-Corrected Transport (Advection Scheme)
GCM: General Circulation Model
GFDL: Geophysical Fluid Dynamics Laboratory
GSA: Great Salinity Anomaly
IPCC: Intergovernmental Panel on Climate Change
LGM: Last Glacial Maximum
LNADW: Lower North Atlantic Deep Water
MOC: Meridional Overturning Circulation
MOM: Modular Ocean Model
NAC: North Atlantic Current
NAO: North Atlantic Oscillation
NADW: North Atlantic Deep Water
NOAA: National Oceanic and Atmospheric Administration
OGCM: Ocean General Circulation Model
POP: Principal Oscillation Pattern
SLP: Sea Level Pressure
SSM / I: Special Sensor Microwave / Imager
SSS, SST: Sea Surface Salinity, Sea Surface Temperature
THC: Thermohaline Circulation
UNADW: Upper North Atlantic Deep Water

Bibliography

AAGAARD, K. and E. CARMACK, 1989: The role of sea ice and other fresh water in the Arctic circulation, *J. Geophys. Res.*, **94** (C10), 14,485–14,498.

AAGAARD, K., J. SWIFT and E. CARMACK, 1985: Thermohaline circulation in the Arctic Mediterranean Seas, *J. Geophys. Res.*, **90** (C3), 4833–4846.

BEAGLEHOLE, J., ed., 1955: *The Journals of Captain James Cook on his Voyages of Discovery. Volume I: The Voyage of the "Endeavour" 1768-1771*, Cambridge University Press for the Hakluyt Society, 684 pp.

BELKIN, I., S. LEVITUS, J. ANTONOV and S.-A. MALMBERG, 1998: "Great Salinity Anomalies" in the North Atlantic, *Progress in Oceanography*, **41**, 1–68.

BJÖRCK, S., B. KROMER, S. JOHNSEN, O. BENNIKE, D. HAMMARLUND, G. LEMDAHL, G. POSSNERT, T. RASMUSSEN, B. WOHLFARTH, C. HAMMER and M. SPURK, 1996: Synchronized terrestrial atmospheric deglacial records around the North Atlantic, *Science*, **274**, 1155–1160.

BLUNIER, T. and E. BROOK, 2001: Timing of millennial-scale climate change in Antarctica and Greenland during the last glacial period, *Science*, **291**, 109–112.

BOND, G., W. SHOWERS, M. ELLIOT, M. EVANS, R. LOTTI, I. HAJDAS, G. BONANI and S. JOHNSON, 1999: The North Atlantic's 1-2 kyr climate rhythm: Relation to Heinrich events, Dansgaard / Oeschger cycles and the little ice age, in *Mechanisms of Global Climate Change at Millennial Time Scales*, P. Clark, R. Webb and L. Keigwin, eds., vol. 112 of *Geophysical Monograph Series*, pp. 35–58, American Geophysical Union, Washington, D.C.

BORIS, J. P. and D. L. BOOK, 1973: Flux-corrected transport, I. SHASTA: A fluid transport algorithm that works, *J. Phys. Chem.*, **11**, 38–69.

BOROWSKI, D., R. GERDES and D. OLBERS, 2001: Thermohaline and wind forcing of a circumpolar channel with blocked geostrophic contours, *in preparation*.

BOVILLE, B. and P. GENT, 1998: The NCAR Climate System Model, Version One, *J. Climate*, **11**, 1115–1130.

BOYLE, E., 1995: Last-Glacial-Maximum North Atlantic Deep Water: on, off or somewhere in-between? (Discussion held 21-22 September 1994, Royal Society, London), in *The role of the North Atlantic in the global carbon cycle.*, G. Eglington, et.al., ed., Philosophical Transactions of the Royal Society B, 348, pp. 243–253, Royal Society, London.

BROECKER, W., 1987: The biggest chill, *Nat. Hist. Mag.*, **97**, 74–82.

BROECKER, W., 1991: The great ocean conveyor, *Oceanography*, **4**, 79–89.

BROECKER, W., 1998: Paleocean circulation during the last deglaciation: A bipolar seesaw, *Paleoceanography*, **13**, 119–121.

BROECKER, W. and G. DENTON, 1989: The role of ocean-atmosphere reorganizations in glacial cycles, *Geochimica et Cosmochimica Acta*, **53**, 2465–2501.

BROECKER, W., S. SUTHERLAND and T.-H. PENG, 1999: A possible 20th-century slowdown of Southern Ocean deep water formation, *Science*, **286**, 1132–1135.

BROECKER, W. S., 1990: Salinity history of the Northern Atlantic during the last deglaciation, *Paleoceanography*, **5**, 459–467.

BRYAN, F., 1987: Parameter sensitivity of primitive equation ocean general circulation models, *J. Phys. Oceanogr.*, **17**, 970–985.

BRYAN, K., 1969: A numerical method for the study of the circulation of the world ocean, *J. Comput. Phys.*, **4**, 347 – 376.

BRYAN, K., 1984: Accelerating the convergence to equilibrium of ocean-climate models, *J. Phys. Oceanogr.*, **14**, 666–673.

BÜTTNER, M., ed., 1979: *Wandlungen in geographischen Denken von Aristoteles bis Kant*, Ferdinand Schöningh, Paderborn, Germany, 276 pp.

CAI, W. and P. BAINES, 1996: Interactions between thermohaline and wind-driven circulations and their relevance to the dynamics of the Antarctic Circumpolar Current, in a coarse resolution global OGCM, *J. Geophys. Res.*, **101** (C6), 14,073–14,093.

CARMACK, E., 1986: Circulation and mixing in ice-covered waters, in *The Geophysics of Sea Ice*, N. Untersteiner, ed., vol. 146 of *NATO ASI Series B*, pp. 641–712, Plenum Press, New York, London.

CAVALIERI, D., P. GLOERSEN, C. PARKINSON, J. COMISO and H. ZWALLY, 1997: Observed hemispheric asymmetry in global sea ice changes, *Science*, **278**, 1104–1106.

CLARKE, G., S. MARSHALL, C. HILLAIRE-MARCEL, G. BILODEAU and C. VEIGA-PIRES, 1999: A glaciological perspective on Heinrich events, in *Mechanisms of Global Climate Change at Millennial Time Scales*, P. Clark, R. Webb and L. Keigwin, eds., vol. 112 of *Geophysical Monograph Series*, pp. 243–262, American Geophysical Union, Washington, D.C.

COLES, V., M. MCCARTNEY, D. OLSEN and W. SMETHIE, 1996: Changes in Antarctic bottom water properties in the western South Atlantic in the late 1980s, *J. Geophys. Res.*, **101** (C4), 8957–8970.

COX, M., 1989: An idealized model of the world ocean. Part I: The global-scale water masses, *J. Phys. Oceanogr.*, **19**, 1730–1752.

COX, M. D., 1984: A primitive equation 3–dimensional model of the ocean, Technical report no. 1, GFDL Ocean Group, Princeton.

COX, M. D., 1987: Isopycnal diffusion in a z-coordinate ocean model, *Ocean Modelling*, **74**, 1–5.

CROWLEY, T., 1992: North Atlantic deep water cools the southern hemisphere, *Paleoceanography*, **7** (4), 489–497.

CURRY, J. and P. WEBSTER, 1999: *Thermodynamics of Atmospheres and Oceans*, vol. 65 of *International Geophysics Series*, Academic Press, San Diego, 467 pp.

DANABASOGLU, G. and J. MCWILLIAMS, 1995: Sensitivity of the global ocean circulation to parameterizations of mesoscale tracer transports, *J. Climate*, **8**, 2967–2987.

DICKSON, R., 1997: From the Labrador Sea to global change, *Nature*, **386**, 649–650.

DICKSON, R. and J. BROWN, 1994: The production of North Atlantic Deep Water: Sources, rates, and pathways, *J. Geophys. Res.*, **99** (C6), 12,319–12,341.

DICKSON, R., J. MEINCKE, S.-A. MALMBERG and A. LEE, 1988: The "Great Salinity Anomaly" in the northern North Atlantic, *Progress in Oceanography*, **20**, 103–151.

DICKSON, R., T. OSBORN, J. HURRELL, J. MEINCKE, J. BLINDHEIM, B. ADLANDSVIK, T. VINJE, G. ALEKSEEV and W. MASLOWSKI, 2000: The Arctic Ocean response to the North Atlantic Oscillation, *J. Climate*, **13**, 2671–2696.

DIETRICH, G., K. KALLE, W. KRAUSS and G. SIEDLER, 1975: *Allgemeine Meereskunde*, Gebrüder Borntraeger, Berlin, Stuttgart, 3rd edn., 593 pp.

DÖÖS, K. and D. WEBB, 1994: The Deacon cell and the other meridional cells of the Southern Ocean, *J. Phys. Oceanogr.*, **24**, 429–442.

DUPLESSY, J. and N. SHACKLETON, 1985: Response of global deep-water circulation to earth's climate change, *Nature*, **316**, 500–507.

ECMWF, 1993: The description of the ECMWF/WCRP level III – A global atmospheric data archive., Tech. rep., ECWMF, 48 pp.

ENGLAND, M., 1993: Representing the global-scale water masses in ocean general circulation models, *J. Phys. Oceanogr.*, **23**, 1523–1552.

ENGLAND, M., J. GODFREY, A. HIRST and M. TOMCZAK, 1993: The mechanism for Antarctic Intermediate Water renewal in a World Ocean model, *J. Phys. Oceanogr.*, **23**, 1553–1560.

FAHRBACH, E., M. SCHRÖDER and A. KLEPIKOV, 1998: Circulation and water masses in the Weddell Sea, in *Physics of Ice-Covered Seas*, Lecture notes from a summer school in Savonlinna Finland, Helsinki University Press.

FIEG, K., 1996: The ocean as a part of the coupled climate system: an attempt to reconstruct the glacial circulation with different models of the atmosphere, *Alfred-Wegener-Institut für Polar- und Meeresforschung, Bremerhaven, Germany, Reports on Polar Research*, **206**, 128pp.

FIEG, K. and R. GERDES, 2001: Sensitivity of the thermohaline circulation to modern and glacial surface boundary conditions, *J. Geophys. Res.*, **106** (C4), 6853–6867.

FISCHER, H., 1995: Comparison of an optimized dynamic-thermodynamic sea ice model with observations in the Weddell Sea, *Alfred-Wegener-Institut für Polar- und Meeresforschung, Bremerhaven, Germany, Reports on Polar Research*, **166**, 130pp.

FOLLAND, C., T. PALMER and D. PARKER, 1986: Sahel rainfall and worldwide sea temperatures, 1901 - 1985, *Nature*, **320**, 602–607.

FRITZSCH, B., R. GERDES, W. HILLER, M. LATIF, S. LEGUTKE, E. MAIER-REIMER, D. OLBERS and F. ROESKE, 2000: Vergleich der thermohalinen Zirkulation in zwei globalen ozeanischen Zirkulationsmodellen, Abschlußbericht BMBF Projekt 01 LA 9862 / 8, OMIP (The German Ocean Model Intercomparison Project Group): Alfred Wegener Institute for Polar and Marine Research, Bremerhaven; Max-Planck-Institute for Meteorology, Hamburg.

GANACHAUD, A. and C. WUNSCH, 2000: Improved estimates of global ocean circulation, heat transport and mixing from hydrographic data, *Nature*, **408**, 453–457.

GANOPOLSKI, A. and S. RAHMSTORF, 2001: Rapid changes of glacial climate simulated in a coupled climate model, *Nature*, **409**, 153–158.

GARZOLI, S. and A. GORDON, 1996: Origins and variability of the Benguela Current, *J. Geophys. Res.*, **101** (C1), 897–906.

GENT, P., W. LARGE and F. BRYAN, 2001: What sets the mean transport through Drake Passage?, *J. Geophys. Res.*, **106** (C2), 2693–2712.

GENT, P. and J. MCWILLIAMS, 1990: Isopycnal mixing in ocean circulation models, *J. Phys. Oceanogr.*, **20**, 150–155.

GENT, P., J. WILLEBRAND, T. MCDOUGALL and J. MCWILLIAMS, 1995: Parameterizing eddy-induced tracer transports in ocean circulation models, *J. Phys. Oceanogr.*, **25**, 463–474.

GERDES, R., C. KÖBERLE and J. WILLEBRAND, 1991: The influence of numerical advection schemes on the results of ocean general circulation models, *Clim. Dyn.*, **5**, 211–226.

GHIL, M., A. MULLHAUPT and P. PESTIAUX, 1987: Deep water formation and Quaternary glaciations, *Clim. Dyn.*, **2**, 1–10.

GLANTZ, M., 1991: Introduction, in *Teleconnections Linking Worldwide Climate Anomalies*, M. Glantz, R. Katz and N. Nicholls, eds., chap. 1, pp. 1–12, Cambridge University Press.

GLOERSEN, P., D. CAMPBELL, D. CAVALIERI, J. COMISO, C. PARKINSON and H. ZWALLY, 1992: Arctic and Antarctic sea ice, 1978-1987: Satellite passive-microwave observations and analysis, National Aeronautics and Space Administration, NASA SP-511, Washington, 290pp.

GNANADESIKAN, A., 1999: A simple predictive model for the structure of the oceanic pycnocline, *Science*, **283**, 2077–2079.

GNANADESIKAN, A. and R. HALLBERG, 2000: On the relationship of the Circumpolar Current to Southern Ocean winds in coarse-resolution ocean models, *J. Phys. Oceanogr.*, **30**, 2013–2034.

GOODMAN, P., 1998: The role of North Atlantic Deep Water formation in an OGCM's ventilation and thermohaline circulation, *J. Phys. Oceanogr.*, **28**, 1759–1785.

GOOSSE, H., J. CAMPIN, T. FICHEFET and E. DELEERSNIJDER, 1997: Impact of sea-ice formation on the properties of Antarctic Bottom Water, *Annals of Glaciology*, **25**, 276–281.

GORDON, A., 1996: Comment on the South Atlantic's role in the global circulation, in *The South Atlantic: Present and Past Circulation*, G. Wefer, W. Berger, G. Siedler and D. Webb, eds., pp. 121–124, Springer-Verlag, Berlin, Heidelberg.

GRIFFIES, S., R. PACANOWSKI and R. HALLBERG, 2000: Spurious diapycnal mixing associated with advection in a z-coordinate ocean model, *Mon. Wea. Rev.*, **128**, 538–564.

HALL, M., M. MCCARTNEY and J. WHITEHEAD, 1997: Antarctic Bottom Water flux in the equatorial western Atlantic, *J. Phys. Oceanogr.*, **27**, 1903–1926.

HARDER, M., 1996: Dynamics, roughness, and age of Arctic sea ice – Numerical investigations with a large-scale model, *Alfred-Wegener-Institut für Polar- und Meeresforschung, Bremerhaven, Germany, Reports on Polar Research*, **203**, 126pp.

HARDER, M., P. LEMKE and M. HILMER, 1998: Simulation of sea ice transport through Fram Strait: Natural variability and sensitivity to forcing, *J. Geophys. Res.*, **103** (C3), 5595–5606.

HASUMI, H. and N. SUGINOHARA, 1999: Atlantic deep circulation controlled by heating in the Southern Ocean, *Geophys. Res. Lett.*, **26**, 1873–1876.

HESSELBO, S., D. GRÖCKE, H. JENKYNS, C. BJERRUM, P. FARRIMOND, H. MORGANS BELL and O. GREEN, 2000: Massive dissociation of gas hydrate during a Jurassic oceanic anoxic event, *Nature*, **406**, 392–395.

HIBLER III, W., 1979: A dynamic thermodynamic sea ice model, *J. Phys. Oceanogr.*, **9**, 815–846.

HIBLER III, W. and K. BRYAN, 1987: A diagnostic ice-ocean model, *J. Phys. Oceanogr.*, **17**, 987–1015.

HILMER, M. and P. LEMKE, 2000: On the decrease of Arctic sea ice volume, *Geophys. Res. Lett.*, **27**, 3751–3754.

HIRST, A. and W. CAI, 1994: Sensitivity of a World Ocean GCM to changes in subsurface mixing parameterization, *J. Phys. Oceanogr.*, **24**, 1256–1279.

HOLTON, J., 1992: *An Introduction to Dynamic Meteorology*, Academic Press, San Diego, 507 pp.

HOTELLING, H., 1936: Relations between two sets of variants, *Biometrika*, **28**, 321–377.

HSIEH, W., M. DAVEY and R. WAJSOWICZ, 1983: The free Kelvin wave in finite-difference numerical models, *J. Phys. Oceanogr.*, **13**, 1383–1397.

HUGHES, T., 1995: *Uniqueness and Variability of the Ocean's Thermohaline Circulation*, C^2GCR Report No. 95-3, Department of Atmospheric and Oceanic Sciences and Centre for Climate and Global Change Research, McGill University, Montreal.

HURRELL, J., 1995: Decadal trends in the North Atlantic Oscillation: Regional temperatures and precipitation, *Science*, **269**, 676–679.

IPCC (INTERGOVERNMENTAL PANEL ON CLIMATE CHANGE), 1990: *Climate Change: The IPCC Scientific Assessment*, Houghton, J.T., Jenkins, G.J. and Ephraums, J.J., eds., Cambridge University Press.

JEFFRIES, M., ed., 1998: *Antarctic sea ice: physical processes, interactions and variability*, vol. 74 of *Antarctic Research Series*, American Geophysical Union, Washington, D.C., 407pp.

JOHNSON, G. and H. BRYDEN, 1989: On the size of the Antarctic Circumpolar Current, *Deep-Sea Research*, **36**, 39–53.

JUNG, T., 2000: *The North Atlantic Oscillation: Variability and Interactions with the North Atlantic Ocean and Arctic Sea Ice*, Ph.D. thesis, Christian-Albrechts-Universität, Kiel.

KARCHER, M. and A. LIPPERT, 1994: Spin-up and breakdown of source-driven deep North Atlantic flow over realistic bottom topography, *J. Geophys. Res.*, **99** (C6), 12,357–12,373.

KAUKER, F., 1998: *Regionalization of Climate Model Results for the North Sea*, Ph.D. thesis, Universität Hamburg.

KAWASE, M., 1987: Establishment of deep ocean circulation driven by deep-water production, *J. Phys. Oceanogr.*, **17**, 2294–2317.

KELLOGG, T., 1987: Glacial-interglacial changes in global deepwater circulation, *Paleoceanography*, **2**, 259–271.

KREYSCHER, M., 1998: Dynamics of Arctic sea ice – Validation of different rheology schemes for the use in climate models, *Alfred-Wegener-Institut für Polar- und Meeresforschung, Bremerhaven, Germany, Reports on Polar Research*, **291**, 116pp.

LAVENDER, K., R. DAVIS and W. OWENS, 2000: Mid-depth recirculation observed in the interior Labrador and Irminger seas by direct velocity measurements, *Nature*, **407**, 66–68.

LAZIER, J., 1980: Oceanographic conditions at ocean weather ship Bravo, 1964-1974, *Atmosphere-Ocean*, **18**, 227–238.

LEDWELL, J., E. T. MONTGOMERY, K. L. POLZIN, L. C. ST. LAURENT, R. W. SCHMITT and J. M. TOOLE, 2000: Evidence for enhanced mixing over rough topography in the abyssal ocean, *Nature*, **403**, 179–182.

LENDERINK, G. and R. HAARSMA, 1994: Variability and multiple equilibria of the thermohaline circulation associated with deep-water formation, *J. Phys. Oceanogr.*, **24**, 1480–1493.

LEVITUS, S., 1982: Climatological atlas of the world ocean, NOAA Prof. Pap. 13, U.S. Government Printing Office, Washington, D.C., 173 pp.

LEVITUS, S., J. ANTONOV, T. BOYER and C. STEPHENS, 2000: Warming of the world ocean, *Science*, **287**, 2225–2229.

LOHMANN, G., 1996: Stability of the Thermohaline Circulation in analytical and numerical models, *Alfred-Wegener-Institut für Polar- und Meeresforschung, Bremerhaven, Germany, Reports on Polar Research*, **200**, 128pp.

LOHMANN, G. and R. GERDES, 1998: Sea ice effects on the sensitivity of the thermohaline circulation, *J. Climate*, **11**, 2789–2803.

LOHMANN, G., R. GERDES and D. CHEN, 1996: Stability of the thermohaline circulation in a simple coupled model, *Tellus*, **48A**, 465–476.

LORENZ, E., 1956: Empirical Orthogonal Functions and statistical weather prediction, *Scientific Rep. No 1, Statistical Forecasting Project, Dept. Met., M.I.T.*

LYNCH-STIEGLITZ, J., W. CURRY and N. SLOWEY, 1999: Weaker Gulf stream in the Florida Straits during the Last Glacial Maximum, *Nature*, **402**, 644–648.

MAIER-REIMER, E., U. MIKOLAJEWICZ and K. HASSELMANN, 1993: Mean circulation of the Hamburg LSG OGCM and its sensitivity to the thermohaline surface forcing, *J. Phys. Oceanogr.*, **23**, 731–754.

MANABE, S. and A. BROCCOLI, 1985: A comparison of climate model sensitivity with data from the Last Glacial Maximum, *J. Atmos. Sci.*, **42**, 2643–2651.

MANABE, S. and R. STOUFFER, 1993: Century-scale effects of increased atmospheric CO_2 on the ocean-atmosphere system, *Nature*, **364**, 215–218.

MANN, M. and J. PARK, 1999: Oscillatory spatiotemporal signal detection in climate studies: a multiple-taper spectral domain approach, *Advances in Geophysics*, **41**, 1–131.

MANTYLA, A. and J. REID, 1983: Abyssal characteristics of the world ocean waters, *Deep-Sea Research*, **30**, 805–833.

MARSHALL, J. and Y. KUSHNIR, 1997: A 'white paper' on Atlantic Climate Variability, http://geoid.mit.edu/accp/avehtml.html.

MARSHALL, J. and F. SCHOTT, 1999: Open ocean deep convection: Observations, models and theory, *Rev. of Geophysics*, **37**, 1–64.

MARTINSON, D., 1990: Evolution of the Southern Ocean winter mixed layer and sea ice: Open ocean deepwater formation and ventilation, *J. Geophys. Res.*, **95** (C7), 11,641–11,654.

MAURITZEN, C., 1996a: Production of dense overflow waters feeding the North Atlantic across the Greenland-Scotland Ridge. Part 1: Evidence for a revised circulation scheme, *Deep-Sea Research I*, **43**, 769–806.

MAURITZEN, C., 1996b: Production of dense overflow waters feeding the North Atlantic across the Greenland-Scotland Ridge. Part 2: An inverse model, *Deep-Sea Research I*, **43**, 807–835.

MCDERMOTT, D., 1996: The regulation of northern overturning by southern hemisphere winds, *J. Phys. Oceanogr.*, **26**, 1234–1255.

MEEHL, G., W. WASHINGTON and A. SEMTNER, 1982: Experiments with a global ocean model driven by observed atmospheric forcing, *J. Phys. Oceanogr.*, **12**, 301–312.

MEINCKE, J., B. RUDELS and H. FRIEDRICH, 1997: The Arctic Ocean-Nordic Seas thermohaline system, *ICES Journal of Marine Science*, **54**, 283–299.

MEISSNER, K., 1999: *Langfristige Variabilität der thermohalinen Zirkulation in einem gekoppelten Ozean-, Meereis-, Atmosphärenmodell*, Ph.D. thesis, Universität Bremen.

MESINGER, F. and A. ARAKAWA, 1976: Numerical methods used in atmospheric models, Tech. rep., GARP Publication Series, No. 17, Vol.I.

MIKOLAJEWICZ, U. and E. MAIER-REIMER, 1990: Internal secular variability in an ocean general circulation model, *Clim. Dyn.*, **4**, 145–156.

MORON, V., R. VAUTARD and M. GHIL, 1998: Trends, interdecadal and interannual oscillations in global sea-surface temperatures, *Clim. Dyn.*, **14**, 545–569.

MÜLLER, P. and J. WILLEBRAND, 1989: Equations for oceanic motions, in *Numerical Data and Functional Relationships in Science and Technology*, J. Sündermann, ed., vol. V/3b of *Landolt-Börnstein, New Series*, pp. 1–14, Springer.

MUNK, W. and C. WUNSCH, 1998: Abyssal recipes II: Energetics of tidal and wind mixing, *Deep-Sea Research I*, **45**, 1977–2010.

NAKAMURA, M., P. STONE and J. MAROTZKE, 1994: Destabilization of the thermohaline circulation by atmospheric eddy transports, *J. Climate*, **7**, 1870–1882.

NSIDC (NATIONAL SNOW AND ICE DATA CENTER), 1996: DMSP SSM/I Brightness Temperature and Sea Ice Concentration Grids for the Polar Regions on CD-ROM, User's Guide, NSIDC Special Report 1, Cooperative Institute for Research in Environmental Sciences, University of Colorado, Boulder, USA.

ORSI, A., G. JOHNSON and J. BULLISTER, 1999: Circulation, mixing and production of Antarctic Bottom Water, *Progress in Oceanography*, **43**, 55–109.

PACANOWSKI, R., 1995: *MOM 2 Dokumentation, User's Guide and Reference Manual*, GFDL Ocean Technical Report No.3, 232 pp.

PARKINSON, C., D. CAVALIERI, P. GLOERSEN, H. ZWALLY and J. COMISO, 1999: Arctic sea ice extents, areas, and trends, 1978-1996, *J. Geophys. Res.*, **104** (C9), 20,837–20,856.

PARKINSON, C. and W. WASHINGTON, 1979: A large-scale numerical model of sea ice, *J. Geophys. Res.*, **84** (C1), 311–337.

PEDLOSKY, J., 1987: *Geophysical Fluid Dynamics*, Springer, 2nd edn., 710 pp.

PHILANDER, S., 1990: *El Niño, La Niña, and the Southern Oscillation*, Academic Press, 293 pp.

PRANGE, M., 2001: *Einfluss arktischer Süsswasserquellen auf die Zirkulation im Nordmeer und im Nordatlantik in einem prognostischen Ozean-Meereis-Modell*, Ph.D. thesis, Universität Bremen, in preparation.

RAHMSTORF, S., 1996: On the freshwater forcing and transport of the Atlantic thermohaline circulation, *Clim. Dyn.*, **12**, 799–811.

RAHMSTORF, S., 1997: Risk of sea-change in the Atlantic, *Nature*, **388**, 825–826.

RAHMSTORF, S., 1999: Decadal variability of the thermohaline ocean circulation, in *Beyond El Niño: Decadal and Interdecadal Climate Variability*, A. Navarra, ed., chap. 15, pp. 309–331, Springer-Verlag, Berlin/Heidelberg.

RAHMSTORF, S. and M. ENGLAND, 1997: Influence of southern hemisphere winds on North Atlantic deep water flow, *J. Phys. Oceanogr.*, **27**, 2040–2054.

RAHMSTORF, S. and J. WILLEBRAND, 1995: The role of temperature feedback in stabilizing the thermohaline circulation, *J. Phys. Oceanogr.*, **25**, 787–805.

REDI, M., 1982: Oceanic isopycnal mixing by coordinate rotation, *J. Phys. Oceanogr.*, **12**, 1154–1158.

REDLER, R. and C. BÖNING, 1997: Effect of the overflows on the circulation in the subpolar North Atlantic: A regional model study, *J. Geophys. Res.*, **102** (C8), 18,529–18,552.

RHEIN, M., 2000: Drifters reveal deep circulation, *Nature*, **407**, 30–31.

RINTOUL, S., 1991: South Atlantic interbasin exchange, *J. Geophys. Res.*, **96** (C2), 2675–2692.

RINTOUL, S., 1998: On the origin and influence of Adelie Land Bottom Water, in *Ocean, Ice and Atmosphere: Interactions at Antarctic Continental Margin*, S. Jacobs and R. Weiss, eds., vol. 75 of *Antarctic Research Series*, pp. 151–171, American Geophysical Union.

RINTOUL, S., C. HUGHES and D. OLBERS, 2001: The Antarctic Circumpolar Current system, in *Ocean Circulation and Climate*, G. Siedler, J. Church and J. Gould, eds., chap. 4.6, pp. 271–302, Academic Press.

ROACH, A., K. AAGAARD, C. PEASE, S. SALO, T. WEINGARTNER, V. PAVLOV and M. KULAKOV, 1995: Direct measurements of transport and water properties through the Bering Strait, *J. Geophys. Res.*, **100** (C9), 18,443–18,457.

ROSS, W., ed., 1963: *The Works of Aristotle*, vol. III, Oxford University Press, reprinted lithographically from the 1st edition, 1931.

ROTHROCK, D., Y. YU and G. MAYKUT, 1999: Thinning of the Arctic sea-ice cover, *Geophys. Res. Lett.*, **26**, 3469–3472.

RUDELS, B., 1998: Aspects of Arctic oceanography, in *Physics of Ice-Covered Seas*, Lecture notes from a summer school in Savonlinna Finland, M. Leppäranta, ed., vol. 2, pp. 517–568, Helsinki University Press.

RUDELS, B., H. FRIEDRICH and D. QUADFASEL, 1999: The Arctic circumpolar boundary current, *Deep-Sea Research II*, **46**, 1023–1062.

SARMIENTO, J. and C. LE QUÉRÉ, 1996: Oceanic carbon dioxide uptake in a model of century-scale global warming, *Science*, **274**, 1346–1350.

SAUNDERS, P. and S. THOMPSON, 1993: Transport, heat and freshwater fluxes within a diagnostic numerical model (FRAM), *J. Phys. Oceanogr.*, **23**, 452–464.

SCHILLER, A., U. MIKOLAJEWICZ and R. VOSS, 1997: The stability of the North Atlantic thermohaline circulation in a coupled ocean-atmosphere general circulation model, *Clim. Dyn.*, **13**, 325–347.

SCHMITTNER, A. and T. STOCKER, 1999: The stability of the thermohaline circulation in global warming experiments, *J. Climate*, **12**, 1117–1133.

SCHMITTNER, A. and A. WEAVER, 2001: Dependence of multiple climate states on ocean mixing parameters, *Geophys. Res. Lett.*, **28**, 1027–1030.

SCHMITZ, W., 1995: On the interbasin-scale thermohaline circulation, *Rev. of Geophysics*, **33**, 151–173.

SCHMITZ, W., 1996: On the world ocean circulation: Volume I. Some global features / North Atlantic circulation, Tech. Rep. WHOI-96-03, Woods Hole Oceanographic Institution.

SCHMITZ, W. and M. MCCARTNEY, 1993: On the North Atlantic circulation, *Rev. of Geophysics*, **31**, 29–49.

SCHÖNWIESE, C.-D., 1992: *Praktische Statistik für Meteorologen und Geowissenschaftler*, Gebrüder Borntraeger, Berlin, Stuttgart, 2nd edn., 231 pp.

SEIDOV, D. and B. HAUPT, 1997: Global ocean thermohaline conveyor at present and in the late Quaternary, *Geophys. Res. Lett.*, **24** (22), 2817–2820.

SEMTNER, J., A.J., 1976: A model for the thermodynamic growth of sea ice in numerical investigations of climate, *J. Phys. Oceanogr.*, **6**, 379–389.

STOCKER, T., 1998: The seesaw effect, *Science*, **282**, 61–62.

STOCKER, T. and O. MARCHAL, 2000: Abrupt climate change in the computer: Is it real?, *Proceedings of the National Academy of Sciences*, **97**, 1362–1365.

STOCKER, T. and L. MYSAK, 1992: Climatic fluctuations on the century time scale: a review of high-resolution proxy data and possible mechanisms, *Climate Change*, **20**, 227–250.

STOCKER, T. and A. SCHMITTNER, 1997: Influence of CO_2 emission rates on the stability of the thermohaline circulation, *Nature*, **388**, 862–865.

STOMMEL, H., 1957: A survey of ocean current theory, *Deep-Sea Research*, **4**, 149–184.

STOMMEL, H., 1961: Thermohaline convection with two stable regimes of flow, *Tellus*, **13**, 224–230.

STOMMEL, H. and A. B. ARONS, 1960: On the abyssal circulation of the worlds ocean - II. An idealized model of circulation pattern and amplitude in oceanic basins, *Deep-Sea Research*, **6**, 140–154.

STÖSSEL, A. and S.-J. KIM, 1998: An interannual Antarctic sea-ice-ocean mode, *Geophys. Res. Lett.*, **25**, 1007–1010.

STÖSSEL, A. and S.-J. KIM, 2001: Decadal deep-water variability in the subtropical Atlantic and convection in the Weddell Sea, *J. Geophys. Res.*, submitted.

STÖSSEL, A., S.-J. KIM and S. DRIJFHOUT, 1998: The impact of Southern Ocean sea ice in a global ocean model, *J. Phys. Oceanogr.*, **28**, 1999–2018.

STRASS, V. and E. FAHRBACH, 1998: Temporal and regional variation of sea ice draft and coverage in the Weddell Sea obtained from upward looking sonars, in *Antarctic sea ice: physical processes, interactions and variability*, M. Jeffries, ed., vol. 74 of *Antarctic Research Series*, pp. 123–139, American Geophysical Union, Washington, D.C.

SY, A., M. RHEIN, J. LAZIER, K. KOLTERMANN, J. MEINCKE, A. PUTZKA and M. BERSCH, 1997: Surprisingly rapid spreading of newly formed intermediate waters across the North Atlantic Ocean, *Nature*, **386**, 675–679.

THOMSON, J., 1948: *History of Ancient Geography*, Cambridge University Press, 427 pp.

TOGGWEILER, J., K. DIXON and K. BRYAN, 1989: Simulations of radiocarbon in a coarse-resolution world ocean model. 1. Steady state prebomb distributions, *J. Geophys. Res.*, **94** (C6), 8217–8242.

TOGGWEILER, J. and B. SAMUELS, 1993a: Is the magnitude of the deep outflow from the Atlantic Ocean actually governed by southern hemisphere winds?, in *The Global Carbon Cycle*, M. Heimann, ed., vol. 15 of *NATO ASI Series I*, pp. 303–331, Springer, Berlin, Heidelberg.

TOGGWEILER, J. and B. SAMUELS, 1993b: New radiocarbon constraints on the upwelling of abyssal water to the ocean's surface, in *The Global Carbon Cycle*, M. Heimann, ed., vol. 15 of *NATO ASI Series I*, pp. 333–366, Springer, Berlin, Heidelberg.

TOGGWEILER, J. and B. SAMUELS, 1995: Effect of Drake Passage on the global thermohaline circulation, *Deep-Sea Research I*, **42**, 477–500.

TOGGWEILER, J. and B. SAMUELS, 1998: On the ocean's large-scale circulation near the limit of no vertical mixing, *J. Phys. Oceanogr.*, **28**, 1832–1852.

TOMCZAK, M. and J. GODFREY, 1994: *Regional Oceanography: An Introduction*, Pergamon Press, U.K., 422 pp.

TRENBERTH, K., 1992: *Climate System Modelling*, Cambridge University Press, 788 pp.

TSUJINO, H. and N. SUGINOHARA, 1999: Thermohaline circulation enhanced by wind forcing, *J. Phys. Oceanogr.*, **29**, 1506–1516.

VIDAL, L., R. SCHNEIDER, O. MARCHAL, T. BICKERT, T. STOCKER and G. WEFER, 1999: Link between the North and South Atlantic during the Heinrich events of the last glacial period, *Clim. Dyn.*, **15**, 909–919.

VINNIKOV, K., A. ROBOCK, R. STOUFFER, J. WALSH, C. PARKINSON, D. CAVALIERI, J. MITCHELL, D. GARRETT and V. ZAKHAROV, 1999: Global warming and northern hemisphere sea ice extent, *Science*, **286**, 1934–1937.

VON STORCH, H., S. GÜSS and M. HEIMANN, 1999: *Das Klimasystem und seine Modellierung*, Springer, Berlin, Heidelberg, New York, 255 pp.

VON STORCH, H., U. WEESE and J. XU, 1990: Simultaneous analysis of space-time variability: Principal Oscillation Patterns and Principal Interaction Patterns with applications to the Southern Oscillation, *Z. Meteorol.*, **40**, 99–104.

VON STORCH, H. and F. ZWIERS, 1998: *Statistical Analysis in Climate Research*, Cambridge University Press, 528 pp.

WEAVER, A., J. MAROTZKE, P. CUMMINS and E. SARACHIK, 1993: Stability and variability of the thermohaline circulation, *J. Phys. Oceanogr.*, **23**, 39–60.

WEAVER, A. and E. SARACHIK, 1991: Evidence for decadal variability in an ocean general circulation model: An advective mechanism, *Atmosphere-Ocean*, **29**, 197–231.

WELANDER, P., 1986: Thermohaline effects in the ocean circulation and related simple models, in *Large-Scale Transport Processes in Oceans and Atmosphere*, J. Willebrand and D. Anderson, eds., vol. 190 of *NATO ASI Series C*, pp. 163–200, D. Reidel Publishing Company, Dordrecht.

WEYL, P., 1968: The role of the ocean in climatic change: a theory of the ice ages, *Meteorological Monographs*, **8**, 37–62.

WHITE, W. and R. PETERSON, 1996: An Antarctic Circumpolar Wave in surface pressure, wind, temperature and sea ice extent, *Nature*, **380**, 699–702.

WHITWORTH, III, T., 1983: Monitoring the net transport of the Antarctic Circumpolar Current at Drake Passage, *J. Phys. Oceanogr.*, **13**, 2045–2057.

WHITWORTH, III, T. and R. PETERSEN, 1985: The volume transport of the Antarctic Circumpolar Current from three-year bottom pressure measurements, *J. Phys. Oceanogr.*, **15**, 810–816.

WILLEBRAND, J., 1993: Forcing the ocean by heat and freshwater fluxes, in *Energy and Water Cycles in the Climate System*, E. Raschke and D. Jacob, eds., vol. 5 of *NATO ASI Series I*, chap. 9, pp. 215–233, Springer-Verlag, Berlin.

WINTON, M., 1997: The effect of cold climate upon North Atlantic Deep Water formation in a simple ocean-atmosphere model, *J. Climate*, **10**, 37 – 51.

WORBY, A. and S. ACKLEY, 2000: Antarctic research yields circumpolar sea ice thickness data, *EOS, Transactions, Am. Geophys. Union*, **81** (17), 181–185.

WÜST, G., 1935: Schichtung und Zirkulation des Atlantischen Ozeans. Das Bodenwasser und die Stratosphäre., *Wiss. Ergebn. Dt. Atlant. Exped. „Meteor" 1925-27, Berlin*, **6**, 1–288.

YANG, J., 1999: A linkage between decadal climate variations in the Labrador Sea and the tropical Atlantic Ocean, *Geophys. Res. Lett.*, **26**, 1023–1026.

YU, E.-F., R. FRANCOIS and M. BACON, 1996: Similar rates of modern and last-glacial ocean thermohaline circulation inferred from radiochemical data, *Nature*, **379**, 689–694.

ZALESAK, S. T., 1979: Fully multidimensional flux-corrected transport algorithms for fluids, *J. Comput. Phys.*, **31**, 335–362.

Acknowledgments

The Alfred Wegener Institute for Polar and Marine Research (AWI) provided the organizational framework for the preparation of this PhD thesis. It came into being under the supervision of Prof. Dirk Olbers and Dr. Rüdiger Gerdes. Working circumstances were optimal with regard to both computational and logistic environment as well as to "the human factor".

A number of people have contributed to the development of this work – directly or indirectly. I would like to give special thanks to:

- Prof. Dirk Olbers for his willingness to supervise and support my work and many helpful suggestions improving the manuscript.
- Prof. Monika Rhein for examining my work.
- Dr. Rüdiger Gerdes. Without him this thesis wasn't what it is. I found him always a sympathetic listener giving valuable advise and helping me to find my way through the jungle of modeling. Yet he never restricted the freedom of learning by experience and let me keep and develop my own style. The mixture of professional support and profound humor made him the mainstay of this work.
- all the members of AWIs "MAD" working group for lots of discussions, ideas, fun and time spent together.
- Dr. Katrin Meißner and Jennifer Brauch for the best company in the ups and downs of Bremerhaven. Furthermore the first one put the results of her model runs to my disposal, the latter one was a big help on every computing problem and did a great job improving the graphs in this study.
- Dr. Frank Kauker was always at hand with advise on statistical analyses and often had the clue.
- Dr. Michael Karcher had all those tiny oceanographic ideas and solutions.
- Cornelia Köberle showed me how to decipher MOM's model code and had the answers.
- Matthias Prange for help solving all those little everyday problems and plenty of meaningful and senseless discussion in the office we shared.
- Rüdiger, Martin, Katrin, Frank, Matze, Jenny and Daniel for reading over parts of my manuscript and lots of suggestions.
- Dr. Hans-Martin Hagen for philosophical assistance.
- Katja, Martin, Heike, Hannah and Nora. For making things colorful, that looked grey before.
- A. of R. for turbulence – what would a geoscientist be without it!